From macro to nano : a multi-scale electrochemical investigation of oxygen reduction reaction on a Pt-free catalyst

Ndrina Limani

To cite this version:

Ndrina Limani. From macro to nano : a multi-scale electrochemical investigation of oxygen reduction reaction on a Pt-free catalyst. Catalysis. Université Paris-Saclay, 2022. English. NNT : 2022UPASF088 . tel-04563660

HAL Id: tel-04563660
https://theses.hal.science/tel-04563660
Submitted on 30 Apr 2024

From macro to nano: a multi-scale electrochemical investigation of oxygen reduction reaction on a Pt-free catalyst

Analyses électrochimiques multi-échelles, du macro au nano, de la réduction de l'oxygène par un catalyseur sans métaux nobles

Thèse de doctorat de l'université Paris-Saclay

Thèse préparée dans l'unité de recherche **NIMBE** (Université Paris-Saclay, CEA, CNRS),
sous la direction de **Renaud CORNUT**, Directeur de recherche,
et la co-direction de **Bruno JOUSSELME**, Directeur de recherche

École doctorale n°571: Sciences chimiques: molécules, matériaux, instrumentation et biosystèmes (2MIB)
Spécialité de doctorat: Chimie
Graduate School: Chimie. Référent: Faculté des sciences d'Orsay

Thèse soutenue à Paris-Saclay, le 12 Décembre 2022, par

Ndrina LIMANI

Composition du Jury

Membres du jury avec voix délibérative

Sylvain FRANGER Professeur (HDR), ICMMO, Université Paris-Saclay	Président
Carlos M. SÁNCHEZ-SÁNCHEZ Chargé de Recherche (HDR), LISE, Sorbonne Université	Rapporteur & Examinateur
Laetitia DUBAU Directrice de Recherche (HDR), LEPMI, Grenoble	Rapportrice & Examinatrice
Jean-Marc NOËL Chargé de Recherche, ITODYS, Université de Paris	Examinateur

THÈSE DE DOCTORAT

NNT : 2022UPASF088

université PARIS-SACLAY

ÉCOLE DOCTORALE
Sciences Chimiques: Molécules,
Matériaux, Instrumentation
et Biosystèmes (2MIB)

Titre : Analyses électrochimiques multi-échelles, du macro au nano, de la réduction de l’oxygène par un catalyseur sans métaux nobles.

Mots clés : réaction de réduction de l'oxygène, matériau sans Pt, électrocatalyse, RRDE, SECM, SECCM.

Résumé : L'évaluation de l'activité catalytique pour la réduction de l’oxygène est cruciale pour prédire et améliorer les performances d des piles à combustible. Ceci est particulièrement important pour l'évaluation de la sélectivité de la réaction (nombre d'électrons), étant donné que la production de H_2O_2 dans les piles à combustible à membrane échangeuse de protons entraine une dégradation rapide de leurs performances. Ce travail de thèse s’appuie sur plusieurs techniques de caractérisation électrochimique pour étudier un catalyseur sans métaux noble Fe-N-MWCNT. Une première étude par la méthode classique disque-anneaua permis de mettre en évidence l'influence du chargement des électrodes sur l’allure des voltammogrammes et sur le nombre d'électrons transférés. Un cadre théorique original considérant la résistance des agglomérats est développé pour interpréter les résultats et comprendre l’impact des conditions de préparation des encres sur les performances mesurées. Ensuite, la microscopie électrochimique est utilisée pour étudier des chargements en catalyseur plus faibles. Une nouvelle méthodologie utilisant successivement 2 microélectrodes (une en Au pour la détection de la réduction du O_2 et une en Pt pour l’oxydation du H_2O_2) a été développée. Cette approche apporte des informations intéressantes sur la capacité du catalyseur à produire du peroxyde, mais l’impact du chargement est toujours significatif. Finalement, l’activité catalytique d’agglomérats individualisés a été investie via la technique électrochimique SECCM et l’utilisation de nanopipettes. La même activité est obtenue pour différents agglomérats ayant différentes teneurs en Nafion. Le couplage de l'étude électrochimique à des analyses MEB a ainsi permis de corréler la morphologie des agglomérats à leur activité catalytique.

ÉCOLE DOCTORALE
Sciences Chimiques: Molécules,
Matériaux, Instrumentation
et Biosystèmes (2MIB)

Title : From macro to nano : a multi-scale electrochemical investigation of oxygen reduction reaction on a Pt-free catalyst

Keywords : oxygen reduction reaction, Pt-free material, electrocatalysis, RRDE, SECM, SECCM.

Abstract : The unambiguous evaluation of ORR activity in the laboratory scale is crucial for an accurate catalyst performance prediction on fuel cells. This is especially important when it comes to ORR selectivity assessment (number of electrons), considering that an unforeseen H_2O_2 production in a FC would lead to performance losses. This thesis makes use of several electrochemical characterization techniques to investigate one non-noble Fe-N-MWCNT electrocatalyst. Starting from RRDE method which is utilized to study the material for its activity and selectivity, the results highlight the influence of electrode loading on the shape of ORR voltammograms and on the number of transferred electrons. An original theoretical framework involving agglomerate resistance is developed, and further used to understand the impact of the ink processing condition on the overall performance. Furthermore, advantage of SECM is taken as a micro-scale technique which allows the study of lower loadings than RRDE. A new SECM dual-electrode investigation approach developed in our group is used successfully in this work, namely an Au UME for ORR detection and Pt UME for H_2O_2 detection. Whilst this approach unravels interesting information about the catalyst's ability for peroxide production, the varying number of electrons with loading is still apparent. Finally, SECCM is employed to unravel the intrinsic ORR activity of individual catalyst agglomerates independent of Nafion content via nano-pipettes. Coupling with SEM made it possible to correlate the morphology of the agglomerates to their catalytic activity.

Acknowledgements

I will start by thanking the **European Commission** for giving such extraordinary opportunities for people coming from third-world countries such as myself. Getting *funded* to achieve my dream of earning a PhD and Masters at some of Europe's greatest universities, is something that cannot be underestimated. I am and will be forever truly grateful for this experience and I will do my very best to give back and contribute to the scientific community as much as I can. I thank all participants of the **SENTINEL consortium**, with whom we had great training weeks in Paris, Rimini and Nice. It was a privilege for me to be in a room and discuss with some of the greatest minds in single entity nano electrochemistry.

I want to thank wholeheartedly my supervisors **Renaud** and **Bruno**, who made sure to be there for me every single time I needed and spent time on purposeful discussions and teaching. They never spared their encouraging words which had a huge impact on my motivation, so thank you a million for shaping me into the scientist I am today. Almost in parallel with my supervisors I have to thank **Alice** who passed all her SECM knowledge to me and was a great colleague to collaborate with. Us all made a great team. I thank **Emmanuel Scorsone** for collaborating with me and preparing the BDD which I used all these years. I would like to thank every single member of the **LICSEN** lab, especially **Vincent** and **Frederic** who were extremely helpful and polite with me. It was a pleasure during these times to have lunch and coffee breaks at CEA with **Lina**, **Yuemin**, **Daniel, Sarah**, **Fabien, Thomas, JC Gabriel** and **Nathan**. CEA would not be the same without you. I thank **Robin** for introducing the CEA to me in the very beginning and always being ready to help. Concerning the non-work-related people, I am glad I had **Eneda** as one of my few friends in Paris, who made this city feel more home to me.

I am grateful to **Wolfgang** for hosting me at Ruhr University in Bochum where I had some of the most productive and pleasant months. I want to thank my friend **Stefan** who was always there for me and tirelessly introduced me to the complicated world of nanoelectrodes. Not to forget my lunch buddies, especially **Adarsh** with whom we had so many laughs every single day. Stefan and Adarsh are only some of the amazing friends I made in Bochum and that I cannot wait to see again. It was a pleasure to work also with **Emmanuel**, **Moonjoo** and **Thomas** for the SECCM work and I thank them for helping as MATLAB and SEM *professionals*.

I am so blessed to have an extraordinary family: **Besa**, **Dukagjin**, **Bleron**, **Granit**, **Gresa** and my little ones **Dielli** and **Mar**, whose existence and unconditional love is what keeps me mentally well and ready for anything. Talking about family, a new member which I was very lucky to meet during these studies is my fiancé **Pedro**, who is now by my side every single day, is my right hand and my biggest supporter. When I count my blessings, I count him many times.

Finally, I dedicate this achievement to my wonderful parents.

Contents

Notations

AFM	Atomic Force Microscopy
Bm ink	Ball Milling ink
CA	Chronoamperometry/chronoamperogram
C_{dl}	Double Layer Capacitance
CE	Counter Electrode
CL	Catalyst Layer
C_s	Specific Capacitance
CV	Cyclic Voltammetry/Cyclic voltammogram
ECSA	Electrochemical Surface Area
FC	Fuel Cell
FCV	Fuel Cell Vehicle
GCE	Glassy Carbon Electrode
GDL	Gas Diffusion Layer
LSV	Linear Sweep Voltammetry/Linear Sweep Voltammogram
MEA	Membrane Electrode Assembly
N	Collection Efficiency
n	Number of Transferred Electrons
O_2	Dioxygen
ORR	Oxygen Reduction Reaction
PEMFC	Proton Exchange Membrane Fuel Cell
RC	Redox Competition Mode
RCE	Reference Counter Electrode
RDE	Rotating Disc Electrode
RE	Reference Electrode
RHE	Reversible Hydrogen Electrode
RRDE	Rotating Ring Disc Electrode
SCE	Saturated Calomel Electrode

SECCM	Scanning Electrochemical Cell Microscopy
SECM	Scanning Electrochemical Microscopy
SEM	Scanning Electron Microscopy
SG/TC	Substrate Generation Tip Collection Mode
SPM	Scanning Probe Microscopy
TG/SC	Tip Generation Substrate Collection Mode
TPB	Triple Phase Boundary
UME	Ultramicroelectrode
Us ink	Ultrasonicated Ink
WE	Working Electrode

Résumé étendu en français

Les conséquences environnementales et sanitaires causées par la combustion de sources d'énergie non durables telles que les combustibles fossiles ont suscité beaucoup d'attention dans la recherche d'alternatives plus viables. Alors que de nombreux développements sont en cours dans cette direction, notamment l'énergie solaire, éolienne et hydraulique, il est toujours nécessaire de disposer d'un vecteur énergétique capable de transporter l'énergie dans le temps et dans l'espace. L'hydrogène est désormais reconnu comme le vecteur énergétique le plus prometteur pour remplacer les combustibles fossiles. Dans le secteur de l'énergie des transports par exemple, les véhicules à hydrogène (Fuel Cell Vehicles, FCV) présentent des avantages prometteurs avec 0% d'émissions par rapport aux moteurs à combustion. Cependant, la maturation d'une telle technologie ne progresse pas de manière significative en raison des complications liées à sa chimie. La réaction de réduction de l'oxygène (ORR) se produisant à la cathode des piles à combustible est une réaction lente en plusieurs étapes, se produisant par une voie possiblement directe ou indirecte *via* la production d'un intermédiaire (H_2O_2). Les électrocatalyseurs nécessaires pour stimuler cette réaction sont généralement des catalyseurs rares à base de platine. Cela a conduit depuis des décennies à rechercher des matériaux alternatifs actifs pour l'ORR, et l'étude des électrocatalyseurs non nobles (sans Platine) reste toujours l'un des sujets brûlants dans le domaine.

Dans cette thèse, un catalyseur à base de nanotubes de carbone multiparois modifiés avec N et Fe (Fe-N-MWCNT) est choisi comme matériau de référence et étudié pour son activité ORR en milieu acide. Même si l'analyse des électrocatalyseurs peut être effectuée dans un système d'assemblage d'électrodes à membrane (MEA) avec des résultats proches de ce à quoi on pourrait s'attendre dans une pile à combustible, cela prend beaucoup de temps et de matériel. Les méthodes de laboratoire, sont, elles, plus robustes et moins exigeantes, et offrent également la possibilité d'extraire des informations fondamentales cruciales sur l'électrochimie du catalyseur. Par conséquent, dans cette thèse, toutes les investigations ont été effectuées avec des techniques électrochimiques de laboratoire. L'électrode à disque rotatif (anneau) (R(R)DE) est la méthode de laboratoire la plus utilisée en électrocatalyse, fournissant des informations cruciales sur l'activité intrinsèque de l'ORR en termes de surtension et sur la sélectivité de l'ORR en termes de quantité de H_2O_2 formé. Cependant, cette méthode est très performante pour des couches minces de catalyseur, alors qu'en pratique, comme les catalyseurs non nobles sont intrinsèquement moins actifs, des couches d'électrodes assez épaisses sont généralement étudiées. Cela complique l'interprétation des mesures, car l'organisation du matériau dans la couche épaisse a une influence sur l'exposition des sites actifs. Par conséquent, la séparation du concept d'activité intrinsèque du catalyseur et d'organisation de la matière dans la couche est cruciale. C'est quelque chose qui a été abordé dans le troisième chapitre de cette thèse, où avec la RRDE nous expliquons comment les conditions de préparation des couches catalytiques influencent la performance obtenue. Il s'avère que la forme des voltammogrammes peut permettre d'obtenir des informations sur la qualité de l'organisation de la matière active dans le matériau. Par contre, la RRDE n'est pas très appropriée pour étudier la sélectivité de la réaction, étant donné que le nombre d'électrons transférés qu'on observe change très significativement avec le chargement, quel que soit le chargement.

Pour cette raison, nous avons utilisé une autre méthode pour étudier la sélectivité. La méthode, relativement peu utilisée par la communauté malgré les informations qu'elle apporte, s'appuie sur la microscopie électrochimique à balayage (SECM). C'est une technique d'électrochimie à l'échelle micrométrique, qui permet d'étudier des quantités de matériau beaucoup plus faibles qu'en RRDE, ce qui supprime les complications liées à l'épaisseur de la couche catalytique. Dans le quatrième chapitre, nous montrons comment la SECM peut être utilisée pour extraire la sélectivité ORR de manière plus fiable grâce à l'étude de chargements très faibles, et à l'utilisation de sondes micrométriques. Le même catalyseur étudié (Fe-N-MWCNT) qui, en RRDE présentait un nombre d'électrons transférés proche de 4 par molécule d'Oxygène consommé, apparait en fait -grâce à la SECM- comme ayant un nombre d'électrons proche de 2, si bien que ce catalyseur n'est en fait pas si performant. Ce résultat illustre l'intérêt de la microscopie électrochimique pour la sélection des électrocatalyseurs, compte tenu du caractère indésirable de l'intermédiaire H_2O_2 majoritairement produit, en raison de ses effets dégradants sur la matrice carbonée. Même si la SECM est très utile, sa résolution est limitée à la taille de la sonde, de taille micrométrique dans nos travaux. Zoomer sur le catalyseur avec une résolution nanométrique est par contre envisageable avec une autre technique à sonde locale, la microscopie à cellule électrochimique à balayage (SECCM). Dans le cinquième et dernier chapitre de cette thèse, nous montrons comment, par SECCM, avec des pipettes de taille nanométrique, nous pouvons acquérir l'activité ORR intrinsèque des agglomérats individuels du catalyseur Fe-N-MWCNT, en normalisant le courant avec la surface électrochimique (ECSA). Une analyse SEM ultérieure permet alors de corréler l'activité catalytique et la morphologie des agglomérats.

Introduction

The significance of setting up an eco-friendly environment, free of hazardous and heat-trapping greenhouse gases, is apparent to everyone. If for a start, we can only convert the transportation sector into an environmentally friendly one, we would significantly reduce the overall emissions worldwide. While the human factor is key to achieve that, time pressure, technical limitations and economic factors often conquer the conscience. Having a means that could beat all these factors with fast and inexpensive solutions while at the same time benefiting the environment, would doubtlessly solve the problem. One of those means could be fuel cell vehicles (FCV), for the development of which the scientific community is working endlessly for decades. Yet, their progress is currently not at the desired level due to the inherent complexities of such systems and their unaffordable price mainly related to the cathode electrocatalyst.

Large scale commercialization of FCV is the final step of many antecedent problems that are necessary to be solved primarily. Considering the oxygen reduction reaction (ORR) aspect, first of all, there is a lot of thought put into the design and synthesis of an active, selective, stable, cost-effective, and abundant ORR electrocatalytic material. These are a lot of prerequisites that rarely overlap in a unique material, putting the scientific community already in a tricky situation for finding the perfect candidate.

Thereafter, the electrocatalysts are screened for their catalytic activity in the laboratory mostly with the rotating (ring) disc electrode (R(R)DE) method and if excellent performance is found, further screening on membrane electrode assembly (MEA) is required. Regrettably, this step is often a barrier preventing the continuation to further stages. When investigating Pt-free catalysts, usually higher amounts of materials are investigated compared to Pt, in order to compensate for their lower intrinsic activity. The thick catalyst layers often tend to hide the real electrochemical response, as will be discussed later on. Indeed, in previous works it has been pointed out that the MEA and RRDE performances are considerably different, with RRDE results highly overestimating the ORR performance (Figure 1).[1] Certainly, these two investigation methods have their differences, however, the catalyst ought to have an intrinsic activity and selectivity not significantly dependent on the methodology used.

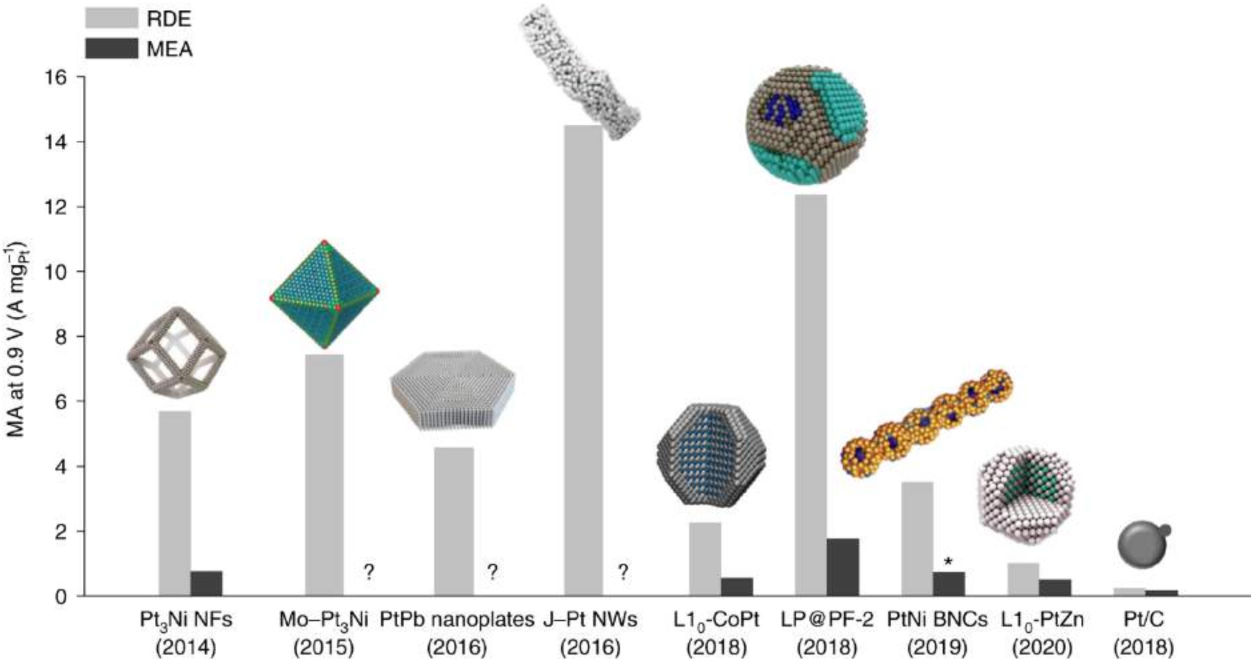

Figure 1 Difference in RRDE vs MEA performance results for Pt-based materials, and for Pt-free materials (LP@PF-2). The ‘?’ designates that the experiment was not performed in a fuel cell while the ‘*’ indicates that the fuel cell data have been obtained from polarization curves. All the data was evaluated at 0.1 M $HClO_4$ saturated with O_2. Other experimental details are explicated in the reference.[1]

Therefore, this invokes the question: are we accurately determining the ORR performance on the lab scale, or are we too focused on synthesizing novel electrocatalysts? This question is even more pertinent when one considers that there are other lab-scale methodologies besides RRDE with the ability to investigate ORR performance, although significantly underused by the community.

Consequently, this thesis deals with the investigation of an electrocatalytic Pt-free material on the lab scale, with several characterization methods to unleash their power and limitations, as well as the intrinsic ORR activity and selectivity of the catalyst.

While Chapter I gives an introduction to the energy transition and the role of ORR in this field, Chapter II presents the principles of the electrochemical methods that were used to evaluate the ORR performance such as RRDE, scanning electrochemical microscopy (SECM), and scanning electrochemical cell microscopy (SECCM).

Starting with RRDE as the macro-scale technique conventionally used, although it is already well-established, does the processing condition of the catalyst ink require more attention for an accurate activity assessment? Answers to this question are provided in Chapter III where the electrocatalytic ORR activity of the Fe-N-MWCNT catalyst is evaluated, with purposeful discussions of the expected and unanticipated results.

When the limitation of RRDE is identified, the advantage of the micro-scale SECM technique is taken as presented in Chapter IV. This method permits the study of smaller loadings which would in principle clear out the impediments coming from catalyst layer thickness, mainly the trapping of the intermediate within. Coupling with AFM, it is possible to determine the agglomerate size and distribution of the deposit, and then discuss their correlation to the catalytic activity.

Finally, zooming into individual agglomerates of the material with nano-scale high resolution can be achieved by SECCM investigations, as presented in Chapter V. Studying single entities has the advantage of unambiguously determining the ORR activity without the influence of many experimental factors that are usually impediments in macro and micro scale techniques. When coupled with SEM, it is possible to correlate the morphology of each agglomerate to its ORR activity.

The experimental work of Chapter III and Chapter IV was done under the supervision of Renaud Cornut and Bruno Jousselme at the Laboratory of Innovation in Surface Chemistry and Nanosciences (LICSEN) at CEA-Saclay. This laboratory gathers organic chemists and electrochemists to work jointly on the synthesis, investigation, and application of Pt-free materials on fuel cells. The work of Chapter V was conducted at the Center for Electrochemical Sciences (CES) at Ruhr University in Bochum, under the supervision of Professor Wolfgang Schuhmann.

Chapter I: Energetic transition and the role of oxygen reduction reaction electrocatalysts

Transposing the fossil fuel-based energetic systems with green alternatives is mandatory for a sustainable way of living. Making the transportation energy sector more environmentally friendly is one of the approaches to boost this energetic transition, with FCV demonstrating promising potential for reaching that goal. However, the challenges associated to oxygen reduction reaction (ORR) electrocatalysis are doubtlessly the most intricated impediments to solve, mainly due to the complexity of this reaction and the scarce electrocatalysts necessary. In this chapter, an overview of the current status on electric vehicles is presented, elaborating more the fuel cell technology and the challenges associated to it. Finally, an introduction of ORR and the common electrocatalytic classes of materials is presented.

1.1 Towards decarbonization of the transport energy sector

1.1.1 Repercussions of fossil fuel consumption and alternative energies

It is well known that currently the burning of fossil fuels accounts for about 80% of energy production worldwide,[2] a fact which is sabotaging the well-being in our planet in many ways. To start with, this form of energy production is the major cause of high amounts of greenhouse gases, including carbon dioxide (CO_2), methane (CH_4) and nitrous oxide (N_2O), which have a tendency to trap the heat in the atmosphere. Only CO_2 alone was predicted long ago to be about 61% of the reason of global warming in this century, mainly due to its massive production by the human factor.[3] Not to mention its hazardous impact on human health,[4] along with other air pollution particulates such as NO_x, SO_x, and CO.[5] Moreover, at the rate in which fossil fuels have been employed, it is actually estimated that they will be exhausted and out of stock no longer than a few decades from now.[6]

Therefore, the urgency of developing and commercializing technologies based on alternative energy sources is now evident.[7] Renewable energy sources that are more sustainable and their working principle does not involve emission of harmful gasses are growing in many countries, such as sun, wind and water-based energy. However, these natural resources are not spread evenly in the globe and in time, making it hard to meet the demands of the increasing population.[8] Despite their sustainability, the lack of effective energy storage of such energy sources still possess a challenge in their desired larger-scale application.[9] Most importantly, the problem of emissions coming from combustion engine vehicles which accounted for 99% of the overall engines in 2019, was not solved until now.[10] Considering that about a quarter of CO_2 emissions comes from the transport sector alone,[11] development of fossil-fuel-free vehicles would facilitate the drop in overall emissions, with battery and fuel cell electric vehicles being propitious candidates.

1.1.2 Electric Vehicles-Batteries and Fuel cells

Battery electric vehicles (BEV) are one of the technologies which store chemical energy, generating thereafter electrical current while discharging. Lithium-Ion Battery (LIB) based electric cars started launching in the beginning of 21st century including Tesla Model S, BMW i3, Toyota Prius Prime etc, becoming a multi-billion-dollar industry.[12] The sales of BEV are predicted to increase enormously by 2030, leading to a further increase in demand of battery-system materials,[13] with lithium and copper being consumed in the largest amount.[14] The latter is also utilized in the recharging infrastructure and electricity generation,[15]predicting a very demanding electrical network considering the rate at which BEV production will increase. One of the main disadvantages of BEV is that they require big reservoirs with limited capacity and driving range.[16]

An alternative solution to most of those problematics could be FCV, which are based on energy conversion devices whose principle consists on converting chemical energy directly to electrical energy by oxidizing a fuel in the anode and reducing another chemical species at the cathode (reactions shown in Figure 2).[16] Although a variety of fuels can be employed, the greatest benefit of using FCV is their ability to utilize hydrogen as a fuel. Being the most lightweight and available element on earth, hydrogen can be stored and transported in tanks with a superior safety factor compared to conventional engines.[17] Moreover, replacing the fossil fuel and gas energy vector with H_2 is generally accepted as a promising approach to diminish the global warming, considering that it leads to only water as a by-product.

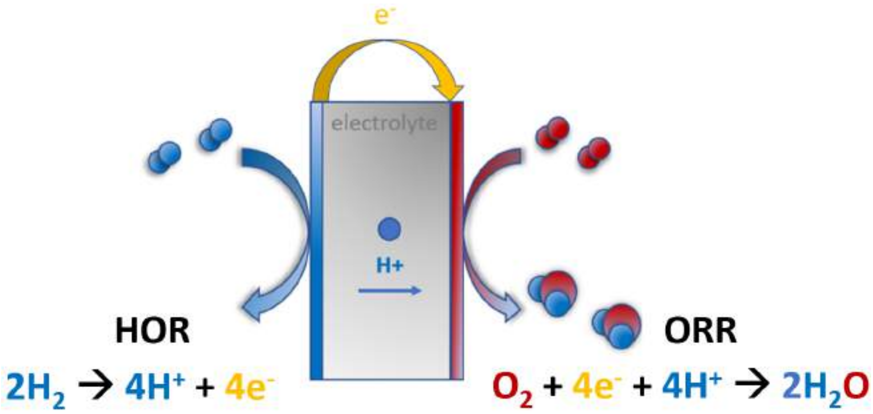

Figure 2 Electrochemical reactions occurring at both electrodes in a fuel cell.

Nowadays, FCV have reached the market thanks to decades of intensive research, with models such as Toyota Mirai, Hyundai ix35, Honda Clarity, Hyundai Nexo etc already launched, although not available in all countries due to limited necessary infrastructure and higher cost.[18] The biggest advantage of FCV is their superiority when it comes to fast recharging times and significantly extended driving ranges, thus excluding the problem of intermittency. This makes them suitable for heavy transportation sectors, as presented in Figure 3.[19] Nevertheless, the large storage tanks needed due to the exceptionally low H_2 density is a matter of concern in this field.[20] Moreover, despite the propitiousness of FCV, the most significant obstacle that prevents them from dominating the market is their price. The high-cost is mainly affiliated to the membrane electrode assembly (MEA), which will be explicated more in the next section.

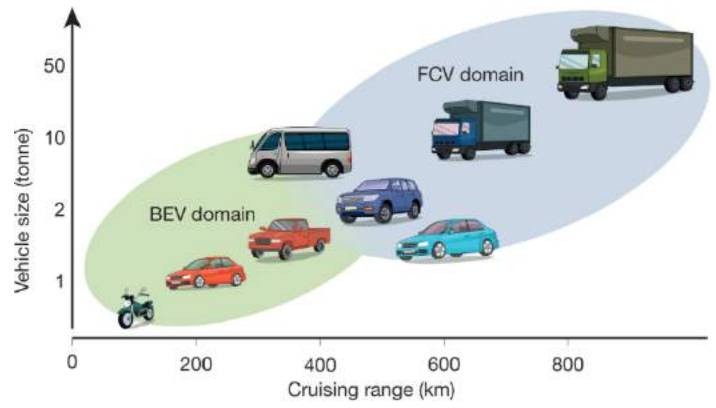

	BEV	FCV
Storage media	Li–ion batteries	Hydrogen
Energy density	<200 W h kg^{-1}	~300 W h kg^{-1}
Refuelling time	Hours	Minutes
Low temperature	Severe degradation	Demonstrated at –30 °C
Efficiency	~90%	~60%
Infrastructure	Grid and charging piles	Hydrogen stations

Figure 3 Illustration showing the comparison of FCV and BEV, the efficiency represents the BEV charging efficiency and the FCVs H_2-to-electricity conversion efficiency. It is higher for BEV considering a wider infrastructure. The energy density implies BEVs battery pack and battery management system and the FCVs fuel cell system and H_2 tank. Moreover, for similar sized vehicles, the refueling time is dozens of hours for a BEV and only 5-10 min for a FCV.[19]

1.2 PEMFC technology

1.2.1 PEMFC working principle and components

As mentioned in the previous section, hydrogen holds the spotlight for being the greenest FC fuel by forming only water as a product, making it the most mature technology up to now.[21] One of the FC types which uses H_2 is proton exchange membrane fuel cell (PEMFC) which has leading performances when it comes to the high efficiency, low emissions, fast change in the functioning intensity, longer lifetime, cheaper manufacture and the lightweight.[22,23] Most importantly, PEMFC have low operating temperature which prevents membrane dehydration,[22,23] making the research towards their development up and coming in the field.

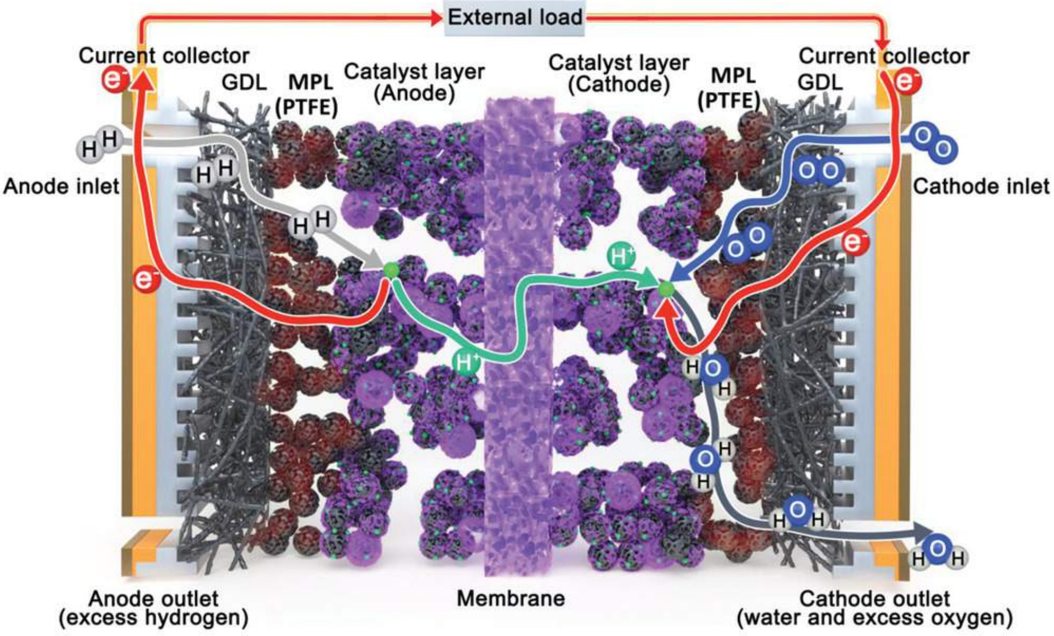

Figure 4 PEMFC scheme.[24]

In Figure 4 one can see an illustration representing the PEMFC, with the flow fields permitting the entry of gases needed for the reactions to occur, in between of which the membrane electrode assembly (MEA) is placed. The latter includes mainly a proton exchange membrane (PEM), a gas diffusion layer (GDL) along with a microporous layer (MPL), and a catalyst layer

(CL).[25] While the GDL is mainly responsible for allowing the gas molecules to diffuse in the system, the MPL made of carbon nanospheres and Polytetrafluoroethylene (PTFE) strengthens gas transport and removes H_2O formed at the cathode.[24,26] Moreover, the CL ensures the electron transfer and the PEM the proton conductivity. More precisely, when the CL at the anode is in contact with H_2, hydrogen oxidation reaction (HOR) occurs and dissociates to proton ions and electrons. While the electrons flow to the circuit to generate electricity, the proton ions diffuse through the PEM to reach the other CL at the cathode. Inhere, O_2 diffuses to the cathode where it gets adsorbed and gets its O=O bond weakened by the electrons transported from the anode, in addition to the consummation of proton ions coming from the PEM, hence oxygen reduction reaction (ORR) occurs with water as a product (reactions presented in Figure 2).[27] The performance of a fuel cell is closely linked to the MEA and the malfunction of any of its components greatly compromises the overall functionality of the fuel cell. In particular, the CL component is one of the biggest problematics regarding FC large-scale commercialization, as will be shown in the next section.

1.2.2 Catalyst layer and the challenges associated to it

The CL is comprised of catalyst particles, a carbon support to ensure good conductivity and an ionomer serving as a binder and/or proton conductor, usually Nafion. The CL is the most principal part of the PEMFC due to its complexity and many functionalities it carries. Besides the proton transport, it is also responsible for the transport of reacting species which go in and out of the system.[28] Moreover, it carries out the electron transfer in the boundary between the reactant, ionomer and catalyst where the molecular, proton and electron channels intersect (triple-phase-boundary or TPB) as illustrated in Figure 5. As a consequence, designing a catalyst layer that undertakes all these processes successfully while exhibiting high reaction rates and keeping the catalyst amount to the minimum, is doubtlessly not a trivial task.

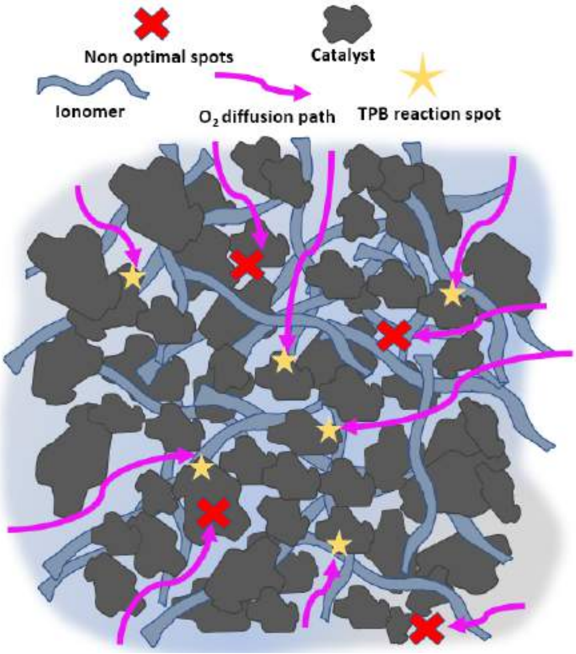

Figure 5 Illustration of the inside structure of an agglomerate and TPBs where reaction occurs.

Firstly, forming a CL with as many TPBs as possible is crucial for a high activity.[29,30] The TPB formation depends mainly on the way the catalyst is dispersed and the microporosity of the carbon support hence the Nafion penetration through it.[25] Moreover, the formulation of catalyst ink is important to be optimized, considering that too little Nafion content can compromise the proton conductivity in a FC, or lead to bad dispersion and poor catalyst adherence on the substrate in laboratory-scale investigations.[31] On the other hand, higher amounts of Nafion can compromise the electronic conductivity in the material due to its electrically insulating nature. The way the catalyst ink is processed is also a crucial factor, with small particles being the target in order to maximize surface area and available active sites.

Both electrodes in a FC require a CL, however the ORR reaction occurring in the cathode is a sluggish multi-step reaction 6 orders of magnitude slower than the anode reaction HOR,[32] making it the biggest problematic sought to be resolved. This is especially true when considering the acid media which is a harsh environment for the majority of ORR catalytic materials, as in alkaline media it is generally known that the catalyst is not as much challenged.[33] Catalyst particles or the electrocatalytic material is the most critical component of the CL. It is now a generally accepted fact that the cost of commercial ORR electrocatalysts is one of the primary obstacles hindering fuel cell commercialization,[18] pushing researchers to seek for alternative cost-effective ORR active materials. In the next sections, ORR pathways and an overview of common electrocatalytic materials is presented.

1.3 Oxygen reduction reaction (ORR)

1.3.1 Oxygen reduction reaction pathways

The pathways in which ORR occurs are mainly through a direct and efficient four-electron transfer shown in Equation 1 in acid media, or an indirect pathway with H_2O_2 formed as an intermediate (Equation 2).[34] The H_2O_2 can then get further reduced to water (Equation 3), or get decomposed (Equation 4).[35] This is the general way of describing ORR pathways, however one must bear in mind that there are other intermediates proved to be formed during ORR, including the superoxide ion formed via 1-electron reduction (O_2^-)[35,36] or the OH· radical via a 3-electron pathway.[37]

Direct pathway: $$O_2 + 4H^+ + 4e^- \rightarrow 2H_2O \qquad 1$$

Indirect pathway: $$O_2 + 2H^+ + 2e^- \rightarrow H_2O_2 \qquad 2$$

$$H_2O_2 + 2H^+ + 2e^- \rightarrow 2H_2O \qquad 3$$

$$2\mathrm{H_2O_2} \rightarrow 2\mathrm{H_2O} + O_2 \qquad 4$$

Nevertheless, the formation of peroxide leads to the degradation of carbon-based catalysts,[38] it can attack the Nafion membrane in the FC[39] and generally this pathway is less energy efficient.[40] Therefore, developing electrocatalysts with minimal peroxide production is essential. Consequently, typically a good ORR electrocatalyst undergoes a direct 4-electron-transfer, exhibits a low overpotential and has many active sites.

1.3.2 Precious state-of-the-art electrocatalysts and their intrinsic activity

Pt-based electrocatalysts are generally acknowledged as the state-of-the-art materials for ORR regarding PEMFC technology, exhibiting superior performance mainly due to their high selectivity and stability. The binding energy of O_2 with Pt often illustrated by volcano plots, is one of the reasons that makes Pt the first choice since the first fuel cell in 1840.[41] The bond must be strong enough for the oxygen to bind to the catalyst, but not too strong so it prohibits the removal of the intermediates.[42] This kind of in-between bond strength is what puts noble metal electrocatalysts generally on top of the volcano curve, which makes them very suitable candidates for the ORR (Figure 6). Nevertheless, there have been works dedicated to further improvement of such noble materials by modulating the particle sizes and morphologies, forming alloy catalysts,[43] or forming core shell structures. As such, the number of active sites and their intrinsic activity may be increased, the loading of precious Pt in alloys is decreased, and the combination of Pt with other metals may lead to a fruitful synergistic effect.[44] When it comes to the intrinsic activity of such materials, it is often depicted in terms of turnover frequency (TOF) which defines the efficiency of the catalyst on transforming the reactant to product, per unit time and amount of catalyst.[45] For TOF determination, it is necessary to evaluate the site density (SD) of the catalyst, which is possible via several methods that have been exhibiting promising results such as: hydrogen underpotential deposition (HUPD), underpotential deposition (UPD) or CO stripping. The principle of these methods is based on measuring the charge generated by the adsorption of a hydrogen monolayer or other metals on the active sites, or the charge needed to strip off the CO already adsorbed on active sites, respectively.[45]

However, even though the intrinsic activity has been demonstrated to be auspicious, the Pt-based materials do not greatly withstand long-term operations without their structure being altered, making their durability inferior.[46] Moreover, due to the difficulty to break the strong O=O bond with an energy of $498\ \mathrm{kJ\ mol^{-1}}$(sluggish ORR kinetics),[47] even Pt-based materials exhibit high overpotentials at low loadings (0.3-0.4 V), generating the need for the usage of high masses for the acquirement of fair performance levels.[48] Thus, it is undeniable that their large-scale usage is not sustainable considering their scarceness and price, which restricts the fuel cell manufacture.[18] Developing electrocatalysts with decreased Pt content would be an effective approach to increase the economic viability of the catalyst, if the activity would not be compromised at some point at low Pt loadings.[49]

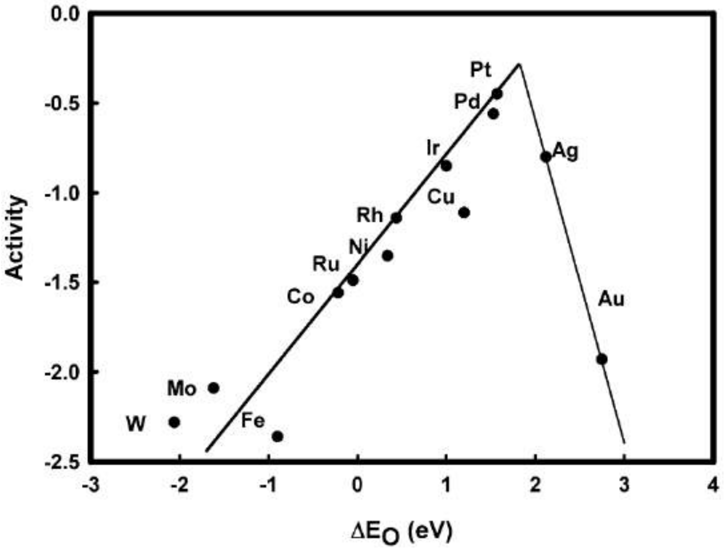

Figure 6 ORR activity versus oxygen binding energy.[50]

1.3.3 Non-precious electrocatalysts and their intrinsic activity

Another strategy is the development of catalytic materials non reliant at all on precious metals. Significant effort has been made by scientists to design and synthesize such materials with the ultimate goal of achieving a performance the exceeds that of noble electrocatalysts. For example metal oxides have been extensively studied, such as MnO_x[51] and Co_3O_4[52] whose morphology plays an important role in the ORR activity apart from the valence status of the metal.[53] However, metal oxides alone do not exhibit good conductivity, hence in practice they are often coupled with a carbon support for a better performance,[54,55] although there may be a competition between the metal oxide and the carbon for O_2 adsorption.[56] Besides, one has limited flexibility in tuning their composition and structure.[57] Multi-metal electrocatalysts have also been studied for ORR, for example spinel-type oxides ($A^{2+}B^{3+}{}_2O_4{}^{2-}$) and Perovskite type oxides (ABO_3), along with Transition Metal Nitrides and Phosphides.[58] Despite transition metal oxides being pre-eminent when it comes to their stability, their electrocatalytic activity remains generally inferior compared to carbon-based materials for example.[59]

Carbon based electrocatalysts have been acknowledged for their reassuring ORR activity considering their high electronic conductivity, surface area and versatile possibilities for tuning their structure and composition.[60] Most commonly such materials are doped with N atoms due to their high electronegativity[61] which leads to high positive charge density in its adjacent carbon atom, ready to adsorb oxygen.[60] This apparently changes as well the position in which oxygen adsorbs from end-on to side-on, where the latter weakens the O-O bond and facilitates 4e$^-$ transfer.[60,62] It was often concluded that a certain type of N in the carbon structure such as pyridinic[63] or quaternary[64] had influence in the activity, however there are studies that refute this hypothesis,[65,66] thus remaining difficult to identify the active centers. However, the majority of these electrocatalysts are investigated only in basic media which is not a very challenging environment for most catalytic materials.[67] Therefore further investigation in acid media is necessary to unravel their potentiality for application in the PEMFC technology.

A particular class of material that has succeeded in the domination of carbon-based and non-precious ORR electrocatalysts are the Fe-N-C electrocatalysts,[68] especially when C stands for carbon nanotubes.[69,70] The simple and abundant precursors is one of the factors that makes them one of the most studied class of ORR materials.[71] Their encouraging activity was accredited mainly to Fe–N_4 active sites,[72,73] postulation made based on the data obtained from various characterization techniques, such as X-ray Photoelectron Spectroscopy (XPS), Mossbauer Spectroscopy, and Time-Of-Flight Secondary Ion Mass Spectrometry (TOF-SIMS).[71] Theoretically, Fe-N_2 active sites are supposed to exhibit the highest intrinsic activity, however that is yet to be proved experimentally.[74] A representation of Fe-N-C sites is shown in Figure 7. However, the active centers in such materials remain not well understood, considering the poor control in the pyrolysis synthesis procedure which leads to various iron environments.[75] In contrast to metal oxides, carbon materials modified with Fe and N exhibit promising electrocatalytic activity, however suffer from poor stability in acidic conditions.[76]

While for metal-based catalysts, the evaluation of SD and intrinsic activity is doable with HUPD, UPD and CO stripping, such methods are not applicable to all materials such as Fe-N-C catalysts, which are less understood and they do not adsorb CO under ambient conditions. Consequently, Luo et al[77] have applied cryo-CO sorption and desorption to evaluate SD and TOF and have evaluated the influence of the preheating cleaning treatment needed prior to the CO sorption in order to remove competitive adsorbates. NO_2^- stripping is another promising technique developed to determine intrinsic activity of Fe-N-C materials[78] it is however a method performed specifically at pH=5.2.[79] Despite these methods being up and coming for the intrinsic activity evaluation of such class of materials, they are not performed in an electrochemical environment similar to what one uses in practice for ORR evaluation.

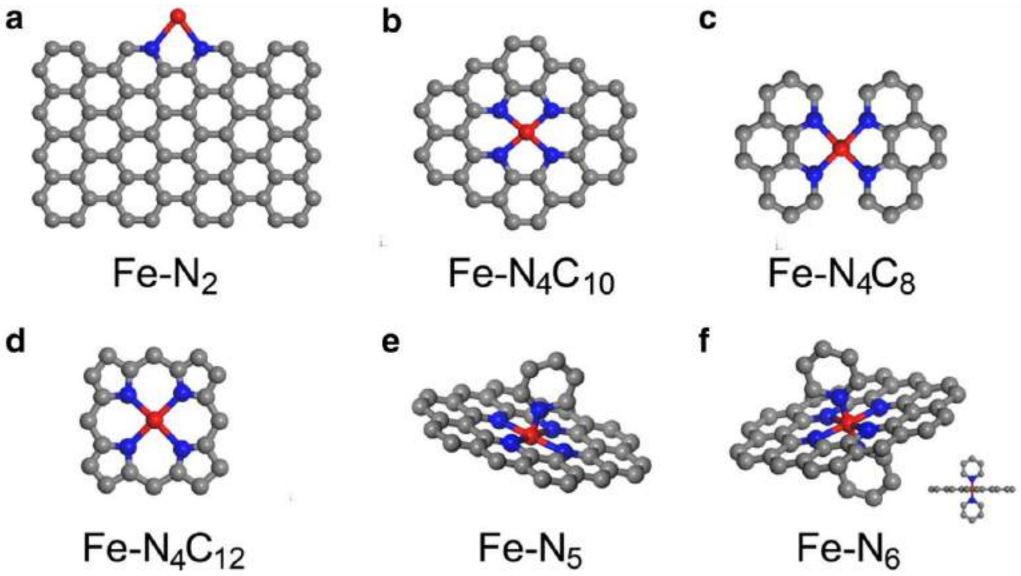

Figure 7 Representation of Fe-N-C sites in a graphene structure. Grey sphere=carbon, Blue sphere-Nitrogen, Red sphere-Iron.[74]

1.4 Conclusion and thesis objective

Transforming the transportation sector into an environmentally friendly one is a key approach to diminish greenhouse gas emissions and global warming. Further developments in FCV which use hydrogen as energy vector has been shown to be a propitious approach to achieve that. However, many challenges need to be overcome to make improvements in that direction and the majority of them are related to ORR electrocatalysis. The complexity of this reaction and the scarceness of the electrocatalytic materials required for it are top research objectives in this field. Therefore, synthesizing and investigating non-precious electrocatalysis is of utmost importance for further developments. The work of this thesis deals with the second aspect, namely the electrocatalyst investigation in the laboratory scale, which often precedes the application of the material on fuel cells. Consequently, it is crucial that the activity acquired in the laboratory reflects the intrinsic ORR activity, which is not always the case when the conventional RRDE methodology used. Accordingly, in this work an exemplary Fe-N-C catalyst is investigated *electrochemically* with several laboratory techniques, with macro (RRDE), micro (SECM) and nano (SECCM) scale resolutions. Bearing in mind that the PEMFC technology is with highest applicative interest, all electrochemical investigations are performed in acid media, pH=1. With this macro-to-nano approach, the potentiality and limitation of each technique will be unraveled with the main goal of acquiring the intrinsic ORR activity and selectivity. Using characterization techniques such as atomic force microscopy (AFM) and scanning electron microscopy (SEM) sheds light onto the agglomerate scale and morphology of the catalyst, which makes the results complete and more comprehensive.

Chapter II: Laboratory electrochemical techniques for ORR investigation

Highly selective catalysts that exhibit low overpotentials are excellent candidates for ORR. However, does this claimed ORR activity in literature usually come from the performance on a MEA? Sometimes that is the case, however the majority of publications refer to the catalytic activity assessed in the laboratory which is a more convenient approach in electrocatalysis research. Synthesizing a non-precious electrocatalyst with high intrinsic activity is indeed crucial in this field, yet the methodology utilized to come to such conclusion, is undeniably just as pivotal. In this chapter, firstly the principles of RRDE, SECM and SECCM as the main electrochemical techniques able to evaluate of ORR activity and/or selectivity are presented. Thereafter, AFM and SEM are introduced briefly, as the main catalyst layer characterization techniques utilized in this work.

2.1 Rotating (Ring) Disc Electrode (RRDE)

RDE is the most common method for a rapid catalyst activity evaluation. It is based on a three-electrode cell where the working electrode (WE) is typically a glassy carbon disc electrode (GCE) surrounded by an insulating material, while the reference electrode (RE) and the counter electrode (CE) choice vary within laboratories. The working electrode is subjected to rotations at certain speeds (convection), where the higher the convection, the thinner the diffusion layer (δ) close to the electrode, leading to a steady state current.[80] The diffusion within the δ transports the reactant to the catalyst.[80] Hence, this apparatus is a convenient means for the quantitative study of electrode kinetics.

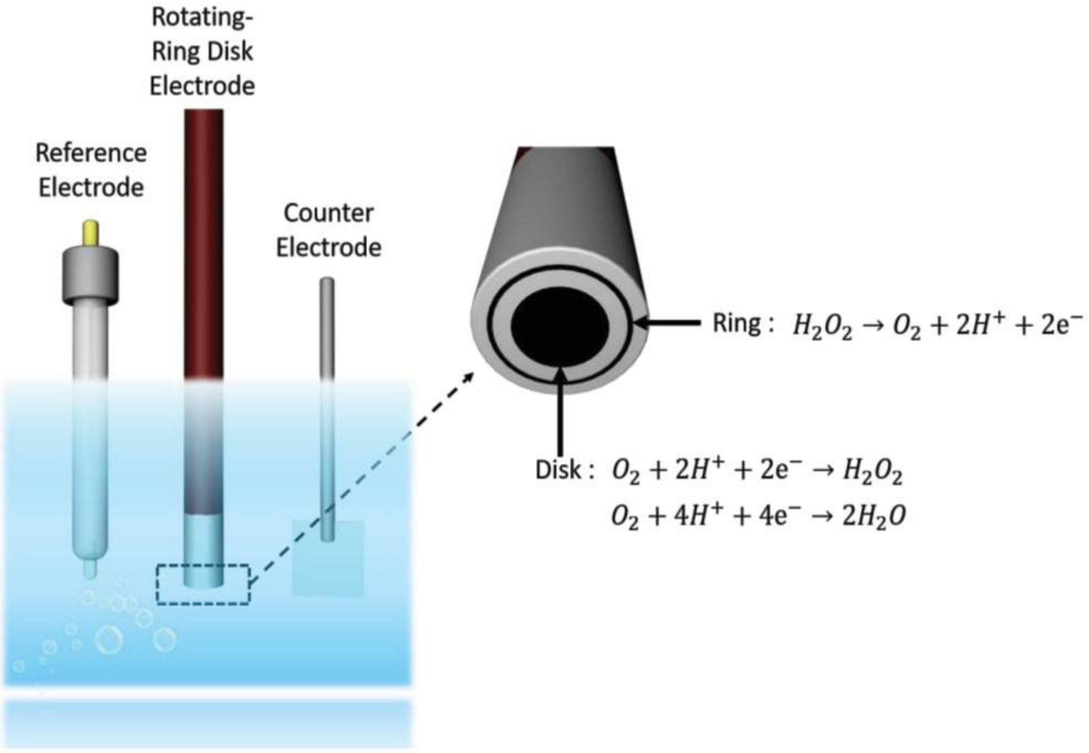

Figure 8 RRDE scheme.[81]

The Koutecky–Levich (K–L) equation is the mathematical expression of current density on the RDE disc and it takes into account the current densities coming from mass transport in addition to the kinetic current density. The formula is depicted in Equation 5, with the j=current density, j_L=current density limited by diffusion, j_K=kinetic current density, and ω=angular velocity. The j_L

parameter represents only the current density that is generated due to mass transport in the electrode, excluding any influence of currents coming from electrode kinetics. It is an important parameter often used to evaluate the performance of the catalyst, and it is expressed by Levich equation (j_L=B*ω $^{1/2}$). The *B* is expressed in Equation 6, where *F* (Faraday constant) =96 485 C/mol, C_{O2}=bulk concentration of oxygen, D_{O2}=diffusion coefficient and v=kinematic viscosity of the electrolyte and n_{O2} = number of transferred electrons.

The j_K on the other hand represents the current density associated to electrode kinetics, and is usually expressed by Butler-Volmer equation presented in Equation 7 where j_o is the exchange current density, often depicted as rate constant, *η* is the overpotential, *α* is the symmetry factor of the reaction, *T* is temperature and *R* is the universal gas constant with a value of 8.314 J·K^{-1}·mol^{-1}. This equation was first derived considering a single-step one-electron transfer reaction.[82] However, if the rate-determining step of the reaction is a one-electron step, it makes the usage of Butler-Volmer equation justifiable even for multi-step processes.[82] Therefore, it remains the most used formula for expressing even the kinetics of multi-step reactions.[83–86]

$$\frac{1}{j} = \frac{1}{j_L} + \frac{1}{j_k} = \frac{1}{B\omega^{\ 1/2}} + \frac{1}{j_k} \qquad 5$$

$$B = 0.2n_{O2}F(D_{O2})^{2/3}v^{-1/6}C_{O2} \qquad 6$$

$$j = j_o[e^{(\alpha nFRT\eta)} - e^{(-(1-\alpha)nFRT\eta)}] \qquad 7$$

The calculation of the number of transferred electrons per O_2 molecule namely *n* was traditionally made with the help of Equation 5, by performing LSVs at different scan rates and then plotting -1/*j* as a function of $\omega^{-1/2}$ (K-L method), where the value of *n* is not meant to be dependent on the other parameters in the equation. However, it has been shown that *n* being constant with potential is not true in reality.[87] Moreover, Bouleau et al.[31] present how for a carbon-based electrocatalyst the *n* varied with ω in a potential range of 0.2-0.7 V vs RHE. Overall, many works show that K-L approach is maybe not perfect for evaluating accurately the number of transferred electrons.[31,87]

Another method for selectivity assessment is RRDE. The setup is similar to RDE except that there is an additional ring electrode (generally platinum) separated by the GC through the insulating material.[88] This ring electrode (WE2) serves for detection of H_2O_2 that may be produced by the sample and works independently from GC (WE1).[89] Quantifying the intermediate produced during ORR is a more straight forward approach to acquire *n*. By detecting the peroxide on the Pt ring, the *n* can be derived through Equation 8 where i_d is the current of the disk electrode, i_r the current of the Pt ring and *N* the collection efficiency of the ring. This information can be used for evaluating the $\%H_2O_2$ as well (Equation 9). This methodology is endorsed by the community for selectivity assessment, therefore in this work the derivation of *n* and $\%H_2O_2$ was done via Equation 8 and Equation 9.

$$n = 4 \times \frac{i_d}{i_d + i_r/N} \qquad 8$$

$$\%H_2O_2 = 200 \times \frac{i_R/N}{i_D + i_R/N} \qquad 9$$

2.2 Scanning Electrochemical Microscopy (SECM)

An alternative to RRDE, a pure diffusion-based technique is scanning electrochemical microscopy, a type of scanning probe microscopy (SPM) which enables the analysis of redox processes in samples by gathering their spatially resolved chemical, electrochemical, and/or topographic specificities. This can be acquired by placing an ultra-microelectrode (UME, typically ≤ 25 µm) at a certain distance from the sample of interest and moving it across the sample (x,y direction), by keeping the UME still (fixed x,y,z), or by moving the UME only on the z direction.[90] The UME is placed along with the sample, counter and reference electrode in a cell and controlled by a potentiostat (Figure 9). Electrochemical information is obtained from the (electro)chemical reactions occurring either at the UME, at the sample, or both. Concerning the probe, the RG is an important parameter which depicts the ratio between the insulating glass radius of the electrode (r_g) and the radius of the active electrode (r_T). This parameter can have an influence on the diffusion hindering of the analyte to the electrode and its value needs to be chosen carefully. Such probe parameters can be determined via SEM images or approach curves.[91] The tip-to-sample distance *d* and tip size have great impact on the spatial resolution.[92] The *d* can be established by performing approach curves,[93] which can then be compared with theory.[94,95] Since the introduction of SECM by Bard et al. in 1989,[96] a great deal of effort has been made by researchers to improve it and to expand its application possibilities. Owing to many advancements of the technique, nowadays utilization of SECM enables researchers to obtain very useful information on a variety of materials for numerous applications.[97–100]

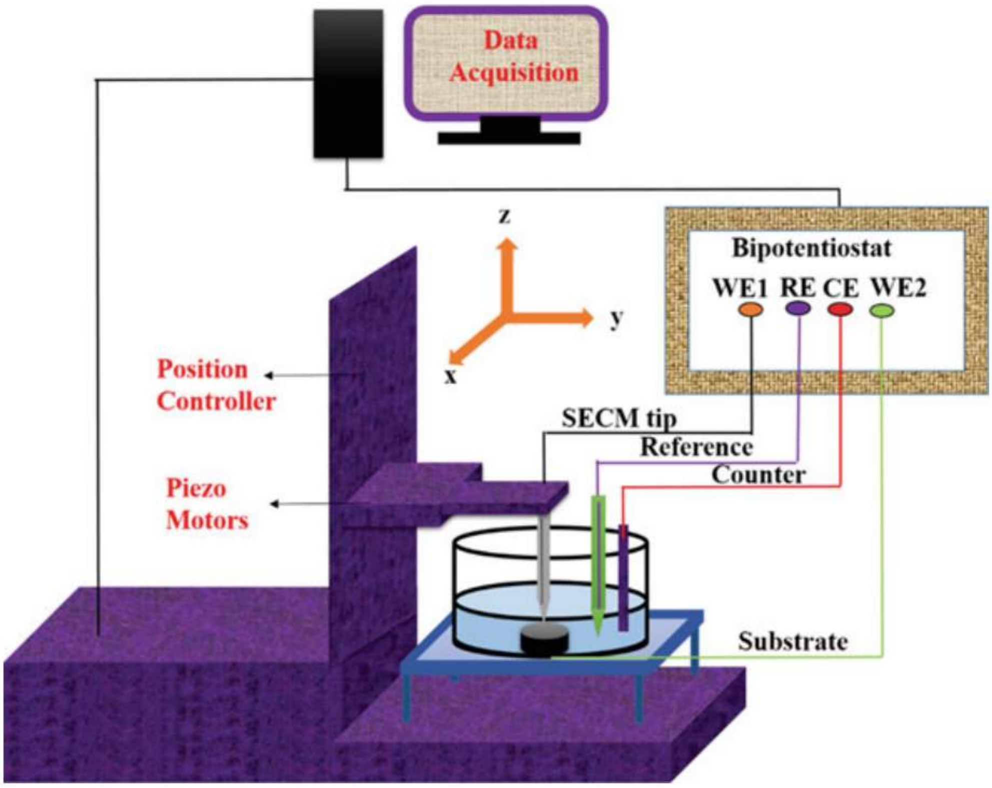

Figure 9 SECM scheme.[101]

While in flat macroelectrodes the diffusion of species occurs in a perpendicular manner and the diffusion layer is thin in comparison to the size of the electrode, in ultramicroelectrodes hemispherical diffusion around the electrode is created and thus promoting higher mass transfer and limiting current densities[102] owing to the geometry (which can be diverse[103]) and the small size of the UME. In this case, the diffusion layer is big compared to the size of the UME. Therefore inhere one can achieve steady state, diffusion limited currents without the need of any convection, leading to an independence of current on the scan rate.[104] Smaller dimensions of the electrode permit a better sensitivity in measurements, and the absence of convection in SECM investigations simplifies the interpretation of results compared to hydrodynamic methods. Moreover, the line scans acquired with SECM can be translated to catalytic activity maps which can give an insight on the current distribution within the catalyst layer. SECM has also found utility in H_2O_2 detection and has some advantages compared to RRDE. Catalyst layers studied with RRDE are often quite thick, in which case H_2O_2 can decompose within the layer before getting in contact with the ring, leading to fewer amounts of intermediate detected.[105] The possibility for this cannot be excluded in SECM as well, however this method allows the study of much lower loadings, decreasing the chances of encountering this problem.

2.2.1 SECM modes

Depending on the purpose of experiment, several modes can be employed by SECM and they will be described briefly in the next sections.

Redox competition (RC) mode

The RC mode was introduced by Eckhard et al. in 2006[106] and it is based on the competition of the sample and tip for the same mediator (oxygen for example), thus undergoing the same reaction (ORR). Let's say we polarize the tip at a negative potential in which ORR occurs. When the tip is approached to the sample by line scans (x, y direction), or if the tip is static above the sample and the sample potential reaches the ORR region, due to the extensive consumption of O_2 by the sample as well, there is less O_2 detected by the tip, hence there is a decrease in the tip current which is measured.[106] The amount of net current that decreases corresponds to the ORR activity of the sample. The RC mode suppresses the background current issue generally encountered with tip generation/substrate collection (TG/SC) mode which was initially used for ORR investigation.[106]

Substrate generation/tip collection (SG/TC) and tip generation/substrate collection (TG/SC) modes

With the generation/collection modes the mediator is produced at one of the electrodes. In TG/SC mode, the redox species (O_2 for example) is generated at the tip and detected thereafter at the sample, thus it is a mode commonly used in ORR activity investigations.[107,108] Due to recent innovations, the O_2 does not have to be generated by an electrode, it can rather be delivered from a micropipette filled with a solution, which can have pumped oxygen at any time of choice, instead of a potential pulse.[109] This mode is called micropipet delivery/substrate collection (MD/SC) mode and it expands the SECM application even to cases when the analyte cannot be electrochemically generated.[110,111] Nevertheless, another commonly used mode is the SG/TC one, where the generation of redox species occurs at the sample, after which they diffuse to the tip and undergo electrochemical reaction.[112] In this case, the current of the tip will grant information about the electrochemical activity of the sample. SG/TC mode is with interest in ORR investigations as the H_2O_2 produced at the sample can be detected at the UME, thus granting the ORR selectivity.[113]

The evaluation of *n* in SECM can be done using the data gathered from reduction of oxygen through RC mode and oxidation of H_2O_2 at the tip via SG/TC mode using the Equation 10 [114] which is similar to Equation 8, except that here the background current is corrected, namely the current at all potentials is subtracted by the current value at the most positive potential at which ORR does not occur. The collection efficiency, *N,* is usually considered 100%, if the ORR and H_2O_2 currents do not change as a function of *d*.[115] However, numerical simulations have been previously performed to validate the value of *N* and it has been estimated to be up to 49% for given experimental parameters, much higher than one can get via RRDE configuration.[116] This is not surprising, considering that in SECM configuration the tip collecting the peroxide is positioned closely on top of the sample, in comparison to RRDE where the Pt ring is adjacent to the disc. Additionally, adapting some experimental parameters such as bigger RG and smaller *d* can also increase the chances to collect more H_2O_2.[117]

$$\mathrm{n} = 4 \times \frac{\Delta \mathrm{i}_{\mathrm{O_2}}}{\left(\frac{\Delta \mathrm{i}_{\mathrm{H_2O_2}}}{\mathrm{N}}\right) + \Delta \mathrm{i}_{\mathrm{O_2}}} \qquad 10$$

Feedback mode

Feedback mode is another widely used mode in the field, described initially along with SECM itself in 1989. Let us consider an oxidized species *O* as a free mediator present in solution that is reduced to *R* by the polarized UME. At a large distance from the sample, the tip exhibits a constant diffusion-limited current i_{ss}, whose magnitude is proportional to the concentration of O and electrode size. As illustrated Figure 10, if the sample is not reactive (an insulator) and the tip approaches it, the hemispherical diffusion will be disturbed and thus the diffusion of O to the tip will be hindered. This will lead to a decrease in the diffusion-limited tip current, known as negative feedback effect.[118] In the case of positive feedback, an electrochemically active sample (a conductor) is approached by the tip. The substrate can thus oxidize the R formed at the tip back to O, thus increasing the concentration of O in the diffusion zone and increasing the tip current.[118] The current normalized by the current measured far from the substrate vs d curves obtained while the tip approaches a conductive or insulating substrate are called approach curves. Concentration and diffusion coefficient of O do not influence the approach curve, as it includes dimensionless variables solely.[90] The degree of current change is dictated by the activity of the sample, enabling the distinction between more and less active spots[118] in the same substrate, the determination of d and of a. The r_g parameter (insulating part of the UME) has the largest influence on negative feedback curves as it hampers the lateral diffusion.[90] As feedback mode measures the current only at the tip, it is convenient to use in cases when the substrate cannot be polarized.

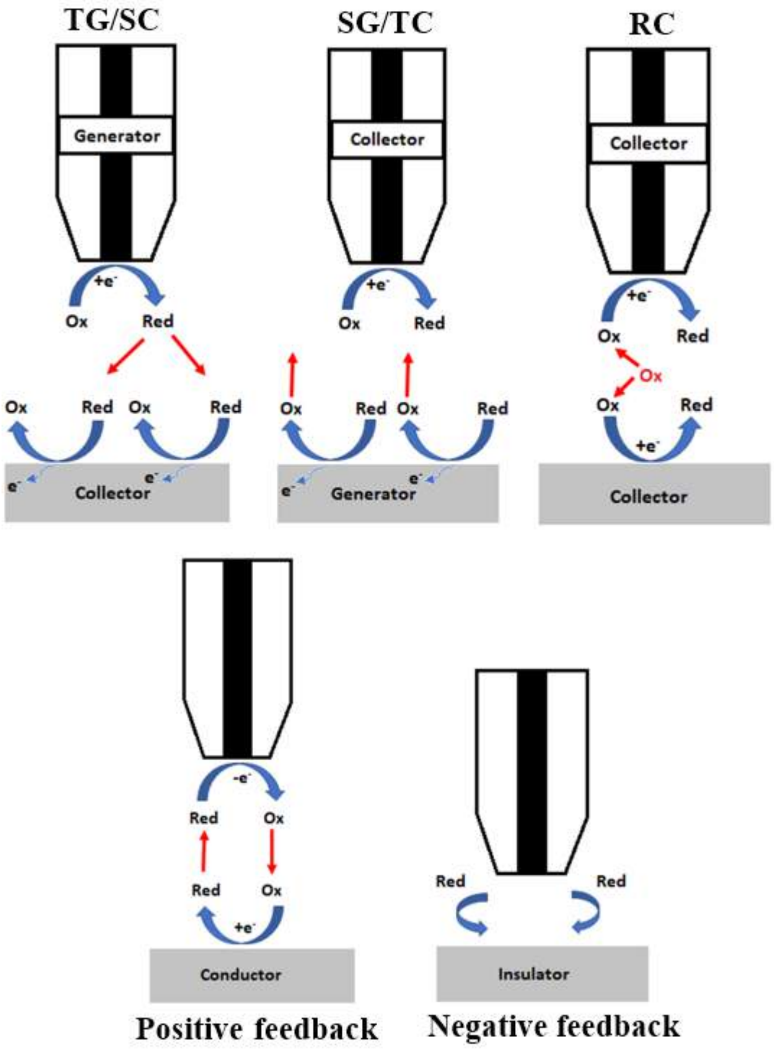

Figure 10 Scheme of SECM modes.

2.3 Scanning electrochemical cell microscopy (SECCM)

Another SPM technique which is promising for ORR investigation and permits nano-scale resolutions is scanning electrochemical cell microscopy (SECCM), a technique based on an electrolyte-filled, dual or single-barred pipette, with a reference electrode in the channel(s).[119] A droplet is formed at the end of the pipette and when it is in contact with the sample a feedback current is generated and one can perform electrochemistry within the confined meniscus. Once a potential is applied between the electrodes, ion and electron-transfer occurs through the droplet meniscus. This results in modulations of substrate surface current (i_{surf}) which serves as a feedback signal for probe positioning. The pipette moves laterally across the surface at a certain *d* or hopping mode, during which the current signals are recorded.[119] This technique enables the imaging of electrochemistry, conductivity and topography of samples, simultaneously.[120] The fact that only a small part of the sample is in contact with the solution very briefly, makes SECCM an encouraging method for investigating samples sensitive to corrosion, passivation or surface fouling.[121] The configuration in the SECCM technique also ensures high O_2 diffusion that comes from the barrel of the pipette and the liquid-air interface of the meniscus.[122] There are however fewer reported works regarding ORR investigation with SECCM, for example Tetteh et al.[123] studied ORR of a complex solid solution (CSS) revealing heterogeneities in activity when scanning with a nano-sized pipette. Moreover, Byers et al.[124] studied single walled carbon nanotubes (SWCNT), with high resolution SECCM revealing that the SWCNT alone are active for ORR, rather than only a carbon conductive material that one usually uses as support for the catalyst. However, SECCM principles are a bit distinct when compared to SECM. Mostly because herein, there is only the substrate (sample) as the unique working electrode, while the pipette is only filled with electrolyte and with the reference electrode. This implies that while the ORR activity can be investigated, there is no means to detect the product generated by the sample (H_2O_2). Therefore, the SECCM set-up cannot provide information about the catalyst's selectivity towards ORR. Nevertheless, one exceptional advantage of this method is the feasibility of acquiring resolution of up to a few nanometers due to the easy fabrication of nanopipettes which takes only a few minutes. In theory this is also possible with SECM as 10 nm Pt nanoelectrodes have been fabricated,[125] however the experimental wrestle to achieve that makes it much more challenging, especially in the case of gold nanoelectrodes which might take days if not weeks. Another advantage of this method is the reduced time needed for acquiring high resolution images with hundreds to thousands of measurement points.[126]

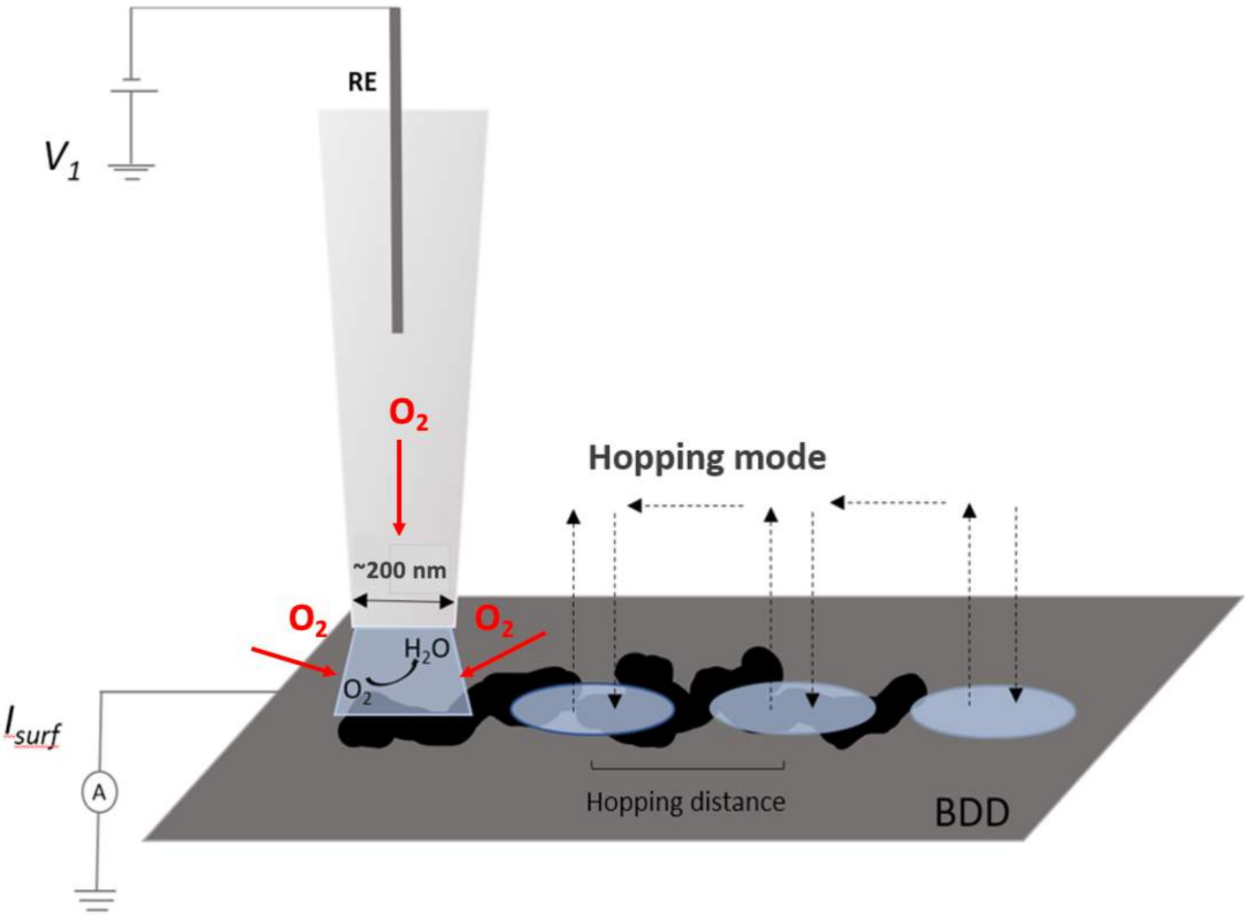

Figure 11 SECCM scheme in hopping mode.

2.4 CL structure characterization techniques

The above-mentioned techniques give crucial information about the catalyst activity, however often that is not complete without an additional observation of the sample in order to better understand the investigated material. In the following section, the main techniques used in this work for CL characterization in addition to optical images will be presented, namely Atomic Force Microscopy (AFM) and Scanning Electron Microscopy (SEM). In this thesis, while AFM was used in combination with SECM to have information about the CL agglomerates, SEM was used in combination with SECCM to get more in-depth insight on the morphology of each studied agglomerate.

2.4.1 Atomic Force Microscopy (AFM)

AFM is a scanning probe technique which measures attractive or repulsive interactions between a sharp tip on a flexible cantilever and a sample under investigation. After the cantilever approaches the surface, it gets deflected by the interactions with it in accordance with Hooke law.[127] This deflection is measured thanks to a laser beam and a photodiode and holds information about the sample[127] while the sample or the tip are moved by a piezo scanner. There are certain possibilities of AFM operation, such as by contact, noncontact, static or dynamic mode for which a comprehensive introduction was made by Haugstad.[128] AFM is mostly used for assessing surface topography, morphology, and roughness. When AFM features are joined with the ones of SECM, their features merge and allow the correlation of topographical and electrochemical information of the sample with high resolution. AFM can be used to determine the particle sizes and catalyst volume of the same deposit that is investigated under SECM.

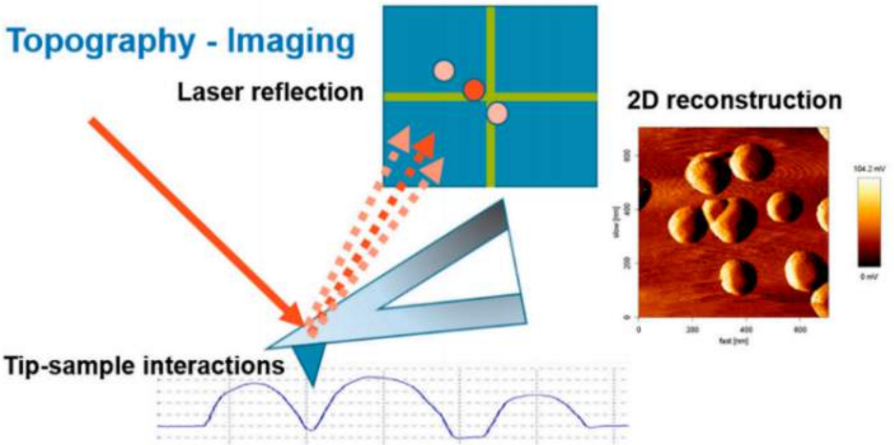

Figure 12 Scheme of AFM working principle.[129]

2.4.2 Scanning Electron Microscopy (SEM)

It is known that despite the wide range application of optical microscopy, in the world of nanomaterials it fails to give information due to its limited resolution.[130] Electron microscopy (EM) techniques liberate us from this limitation allowing ultra-high resolutions up to a few nm. One of the EM techniques crucial in the field of nanomaterials is SEM, a technique whose principle consists on scanning the sample with an electron beam from an emission source and ejecting electrons from the sample surface, electrons which then are captured by a detector. Transmission Electron Microscopy (TEM) is another EM technique which can provide a higher resolution than SEM.[131,132] The latter is widely used to determine the size and morphology of nanomaterials.

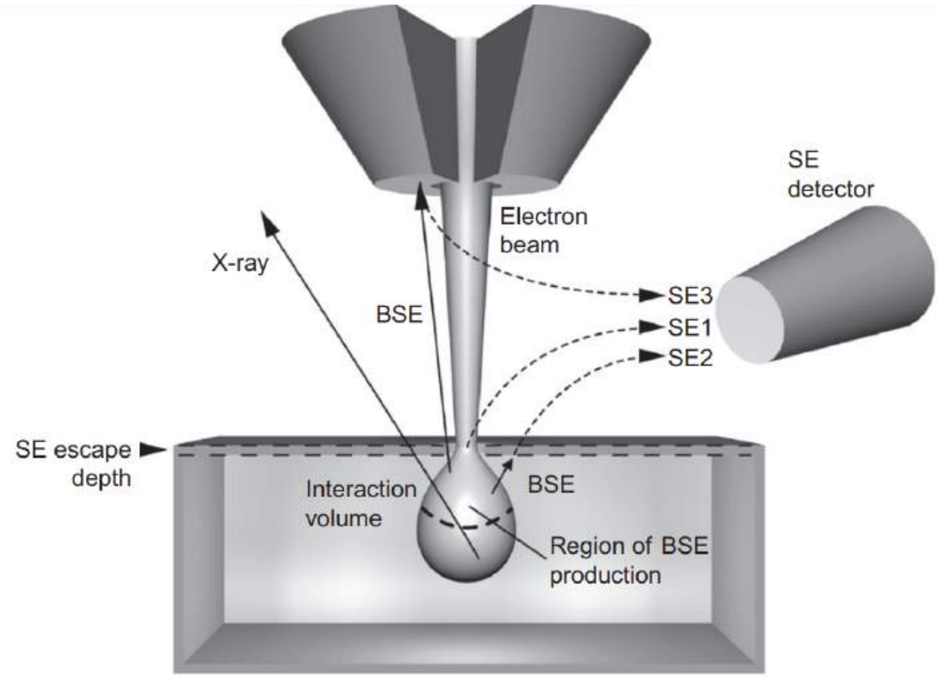

Figure 13 SEM working principle scheme[133] BSE stands for backscattered electrons while SE for secondary electrons. These and X-ray are only some of the electrons which can be ejected from several depths of the sample.

2.5 Conclusion

In this chapter, the electrochemical characterization techniques utilized in this thesis were presented. Starting with RRDE as the conventional methodology used mostly in the community and following with SECM as a technique with similar working principles, yet with different phenomena manifesting in microelectrodes. Thereafter, SECCM as an up-and coming technique in the field was introduced. The working principle of all these techniques was explicated. Finally, a brief presentation of SEM and AFM was made, as the main CL characterization techniques employed in this work. While the former can give insight on the morphology of the catalyst, the latter can be used to unravel the agglomerate size and distribution in the CL.

Chapter III: RRDE study-key challenges in acquiring intrinsic ORR activity and selectivity

In this chapter, the macroelectrode-based RRDE method is employed for the electrochemical investigation of the non-noble Fe-N-MWCNT catalyst. After introducing the common RRDE problematics in the field, the chapter continues by presenting the ORR performance of the catalyst. It is demonstrated how the electrode coverage and amount of material deposited on the electrode affect the ORR activity and selectivity. A hypothesis explaining the less sigmoidal shapes of voltammograms at lower loadings is proposed. Finally, the effect of catalyst ink processing condition on the voltammogram shape and number of transferred electrons is presented.

3.1 RRDE as a conventional ORR investigation method

Research towards the synthesis and design of non-precious ORR electrocatalysts is vastly increasing in the field with plenty of auspicious materials exhibiting encouraging results.[69,134] The results usually refer to the performance acquired in laboratory scale, namely with RRDE as a convenient, rapid, and undoubtedly the most widely used technique for preliminary evaluation of electrocatalytic materials. Nevertheless, as the ultimate goal is the integration of the electrocatalyst on a FC, the excellent activity acquired in laboratory might be unavailing knowing that the performance acquired with RRDE for Pt-free materials generally does not match the one acquired via MEA studies.[1] Since it is indeed a well-established method for decades, there is a chance that nowadays it is being taken for granted while the ultimate focus stays on the research of new synthesis strategies for materials. With an example to start with, one barely encounters micrographs of deposits on the GC electrode, even though the electrode coverage and smoothness of layer can certainly impact the outcome.[135,136] Moreover, when Pt-free materials are investigated, higher electrode loadings tend to be utilized compared to Pt/C[63] which often overestimates the performance.[137] This approach is usually employed because higher loadings tend to exhibit higher selectivity and better diffusion plateaus compared to lower ones.[138] However, does that represent the intrinsic selectivity of the catalyst which should allegedly be independent of mass? Identifying and addressing the problematics that prohibit acquiring pivotal information about catalysts activity is necessary in the field in order to go steps closer into resolving them. Some researchers have indeed tackled such issues related to appropriate experimental protocols employed in RRDE. In a recent publication, Bouleau et al.[31] make an excellent encapsulation of loading, Nafion, carbon grinding and selection of upper potential influence on the ORR catalytic activity. Garsany et al.[136,139] have as well stressed the importance of electrode coverage and quality of catalyst film on the ORR outcomes. In this chapter, the influence of catalyst loading, electrode coverage and ink processing condition on ORR activity and selectivity is presented. An observation not properly interpreted until now is the change on voltammogram shape with loading, which is tackled herein.

3.2 Catalyst ink dispersion methods-ultrasonic bath and ball milling

Graphitized carbon nanomaterials are well known for their hydrophobicity and their tendency to aggregate due to Van der Waals and electrostatic interactions[140,141] leading to challenges regarding their dispersion in aqueous solutions. Consequently, processing the catalyst ink prior to the electrochemical study is a common practice in order to acquire mixtures as homogeneous as possible with abundant triple-phase boundaries. Up to now, the most common processing method used by the community to overcome the aggregation of carbon nanomaterials is ultrasonication of the catalyst ink.[142,143] The principle consists on the generation of ultrasonic waves by an inducer, which create gas-and vapor-filled microbubbles upon travelling through the medium. After reaching a maximum size, the microbubbles collapse by generating local extreme conditions with high pressure, high temperature, and H* and OH* radicals created by water synolysis.[144,145] These so-called 'hot spots' are accounted for the breaking of agglomerates in the material.

Another approach for dispersing carbon-based catalysts is by mechanically breaking the agglomerates through agitation of the ink containing ZrO_2 beads inside, in which case the collisions and friction of the beads with each-other and with the container, transfers the mechanical energy to sufficiently break the particles.[146] Studies have shown that ball milled inks exhibit higher viscosity and higher stability of agglomerates.[147] Higher current densities and generally better MEA performance has been obtained with mechanical ball milling processing compared to solely ultrasonicated inks.[148,149] This enhancement in performance was mostly correlated to the sufficiently decreased particle size,[150] easing the access of oxygen to active sites (Figure 14). Despite the fact that ball milling has prospered, ultrasonication treatment of catalyst inks still dominates in laboratory scale protocols. Consequently, in this chapter, inks acquired with ultrasonication processing and ball milling were studied subsequently with RRDE.

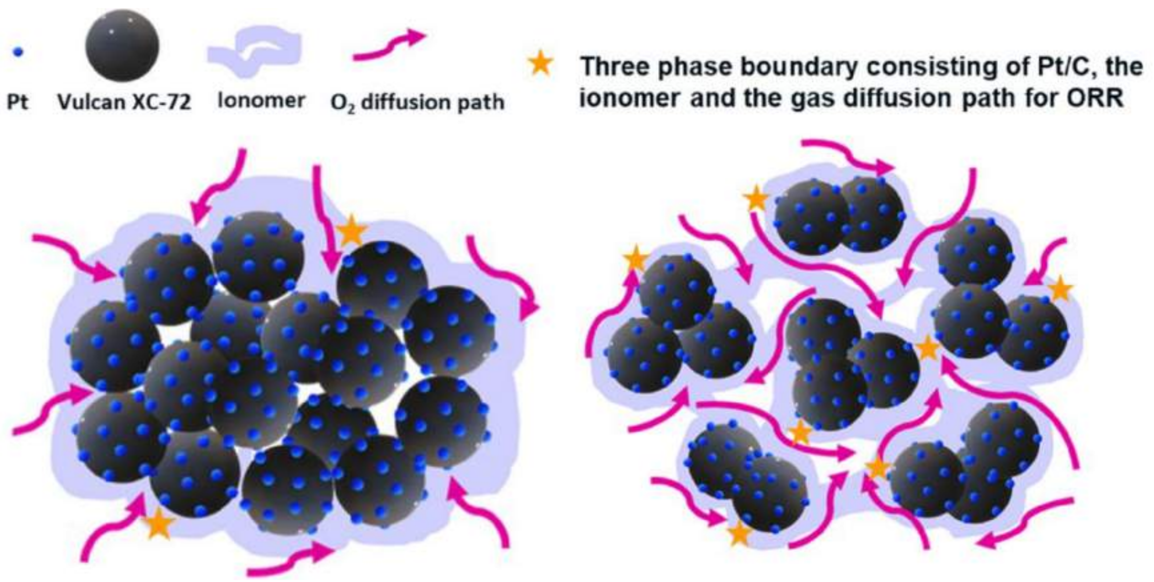

Figure 14 Different catalyst dispersion leads to big or small agglomerates, thus affecting oxygen access to active sites.[151]

3.3 Experimental

3.3.1 Catalyst Ink preparation

The ball milling ink (bm-ink) was prepared by dispersing 120 mg of Fe-N-MWCNT catalyst powder (synthesis in Annex I) in a mixture of 1440 mg Nafion solution (5 wt. % in lower aliphatic alcohols and water, contains 15-20% water, ref 274704, from Sigma Aldrich), 2925 mg isopropanol (99.5 % from Thermo Fisher Scientific Chemicals) and 975 mg water, obtaining a concentration of 19.56 mg/mL in catalyst. The Nafion percentage in this formulation is about 37.5 %. This ink was mixed with 10 g zirconium (Zr) spheres (from Retsch) and treated for 1 hour in IKA ULTRA-TURRAX® Tube Drive for first grinding. Afterwards, the same ink was left for 2 weeks in IKA ROLLER 6 shaker. Additionally, the ink was treated for 30 minutes in ultrasonic bath before each measurement. The ultrasonicated ink (us-ink) with the same concentration (19.56 mg/mL) was prepared by dispersing 24 mg catalyst on 660 µL isopropanol, 220 µL, water and 350 µL Nafion solution (5%) and then treated on ultrasonic bath (VCX 750 from Sonics materials equipped with a Cup Horn) for 1 hour. Likewise, before each measurement the ink was left 30 minutes on ultrasonic bath.

3.3.2 Electrochemical measurements

The GC electrode with an area of 0.196 cm^2 and a platinum ring (RRDE electrode from Pine Research) was polished with 200 Å alumina suspension (99.98 % from Presi, Grenoble) for 10 minutes before each measurement. Amounts of 0.23, 0.7, 1.6, 3, and 5 µL ink were drop-casted in the GCE for achieving the loadings 23, 70, 160, 300, and 500 µg/cm^2 respectively. The 0.23 and 0.7 µL were deposited in one drop, while the other loadings in two equal drops followed by drying in open air. All experiments were conducted in 0.05 M H_2SO_4 electrolyte (99.999% from Sigma Aldrich), bubbled with oxygen for at least 30 minutes prior to each experiment. A saturated calomel electrode (SCE) was used as a reference electrode and a carbon rod as counter electrode. The potentials in the results section are all converted to reversible hydrogen electrode (RHE) via Equation 11, where the pH in the electrolyte used herein is equal to 1 and the standard potential for SCE ($E^o_{(SCE)}$) is 0.241 V.[152]

$$E_{RHE} = E_{SCE} + 0.059\, pH + E^o_{SCE} \qquad 11$$

Onset potentials (E_{onset}) correspond to the potential value at a current density of 0.1 mA/cm^2. Cyclic voltammograms (CVs) were performed in order to take into account the capacitive current, in a potential range between -0.3 V and 0.8 V vs SCE and a scan rate of 5 mV/s. This scan rate is a good compromise for approaching steady-state behavior, as higher ones could give an apparent kinetics artificially improved, while much lower ones could invoke artifacts coming from the accumulation of impurities in the electrolyte at the WE.[139] Even though the capacitive current was small, the average current from the forward and the backward scan of CV was used in all calculations, and we refer to all voltammograms as LSVs. Simultaneously, chronoamperograms (CA) on the platinum (Pt) ring were recorded by applying a constant potential of 1.0 V vs SCE, a potential value where H_2O_2 oxidation peak was observed. Calibration of the Pt ring was performed by gradually adding peroxide in the electrolyte while the ring is polarized at 1.0 V vs SCE, in order to ascertain its good sensitivity to H_2O_2 detection, as shown in Figure 15. The calibration curve is a straight line with a coefficient of determination R^2 of 0.99, while slope calculated herein is 0.35788. The background current of 0.005 mA could correspond to the oxidation of small amounts of impurities present in the solution.

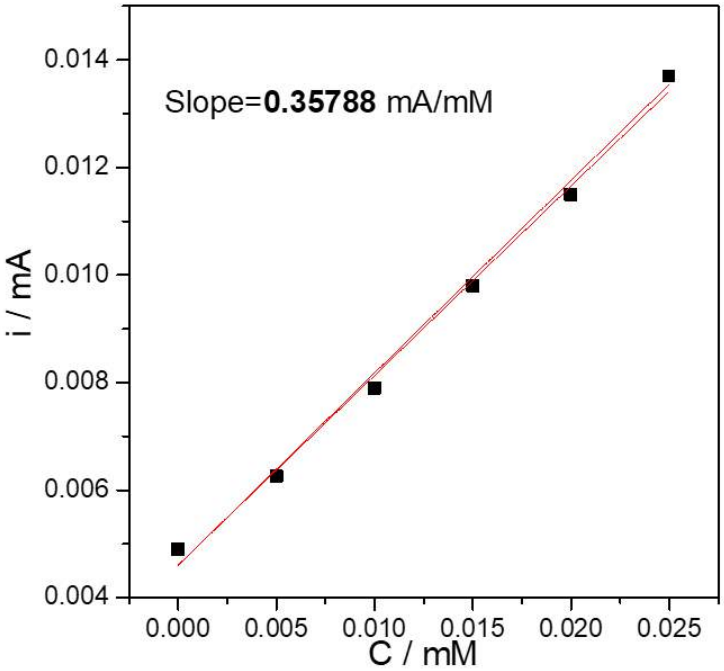

Figure 15 Calibration curve obtained from CA currents recorded at the Pt ring (polarized at 1.0 V vs SCE) at different concentrations of H_2O_2 in the electrolyte.

The voltammograms were carried out in different rotation speeds, namely 400, 800, 1200, 1600 and 2000 rotations per minute (rpm) while the presented voltammograms in all figures correspond to 1600 rpm. The collection efficiency of the Pt ring (N) was determined using a standard procedure from BioLogic (EC-Lab-Application Note #07 2004), using a $Fe(CN)_6^{4-}$ solution ($5{\cdot}10^{-3}$ M) with KCl (0.5 M) as supporting electrolyte. The disc is swept from 0 to 1 V vs SCE in which case the Fe (II) species is oxidized to Fe (III), while the ring is polarized at 0 V to reduce back the Fe (III). Dividing the corresponding ring and disc currents gave access to the collection efficiency $N= -\frac{i_{ring}}{i_{disc}}$ =0.21. This value is what is commonly found in literature and is considered relatively low, due to the limitations imposed by the geometry of the working electrodes, namely the Pt-collection ring placed on the side of the GC disc where the intermediate is generated (Figure 8), which is an unfavorable position to catch the maximum amount of peroxide. The *n* and %H_2O_2 were calculated with Equation 8 and 9 respectively.

3.4 Us-ink-ORR performance at different loadings

3.4.1 Selectivity-peroxide production and number of electrons

Initially, the catalyst ink processed by ultrasonication was drop casted in different amounts in a GC disc electrode. As the current is divided by the geometric area of the electrode leading to current density, it is crucial that the coverage of the GC disc with catalyst is as high as possible. In order to have a better control in that, micrographs of each studied deposits were taken as shown in Figure 16. Herein one can see that as the loading gets lower, it is more challenging to cover well the whole area, thus loadings lower than 23 μg/cm^2 were not able to be acquired. Higher loadings than 500 μg/cm^2 were not studied, considering that their high roughness could disturb the diffusion layer and thus lead to overestimated currents, higher than the j_L predicted by Levich equation.[153] Nevertheless, the selectivity of the respective deposits was acquired by detecting peroxide currents at the Pt ring, simultaneously while the LSV occurs at the GC disc. The percentage of H_2O_2 was calculated via Equation 9 using the disc and the ring currents and was plotted versus the potential applied at the disc (Figure 17a). The shape of $\%H_2O_2$ curves show a decreasing peroxide percentage detected at more negative potentials (0-0.2 V vs RHE), which may be correlated to the higher rate of H_2O_2 reduction to H_2O at such conditions.[154] It is also shown in Figure 17a that the peroxide detected decreases significantly with an increase on catalyst thickness, where the lowest loading exhibits a peroxide percentage as high as ~45%, while the highest loading only ~12% at 0.57 V. At more negative potentials (0 V vs RHE) the percentage varies from 7% to 20% for highest and lowest loadings respectively. The corresponding values of n acquired via Equation 8 are shown in Figure 17b where it is evident that the n varies throughout different potentials and increases from ~3.25 to 3.75 (at 0.57 V vs RHE) from the 23 to 500 ug/cm^2 deposit, while at 0 V vs RHE the n increases from ~3.62 to 3.85. Higher peroxide detection for lower loaded deposits is in accordance with what was observed previously for carbon based materials.[138,155–157] This was attributed to the larger diffusion path of H_2O_2 in thicker layers, possibly leading to a further electrochemical or chemical reduction of H_2O_2 to H_2O within the layer, prior to getting released to the electrolyte.[154] There are also works that have correlated this to the higher microporosity of the material at higher loadings, in which case the micropores would aid H_2O_2 adsorption and its reduction.[158] In fact, H_2O_2 disproportionation to O_2 and H_2O within the layer is as well possible. However, this variation in selectivity makes it difficult to come to a conclusion as to what is the intrinsic *n* of the catalyst.

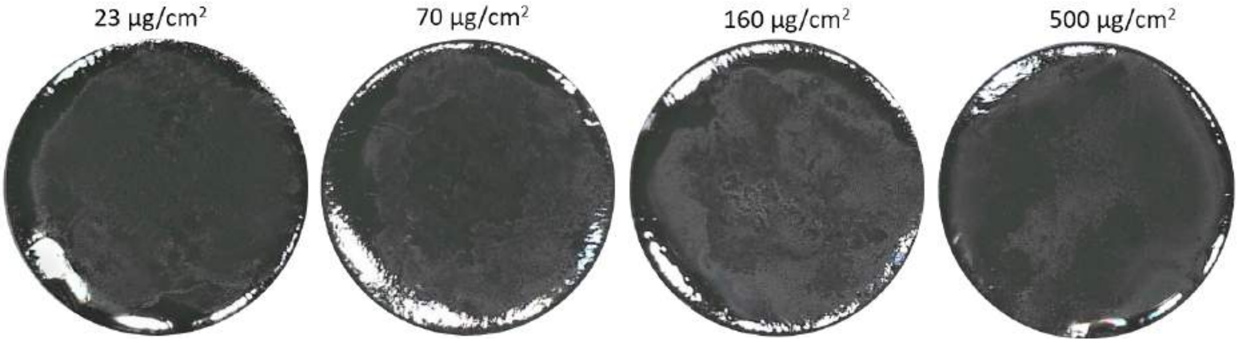

Figure 16 Micrographs of the studied deposits. GC disc covered with different amounts of Fe-N-MWCNT catalyst (us ink).

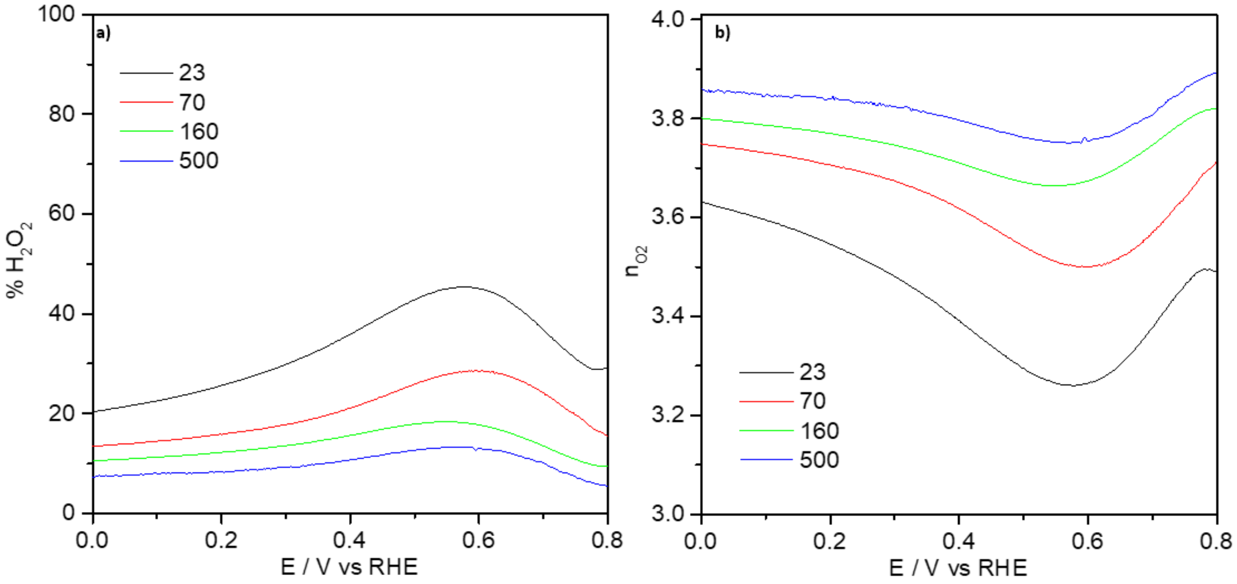

Figure 17 a) Peroxide percentage detected at the Pt ring vs the potential applied at the disc for different loadings (µg/cm²), b) the corresponding *n* values. Experiments obtained for us-ink of Fe-N-MWCNT catalyst in O_2 saturated 0.05 M H_2SO_4 at a scan rate of 5 mV/s, corresponding to the measurement at 1600 rpm.

3.4.2 Voltammograms and the evolution of their slope

The LSVs recorded at the disc for the all the deposits are shown in Figure 18a, where one can recognize an increase of the current density at 0 V vs RHE (*j*(E=0V)) and more positive overpotentials at higher loadings (values in Table 1). While better kinetics is anticipated with an increase in mass thus active sites, the *j*(E=0V) change is rather unpredicted. The reason for this might be the fact that at lower loadings, the ink is not as well distributed, leaving more uncovered spots in the electrode. As such, the covered electrode area is smaller and as the O_2 diffusion occurs in parallel with the electrode, the current density values will be smaller too.[159] This outcome is often observed in previous works.[31,158,160] Nonetheless, something interesting about the LSV curves in Figure 18a is also their shape variation with loading, namely the diffusion plateau is more evident at higher loadings. To better quantify this, the first derivative of the LSV curves (*dj/dV*) was acquired in Figure 18b, depicting the slope of the voltammograms. Firstly, neither voltammogram exhibits a symmetrical bell shaped gaussian derivative curve, which would imply an ideal sigmoidal LSV curve.[153] Secondly, the maximum *dj/dV* value is increasing with loading, from ~5 $mA/cm^2{\cdot}V$ for the lowest loading to ~14.5 $mA/cm^2{\cdot}V$ for the highest one. A higher *dj/dV* value (more sigmoidal-shaped curve) at higher loadings is somewhat counter intuitive when one considers that at higher thicknesses, there is longer O_2 diffusion paths which should be disadvantageous by prohibiting the access to the majority of active sites far from the surface of the catalyst layer. Same limitation could be predicted for the electrons that have to flow from the electrode throughout the CL (Figure 19). Therefore, one would expect an ohmic drop leading to a less sigmoidal shape of the curve at higher thicknesses. Moreover, high slopes have been associated to fast 2+2 e^- mechanism or a direct $4e^-$ one, with minimum peroxide production.[161] This is in disagreement with many published works where catalysts with highly selective H_2O_2 production have shown well defined sigmoidal voltammograms,[162–164] as well as catalysts with close to four electron transfer which have exhibited non-sigmoidal slopes.[65] Even though the variation of slope with loading was well noticed in previous studies,[138,153,165] the elucidation of such observation is rather dissatisfactory in literature. Therefore, in the next section we propose a possible cause leading to non-sigmoidal shaped voltammograms.

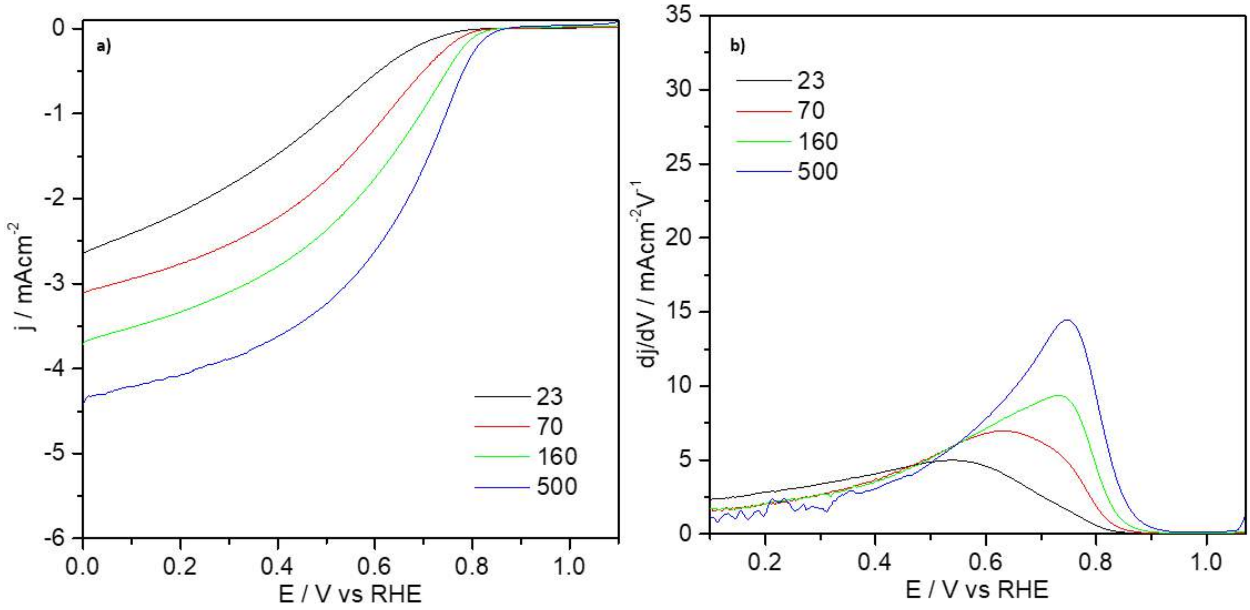

Figure 18 a) ORR LSV curves for us-ink of Fe-N-MWCNT at different loadings (µg/cm^2) at 1600 rpm, b) the corresponding first derivative of the respective curves. Experiments obtained in O_2 saturated 0.05 M H_2SO_4 at a scan rate of 5 mV/s. Results correspond to deposits acquired with us-ink.

Table 1 $j_{(E=0V)}$ and E_{onset} values extracted from Figure 18.

Loading/µg/cm^2	23	70	160	500
j(E=0V)/mA /cm^2	-2.64	-3.11	-3.71	-4.42
E_{onset} / V vs RHE	0.74	0.78	0.80	0.82

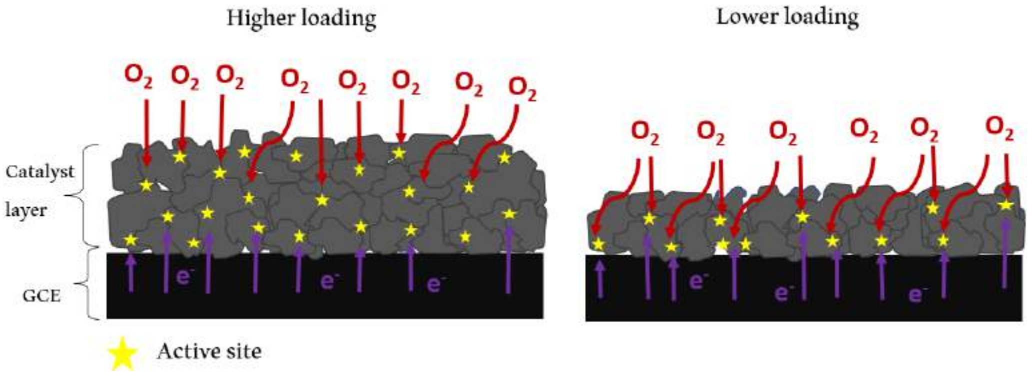

Figure 19 Scheme illustrating the (predicted) hampered access of O_2 and electrons to active sites at higher loadings compared to more feasible access at lower loadings.

3.5 Hypothesis on the origin of voltammogram slope

Considering that voltammograms are typically the first source of information in ORR electrocatalysis, understanding the origin of their shape could have important implications on the interpretation of results and performance predictions for MEA studies. A low slope deviating from the sigmoidal shape in RDE voltammograms would certainly suggest poor current densities on a MEA, generating the necessity to further investigate this matter.

Let's zoom into the electrochemical area in the CL where the charge transfer occurs. This is a complicated media involving numerous processes such as electron and proton transport throughout the CL (characterized by $R_{\mathrm{T,e-}}$ and $R_{\mathrm{T,H+,}}$ respectively), electron and proton transport on the catalyst agglomerates (characterized by $R_{\mathrm{agg,e-}}$ and $R_{\mathrm{agg,H+}}$ respectively, Figure 20a), charge transfer (R_{CT}) and double layer charging (C_{DL}) within agglomerates. If we present these phenomena in terms of electrical circuit, we would have a circuit like in the Figure 20b.

Safari and Delacourt[166] have introduced the concept of intraparticle resistance, where the inner part of the particle experiences a screened potential rather than the applied one (E_{app}-RI). This screening effect was injected into a modified Buttler Volmer equation, similarly as what was done previously by Alice Boudet to interpret SECM results.[167] We make a hypothesis inspired by this theory, where the particle in our case is an agglomerate with a flowing current (i_{local}) and with a certain screening or ohmic effect ($\mathrm{R}i_{\mathrm{local}}$). If for example, we double the number of agglomerates, for a given current, the distribution of the total current onto more agglomerates will halve the flowing current in one agglomerate (i_{local}), thus decreasing the screening effect too. If again we describe this in terms of electrical circuit, adding parallel resistances (more catalyst) would lead to a smaller equivalent (total) resistance (Figure 20c). This explains why at lower loadings (less agglomerates) we observe more screening effect, while at higher loadings (more distributed current and lower i_{local}) we have more sigmoidal shaped curves. In this case, the transverse electron and proton resistances are negligible because considering them a limitation does not justify the experimental observation.

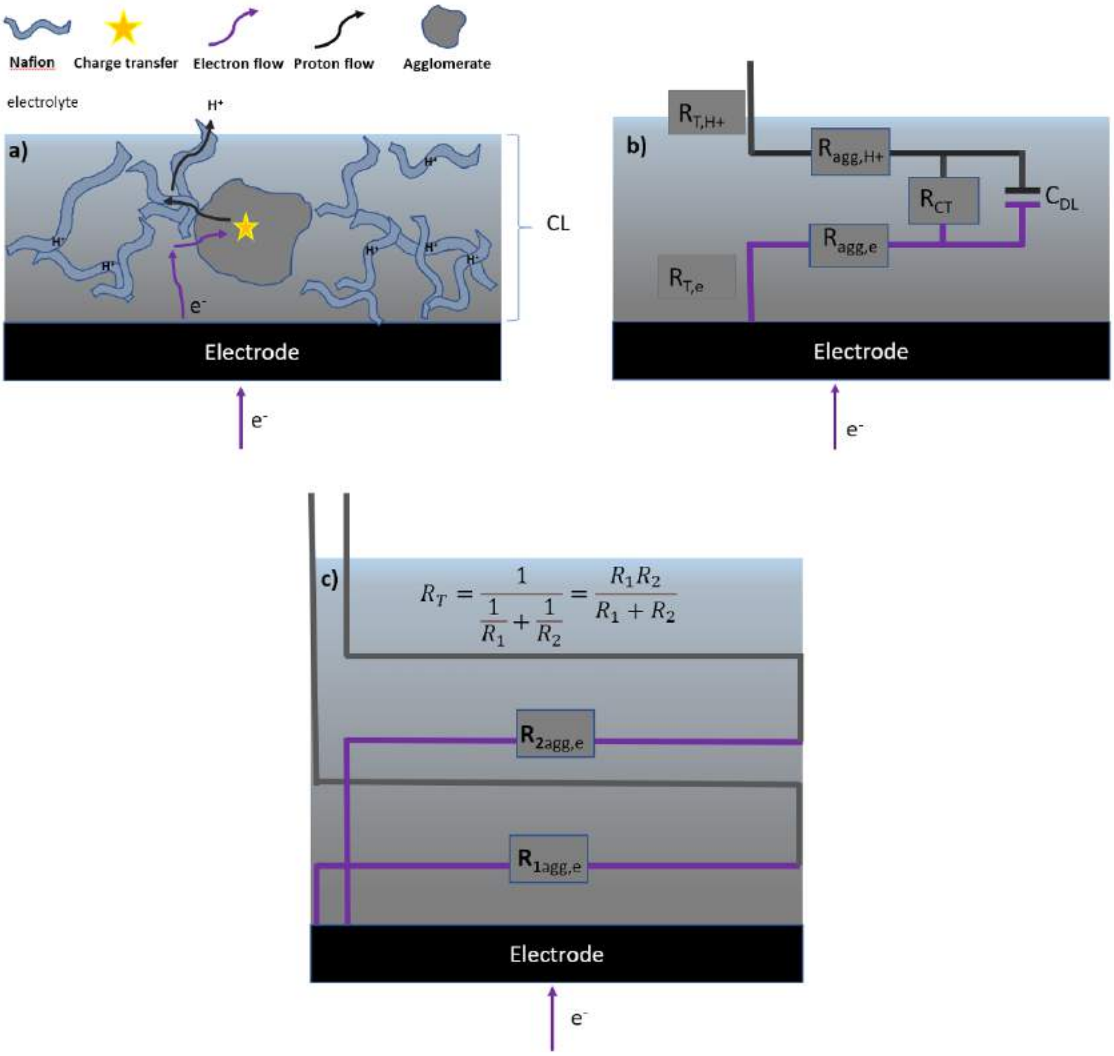

Figure 20 a) Scheme illustrating the charge transfer process, namely electrons travelling throughout the layer, entering inside a catalyst agglomerate, undergoing charge transfer, followed by protons getting out of the agglomerate and finally travelling throughout the layer to reach the membrane, b) representation of the previous scheme in terms of electrical circuit, where $R_{T,e}$ is the resistance of the transversely moving electrons within the layer, $R_{agg,e}$ is the resistance coming from electrons flowing inside the agglomerate, R_{CT} is the resistance of charge transfer, C_{DL} is the double layer capacitance, $R_{agg,H+}$ is the resistance of protons inside the agglomerate and $R_{T,H+}$ is the resistance of protons flowing transversely within the layer, c) electrical circuit representation in the case of adding one more agglomerate (higher loading) while considering the resistance inside the agglomerate as the only limiting factor, while other resistances are negligible.

In order to confirm this hypothesis, the model was put in equation and solved numerically by Alice Boudet. Roughly explained, the screened potential and the loadings were taken into account in the Butler Volmer Equation. The latter was then solved via the finite element modeling software Comsol Multiphysics, enabling the plotting of theoretical voltammograms. As shown in

Figure 21, this model was able to reproduce the evolution of the shape with loading and derivatives of the experimental voltammograms.

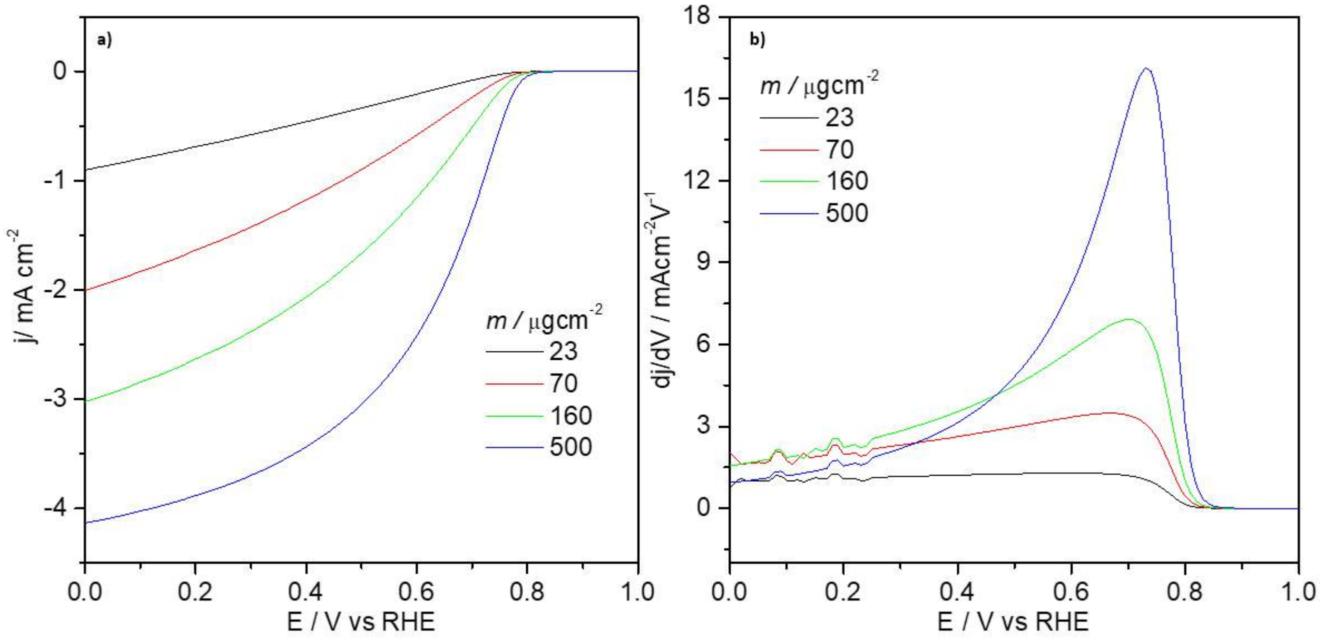

Figure 21 a) Example of simulated voltammograms at different loadings and b) the corresponding simulated derivatives/slopes by Alice Boudet.

Now the question arises: to what extend is this simple theoretical approach able to predict experimental outcomes. Moreover, thin layers are with interest to be used in RRDE, therefore one would want to diminish the ohmic drop in low loadings. Since we are considering the ohmic effect to come from the agglomerate, in principle one would expect less screening effect in agglomerates with smaller volume. Therefore, if one changes experimentally the processing condition of the catalyst to allow for more breakage of agglomerates, a lower screening effect could be predicted, as will be shown in the next section.

3.6 Bm-ink-ORR performance at different loadings

3.6.1 Towards improved catalyst ink dispersion

Further study was conducted for an experimental proof of the model described in the previous section. Another set of experiments was performed with a catalyst ink treated with ball milling (bm-ink) prior to ultrasonication. In MEA studies, ball-milling has been indeed recognized as a successful method to disperse catalytic materials.[168–170] To have a first insight if the dispersion was enhanced with ball milling treatment, SEM cross sections images of both inks drop casted in a gas diffusion layer (GDL) were taken. In Figure 22 one can see a drastic difference on the texture of us-ink vs bm-ink, where the former exhibits a lumpy layer with a thickness of ~20-50 µm with big agglomerates, while the latter exhibits a rather compact film of only ~10 µm. The deposits acquired in the GC disc with the bm-ink are shown in Figure 23, where one can recognize a substantial improvement on the smoothness of the catalyst layer compared to the us-ink deposits in Figure 16, although the electrode coverage at lower loadings is still compromised.

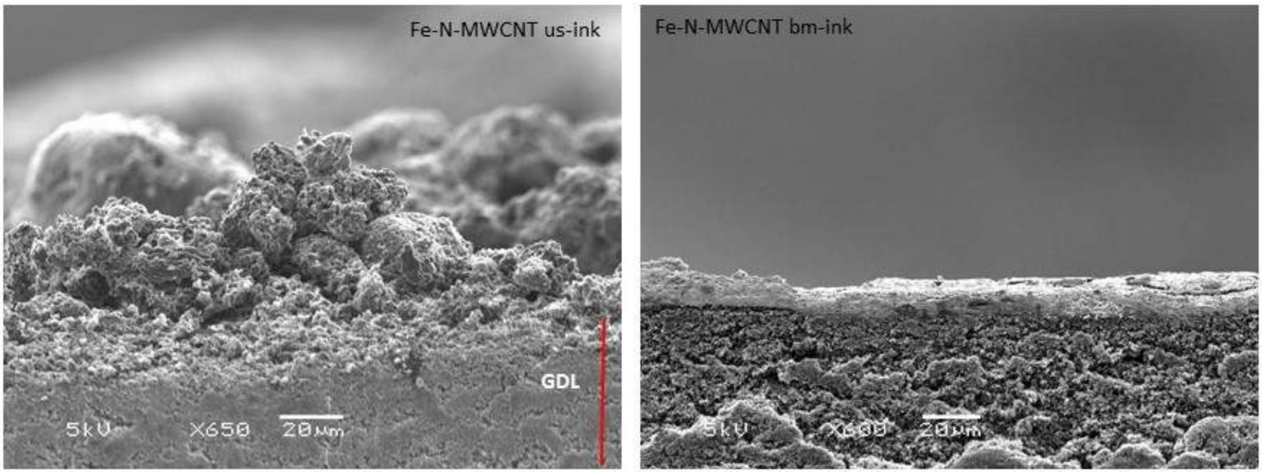

Figure 22 Scanning electron microscopy (SEM) images of us ink and bm ink of Fe-N-MWCNT deposited in gas diffusion layer (GDL) with a loading ~600 ug /cm^2.

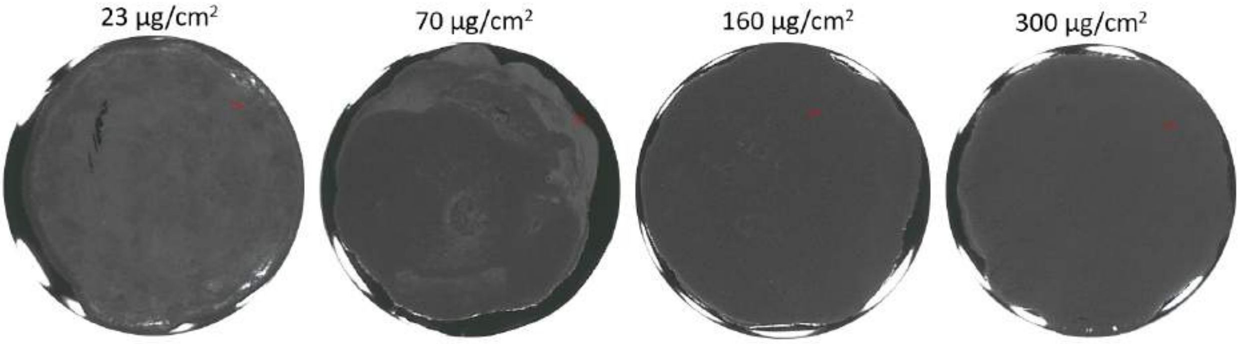

Figure 23 Micrographs of the studied deposits. GC disc covered with different amounts of Fe-N-MWCNT catalyst (bm ink).

3.6.2 Voltammograms and the evolution of their slope

The corresponding voltammograms of the bm ink deposits are presented in Figure 24a with the *j*(E=0V) values higher than the ones observed in the us ink deposits. Herein the diffusion plateau is well defined for higher loadings, therefore we can refer to the current density at 0 V as the limiting current density or j_L. The overpotential values observed herein do not vary much from the us-ink deposits, which may be an indication that the processing conditions does not have an impact on the kinetics of the material and number of active sites. The j_L and E_{onset} results for all loadings are presented in Table 2. The shapes of the LSVs are also evidently more sigmoidal compared to the us-ink as demonstrated in Figure 24b, where the derivative curves are now symmetric gaussian shaped. The derivatives vary from ~13 mA /cm^2·V for the lowest loading to ~30 mA /cm^2·V for the highest. Similar to the us-ink deposits, the sigmoidal shape increases with loading because of the previously described hypothesis, however the values of the slopes here are higher compared to the us-ink deposits. For example, when analyzing the derivatives of the thickest layers in both inks, the bm-ink one exhibits a 30 mA /cm^2·V slope compared to the us-ink one which was only ~14.5 mA /cm^2·V. Therefore, decreasing the size of agglomerates was a successful approach to diminish the screening effect.

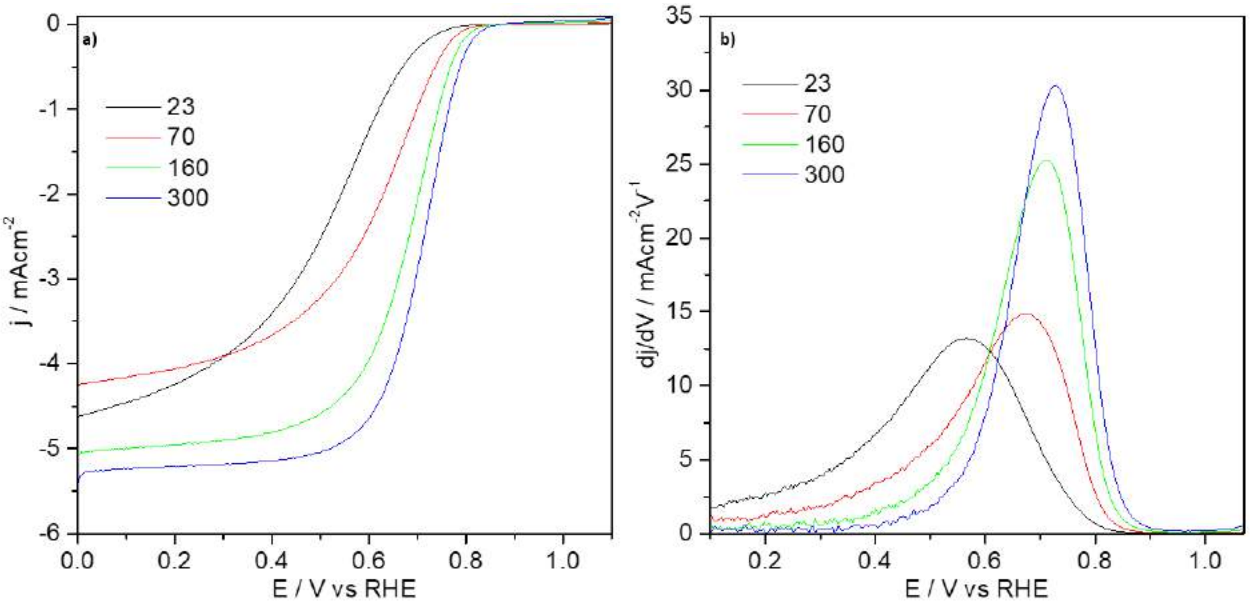

Figure 24 a) ORR LSV curves for bm-ink of Fe-N-MWCNT at different loadings (µg/cm^2) at 1600 rpm, b) the corresponding first derivative of the respective curves. Experiments obtained in O_2 saturated 0.05 M H_2SO_4 at a scan rate of 5 mV/s.

Table 2 j_L and E_{onset} values extracted from Figure 24.

Loading /µg/cm^2	23	70	160	300
j_L / mA /cm^2	-4.62	-4.28	-5.06	-5.42
E_{onset} / V vs RHE	0.74	0.78	0.80	0.83

3.6.3 Selectivity-peroxide production and number transferred electrons

The selectivity of the bm-ink deposits was investigated as well and the %H_2O_2 and *n* at different potentials are depicted in Figure 25. Herein, the percentage of peroxide detected is as low as 3% for the highest loading and ~32% for the lowest loading, while the *n* varies from ~3.42 to 3.95 at ~0.63 V vs RHE. For the highest loadings, the peroxide percentage is for 11% less in the bm-ink and the *n* higher for 0.2 compared to us-ink. For the lowest loadings, the bm-ink exhibits 13% less %H_2O_2 compared to us-ink, and a *n* higher for 0.2. The enhancement of *n* in the bm ink could be due to the reorganization of the agglomerates, with active sites being possibly more homogeneously distributed and H_2O_2 having more neighboring active sites to be further reduced to water. Consequently, the selectivity of the catalyst was generally speaking improved with ball milling treatment of the ink. Notwithstanding, the selectivity of the catalyst is yet varying with the loading for a value of 0.5 in both inks, intercepting the access to the intrinsic ORR selectivity of the material.

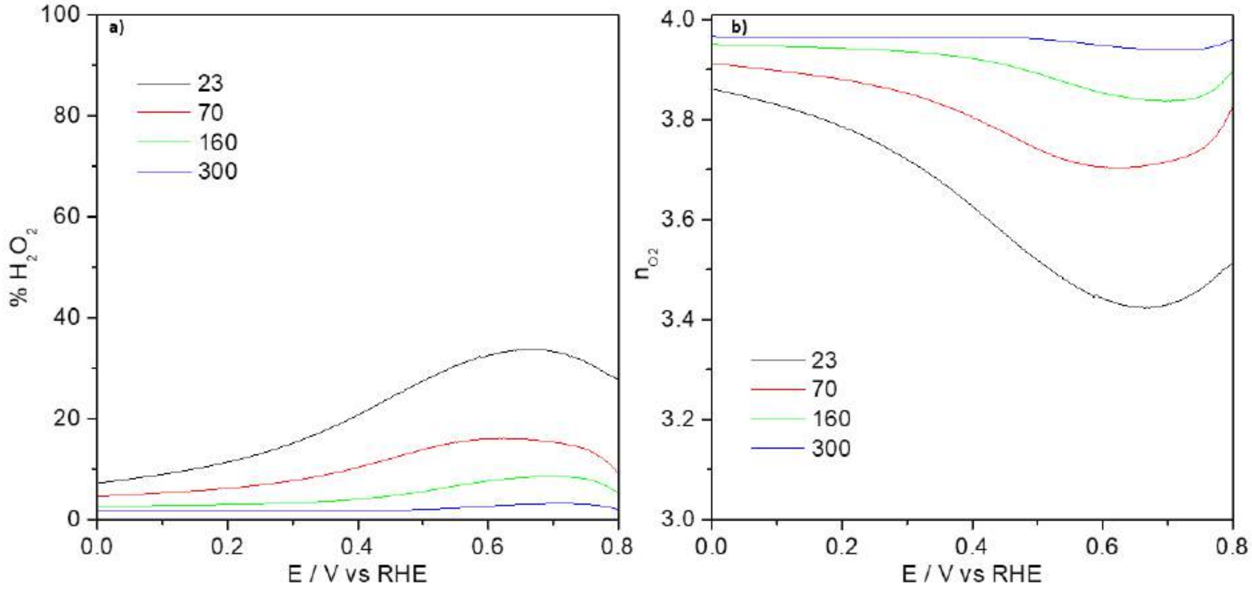

Figure 25 a) Peroxide percentage detected at the Pt ring vs the potential applied at the disc for different loadings (µg/cm^2), b) the corresponding *n* values. Experiments obtained for bm-ink of Fe-N-MWCNT catalyst in O_2 saturated 0.05 M H_2SO_4 at a scan rate of 5 mV/s, corresponding to the measurement at 1600 rpm.

3.7 Conclusion

In this chapter, the Fe-N-MWCNT catalyst was investigated for its selectivity and activity via RRDE method. When the conventional ultrasonicated ink was studied, it was observed that the *n* was varying with loading (from 3.2 to 3.7 at 0.57 V vs RHE), thus prohibiting the information of intrinsic *n*. Meanwhile it was recognized that the shape of LSVs was deviating from the predicted sigmoidal one, all the more at lower electrode loadings. A hypothesis was made assuming that at higher loadings, the local current of agglomerates is more distributed and leads to a diminishing of ohmic drop. The theoretical voltammograms taking into account the screening effect were plotted by Alice Boudet and exhibited the same slope/loading trend as the experimental observation. By improving the catalyst dispersion through ball milling treatment, the hypothesis was further confirmed experimentally. The bm-ink deposits lead to drastically improved slopes of voltammograms, possibly due to less screening effect on the smaller agglomerates. The selectivity was also investigated with RRDE, and changed from ~3.42 to 3.95 (with bm-ink) at 0.6 V vs RHE, depending on the loading.

There are several takeaways from this chapter, starting with the importance of taking micrographs of the studied deposit, ensuring that a good electrode coverage and smooth layer are being obtained. Secondly, the non-sigmoidal shape of the voltammograms can come from an ohmic drop caused by a screening effect inside the catalyst agglomerate. This screening is diminished when the amount of material is increased, as well as when the size of agglomerates is decreased via ball milling. Therefore, processing condition of the catalyst ink plays a role on ohmic losses. In other words, a non-sigmoidal shaped voltammogram suggests that the processing condition needs to be improved (material organization within the CL). This finding is vastly pertinent when considering the integration of the catalyst in FCs, as ohmic drop has huge impact on FC performance and is ought to be kept as low as possible.

Finally, and most importantly, even though the selectivity of the catalyst is enhanced with ball milling treatment, it always changes with catalyst loading no matter the catalyst dispersion. When a good electrode coverage is achieved, the catalyst might be too thick with long H_2O_2 diffusion paths within. On the other hand, lower loadings jeopardize a good electrode coverage even if the dispersion is good, causing lower j_L. Notwithstanding the attempts, using RRDE method it was not possible to be granted access to intrinsic catalyst selectivity which would not depend on the amount of material studied. Ideally, one would need to be in a situation where all active sites are available for the reaction, where no long diffusion paths could trap the intermediate (thin layers) and where one would not depend on the geometric area of a macroelectrode. Theoretically, one could achieve this with a method that allows investigations of much smaller amounts of material and employs smaller electrodes, as will be shown in the next chapter.

Chapter IV: SECM and AFM investigation of ultra-low catalyst loadings

In this chapter, the ORR activity of the Fe-N-MWCNT catalyst is investigated at ultra-low loadings by employing SECM. The aim is to reach a situation where the catalyst thickness will not be a limitation in acquiring the intrinsic number of transferred electrons. Firstly, the meticulous choice of substrate, ultramicroelectrode and deposition method will be introduced, followed by the loading assessment using AFM. Thereafter, the electrochemical measurements acquired with SECM will be presented with a particular emphasis on the number of electrons variation with loading and its association to the agglomerate state of the deposits determined by AFM. Finally, the SECM outcomes were correlated to the results acquired with RRDE in Chapter III for a more comprehensive perspective.

4.1 SECM as a non-conventional ORR investigation method

SECM is in theory a valuable asset when it comes to electrocatalytic investigations due to numerous advantages that microelectrodes can provide, explicated in more detail in Chapter II. Despite the competence of SECM to be employed on its own, curiously in electrocatalysis literature it is vastly used for supporting the RRDE results with extra information, such as activity maps showing the distribution of current in the catalyst deposit.[171,172] SECM was as well used hand in hand with RRDE knowing that both are powerful tools for ORR selectivity assessment via peroxide determination. There are works where the RRDE results were concordant with the SECM ones,[173,174] and works that showed that RRDE rather overestimates activity.[114] The number of electrons assessment via SECM by employing pulsed-profile is the approach most widely used for ORR selectivity assessment,[175,176] although it is not implemented as much as one would expect. Therefore, RRDE still dominates within laboratory scale techniques for ORR activity and selectivity assessment of the catalyst. Additional SECM research in ORR electrocatalysis is vastly requisite for unleashing its power, understanding better the technique and the catalyst itself. In this chapter, the latent potentiality of SECM was utilized by studying ultra-low loadings which were not possible to be acquired in a mm-sized electrode in RRDE.

4.2 Experimental

The rotating disc electrode experimental set-up is regulated in the community, where a commercial GCE is used as WE1 with the drop casted catalyst and the Pt ring around as WE2. Only the dimensions of the GCE and its separation from Pt ring might vary slightly within users. The electrochemical measurements and their treatment to acquire performance parameters are standardized too, although the amount of material studied is not regulated as was mentioned in Chapter III. However, in SECM there is no consensus on the type of substrate (WE1), UME (WE2), catalyst deposition method and neither catalyst amount, leaving some liberty for the experimentalist to customize the set-up judiciously. In the following section, the SECM experimental approach used in this work will be discussed in detail, by reasoning the choice of substrate, deposition method, determination of loading and choice of UME.

4.2.1 Choice of substrate and its fabrication

The substrate is one of the working electrodes in SECM measurements, subjected to polarization at certain potentials during electrochemical measurements. Consequently, a proper substrate selection is mandatory for precise evaluation of catalysts activity. There are several substrate alternatives that could be used in SECM, as long as they fulfil the requirements of being conductive, flat enough for the topography not to influence the electrochemical measurement, and most importantly, inert towards ORR for the substrate activity not to be superimposed with the one of the catalysts. GCE is commonly used in SECM measurements[177] and gold coated Si-wafers have also been employed.[178] The work done previously by Olivier Henrotte in our group demonstrated that boron doped diamond (BDD) is superior to the formerly mentioned substrates as it exhibits the highest overpotential for ORR among them, besides its high stability and reusability.[179] As such, the potential range able to be utilized herein is wider (until -0.3 V vs SCE), without the substrate contributing to the current coming from the catalyst. Considering that the SECM study will be coupled with AFM later on, a substrate with minimal roughness is necessary for the distinguishment of small agglomerates, therefore the conventional BDD with a ~40 nm roughness would not be adequate.[178,179]

Consequently, a flatter BDD substrate was fabricated by Emmanuel Scorsone via the following procedure: Initially diamond nanoparticle (Microdiamant, Switzerland) seeds were deposited onto a silicon substrate according to a procedure described previously,[180] followed by the deposition of a first layer of boron doped diamond of approximately 500 nm thickness in a Seki Diamond AX6500 diamond growth reactor in a hydrogen plasma containing 1% methane as the source of carbon and trimethyl boron as dopant. Subsequently the substrate was transferred to another Seki Diamond AX6500 diamond growth reactor, where a 100 µm thick layer of intrinsic diamond was overgrown onto the BDD layer. Finally, the silicon was removed by wet etching in a mixture of HF/HNO_3 in order to acquire a free-standing diamond film. While the rough surface is the one exposed to the plasma during growth, the smooth surface (boron-doped) is the one originally in contact with the silicon. Since the latter is smooth in the first place, this BDD layer will end up smooth too (Figure 26). The substrate was scanned with AFM (image in Figure 27a) where the root mean square (RMS) roughness of only 0.281 nm for a 2 µm area was determined. Some small spots appear brighter in the AFM image, however if we see the section analysis of such region in Figure 27b (marked with a black line in Figure 27a), one can see that even such irregularity exhibits a roughness of less than 3 nm.

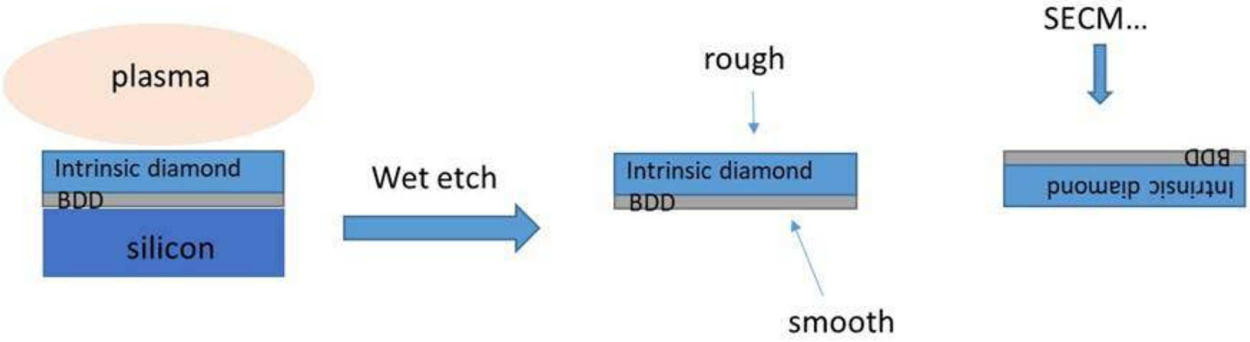

Figure 26 Scheme showing the fabrication process of BDD.

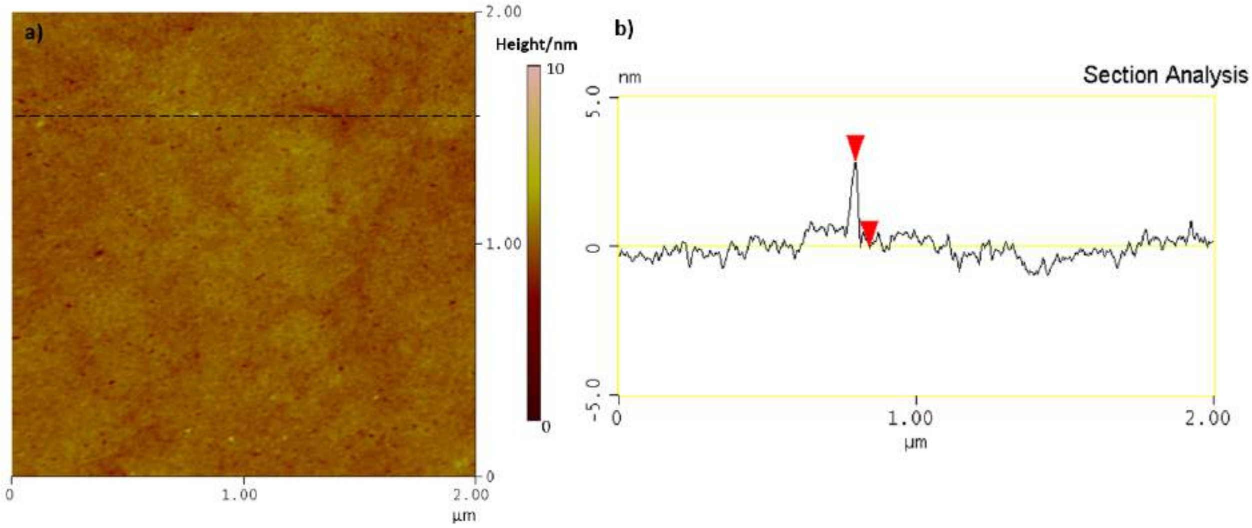

Figure 27 a) AFM image of the flat BDD substrate, b) section analysis of the region marked with a black line in the image, depicting the roughness of the white spots in the image.

4.2.2 Catalyst ink preparation

From the study presented in Chapter III, it was evident that ball milling was successful in breaking big agglomerates and well dispersing the catalyst. Therefore, the catalyst ink herein was prepared by dispersing 20 mg of catalyst powder into a 1.175 mL mixture of isopropanol and water (3:1 ratio) and 24 µL Nafion (5% in weight after drying), leading to a concentration of 17 mg/mL. The Nafion percentage in this formulation is about 5 %. Subsequently, after adding ~15 g of Zirconium beads, the ink was treated 40 minutes on an IKA ULTRA-TURRAX® Tube Drive for an initial breaking of agglomerates, followed by ball milling for 2 weeks in an IKA ROLLER 6 shaker. Thereafter, the ink was diluted to ~0.2 g/L and has undergone ultrasonic bath treatment for at least 30 minutes prior to depositing it on the substrate.

4.2.3 Deposition of the catalyst ink onto the substrate

The most straight-forward way to deposit the catalyst onto the substrate would be drop casting, which is indeed the common practice.[115] However, in such cases it is difficult to obtain a homogeneously distributed deposit and to control its size. Consequently, in this work and in accordance with previous studies from the group, the deposits were acquired by spray-coating (Sonotek, ExactaCoat apparatus) the diluted ink, 5 mm on top of a micropatterned mask (from Micron Laser Technology) with a size of 200 µm, under which the BDD substrate is fixed. Homemade sliding plates are placed on top of the mask in order to allow the access of the ink only at one micropattern at a time (Figure 28a). The amount of ink sprayed is controlled by the number of passages in the nozzle which is chosen manually in the Sonotek Software, where four passages spray 0.15 mL of ink. The trajectory of four passages for each deposit is determined in the software, where each passage starts from different corners and they overlap with each other, leading to homogeneous and small deposits (Figure 28b). A flow rate of 0.3 mL/s has been chosen as the best compromise in order to avoid flooding and to allow the ink to reach the substrate through the mask. The substrate with the mask is placed on top of a heating plate (ExactaCoat apparatus) for allowing high temperatures (~80^{o}C) that aids on solvent evaporation during the deposition (Figure 28c). Few-seconds pauses are also employed after each passage in order to avoid flooding. The deposits were dried under argon flux afterwards, in order to remove the poorly adhered particles. Finally, micrographs of the deposits are taken with Olympus BX61 optical microscope prior to SECM measurements, in order to determine their area and homogeneity.

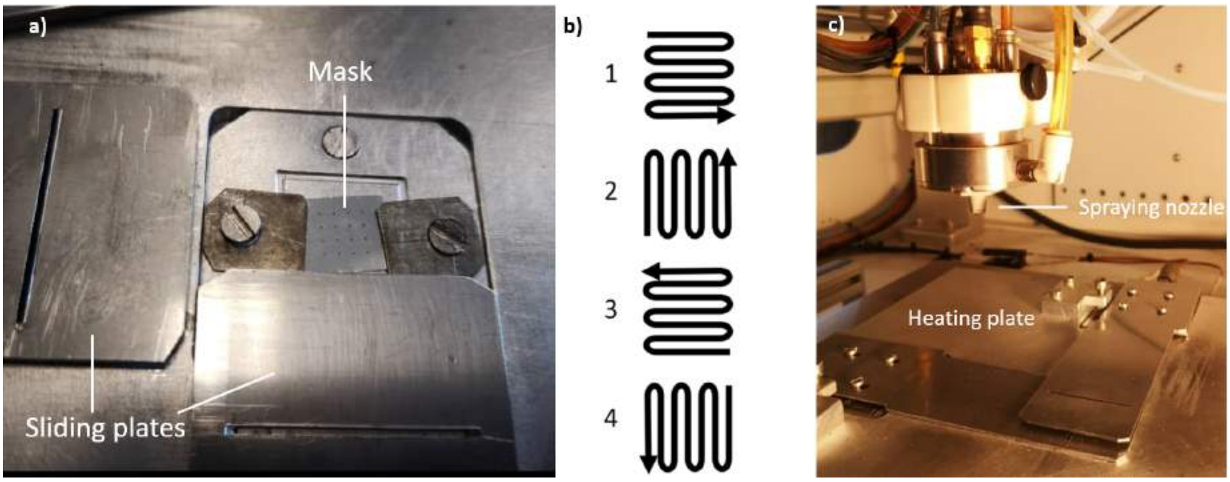

Figure 28 a) Picture of the mask fixed on top of the substrate with the sliding plates, b) passage pathways of the spraying nozzle above the sliding plates, c) picture of the set-up prior to spraying.

4.2.4 Loading estimation via AFM

Theoretically, the loading could be estimated by the volume of sprayed ink on the substrate and the area defined by the mask which are known in our case. However, the work done previously by Alice Boudet in our laboratory showed that using the exact same apparatus, in reality a very low amount of sprayed catalyst actually adheres to the substrate (5-25%) and this adherence even depends on the material.[178] The size of deposits observed by optical microscopy is usually somewhat bigger than the size of the mask used (200µm), indicating the spreading of the ink underneath the mask.[178] Therefore, this generates the need to have a more accurate and quantitative estimation of the loading, which can be achieved by catalyst volume determination with AFM (PicoLE microscope from Molecular Imaging) which herein was employed with a protocol established by Alice Boudet.[167] The resolution deemed appropriate for the experiments herein is 510 x 510, where the size of one pixel is 98 nm and the size of the scan is 50 µm. Five images were taken in different locations of the deposit with a low scan speed of 0.5 line/s. If the extrapolated catalyst volume calculated in these images did not differ more than 10% from each other, the number of images taken was considered adequate for a fair estimation of the total deposit volume. Gwyddion software was used for image processing, where the particles are discerned via a watershed algorithm[181] which establishes the local extremes and separate grains (Figure 29b). The export of the following parameters is done afterwards: particle height, volume, projected area and external surface. The definition of 50 ranges of particle volume was done, distributed in a logarithmic scale within the tiniest and the biggest particle detected during experiment. A python routine was used to count of particles in each range and the sum of their volumes.[167] The average volume of all five images within one deposit is then multiplied by the ratio between the deposit surface and the AFM-determined surface. Consequently, we have information about how the volume of catalyst in each range contributes to the total catalyst volume (Figure 29c). The loading of the deposit was calculated using the volume acquired by AFM, the area determined by the optical microscope, and the assumed density of non-porous carbon 2 g/cm^3 via Equation 12.[182] This assumed density could be higher than the real density of the material studied herein which might be porous to some extent, leading to a small overestimation of the loading. Nevertheless, this is not an obstacle when considering that the main intention of this work is rather the comparison of different loadings. The loadings investigated in this work were 1.2 µg/cm^2, 5.7 µg/cm^2, 13.8 µg/cm^2 and 38.4 µg/cm^2. Smaller loadings were unsuitable for investigation because they were not visible in the substrate, therefore making it difficult to find during the SECM experiment. The micrographs along with the corresponding AFM images of all deposits are shown in Figure 30, where the distribution of the catalyst appears fairly homogeneous and consistent between AFM and optical images.

$$Loading\ = \frac{2\ gcm^{-3} * V_{AFM}(cm^3)}{A_{micrographs}\,(cm^2)} \qquad 12$$

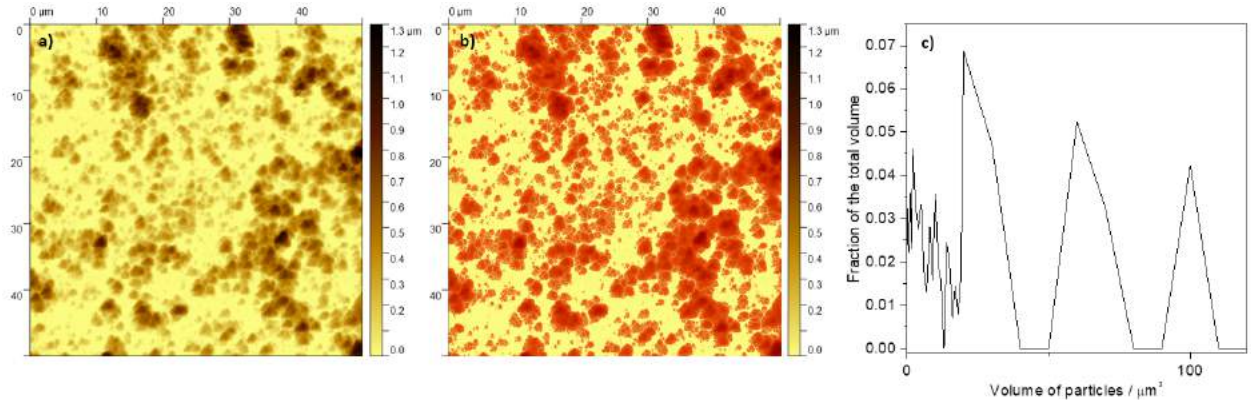

Figure 29 Demonstration of the protocol for particle size determination. a) initial raw AFM image, b) distinguishment of particles via the watershed algorithm embedded in Gwyddion software, c) final result showing the volume of particles in µm³ (x axis) and how much they contribute to the total volume of the deposit (y axis).

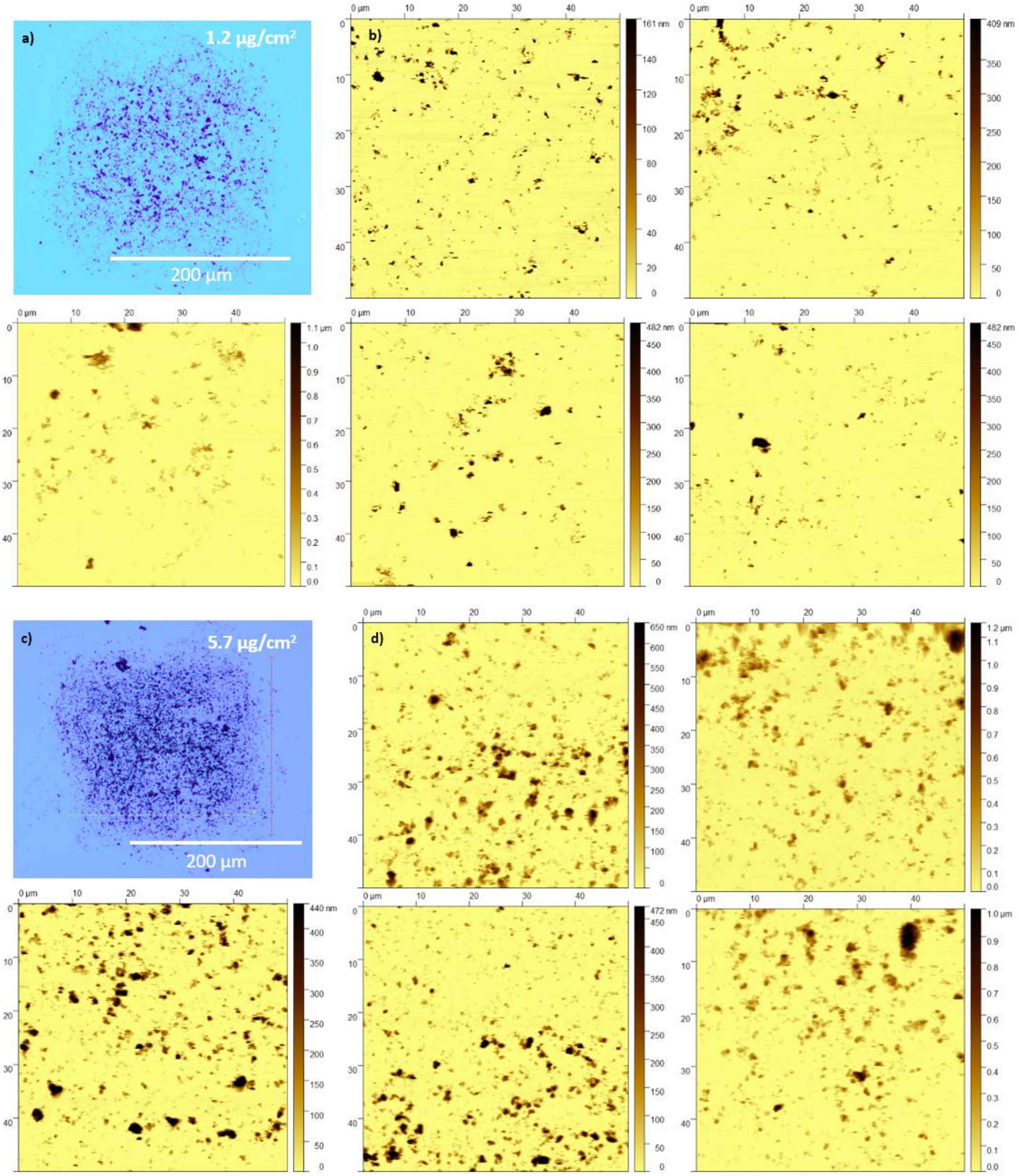
a)
1.2 µg/cm^2
200 µm
b)
161 nm
409 nm
1.1 µm
482 nm
482 nm
c)
5.7 µg/cm^2
200 µm
d)
650 nm
1.2 µm
440 nm
472 nm
1.0 µm
0 µm
10
20
30
40

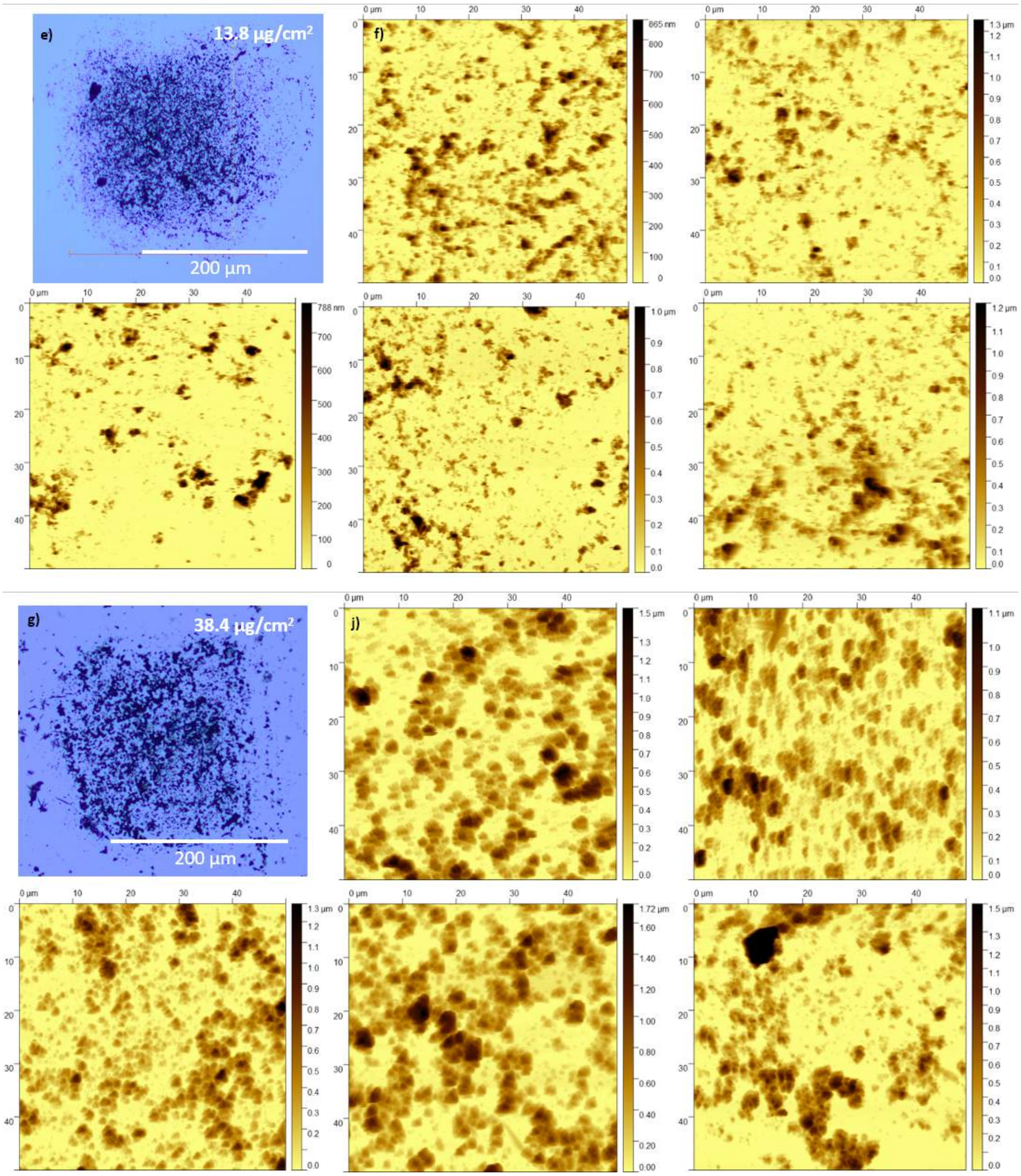

Figure 30 a,b) Micrograph and AFM images of 1.2 µg/cm² deposit, b,c) micrograph and AFM images of 5.7 µg/cm² deposit, e,f) micrograph and AFM images of 13.8 µg/cm² deposit, g,j) micrograph and AFM images of 38.4 µg/cm² deposits.

4.2.5 SECM electrochemical approach

The common UME material of choice for ORR investigation is platinum[177] due to its high activity towards ORR, while the experiments are usually carried out in RC mode as a valuable protocol for ORR studies, considering that it excludes background currents often encountered in TG/SC mode.[106,177] In order to get access to selectivity of the catalyst, the detection of peroxide produced during ORR is also needed and this is usually done with Pt microelectrodes too. The unique protocol reported on literature regarding selectivity investigation of the catalyst is via pulsed profile method developed in Schuhmann's group in 2007[183] where a combination of RC and SG/TC mode is employed in the same experiment for ORR and H_2O_2 current evaluation with a Pt UME. Herein, while the substrate was polarized at -400 mV and 0 mV vs Ag/AgCl, a potential pulse profile was applied to the tip as follows: +0.05 V for 500 ms as initial inert potential, +1.2 V for 200 ms for generating oxygen, -0.6 V for 500 ms for oxygen reduction (RC mode), +1.2 V oxygen generation, and finally +0.6 V for 500 ms for peroxide oxidation and data acquisition (SG/TC mode).[115] The timeframes of milliseconds were chosen in order to avoid the escape of oxygen and peroxide before the track of faradaic currents.

However, in a previous work done in our group as a part of the PhD thesis of Olivier Henrotte, by performing CAs at different cathodic potentials in a Pt UME it has been shown that the current did not reach a stable value until ~300s.[179] This was unanticipated considering that the applied potentials corresponded to the ORR diffusion plateau, which should lead to steady state currents. This observation was linked to the establishment of Pt surface sites and possible contamination of the tip.[179] Nevertheless, acquiring performance parameters based on steady-state currents is crucial in order to exclude the possibility of the current corresponding to adsorbed electroactive species or charging current.[90] On that account, by Henrotte et al.[179] it was demonstrated how Au probes are an excellent alternative to Pt for ORR investigation due to higher sensitivity towards O_2 detection and higher stability which allows the performance of steady state measurements.[179] For H_2O_2 detection however, Pt UME remains the best alternative as with an Au UME one cannot observe conclusive peroxide oxidation peaks.

Consequently, the SECM experiments herein were originally performed with a new approach via two UMEs *subsequently*, namely an Au UME for ORR detection in RC mode and a Pt UME for H_2O_2 oxidation in SG/TC mode. A SCE electrode was used as RE and a Pt mesh separated from the electrolyte by glassware was used as CE. The UMEs were purchased by Sensolytics, both with a 10 µm diameter, RG=10 and r_T=5 µm. Contrary to the pulsed profile used by Schuhmann´s group where the oxygen is provided via a potential pulse at the electrode, inhere prior to the start of each experiment, the electrolyte (0.05 M H_2SO_4) was purged with oxygen for at least 15 minutes, and then the O_2 flow was kept on top of the electrolyte while avoiding bubbles. Before starting the electrochemical measurements, the tip was placed above the center of the deposit, which was achieved by doing line scans in RC mode and recording the coordinates when the current reached the maximum value (center of deposit). During the measurements, the Au tip was kept static above the deposit and polarized at -0.65 V vs SCE for oxygen reduction, while the substrate was swept at potentials from 0.4 V to -0.3 V vs SCE at a scan speed of only 2 mV/s in order to achieve steady state conditions. Subsequently, for peroxide detection the substrate potential was swept at the same potential range as for ORR, while at the Pt UME a CA was recorded at 1.1 V vs SCE for H_2O_2 oxidation. The static-tip approach was previously used by Sánchez-Sánchez et al[184] and saves a significant amount of time compared to performing line scans at different substrate potentials, which would have to be conducted with a maximum scan rate of 10 µm/s for the current response not to be perturbed by motion.[185] Nevertheless, the tip currents acquired from both measurements are plotted versus the potential applied at the substrate, which was converted from SCE to RHE via Equation 11. The tip currents acquired by both experiments were used to calculate the *n* using Equation 10. The collection efficiency (N) in commonly taken as 100% as long as the probe current does not vary with a change in *d*[114,115] as it was found in our case. However, considering that two different electrodes are employed herein which may have slight dimension variations, numerical simulations are necessary to be performed. This was done by Alice Boudet as a part of her doctoral thesis, in which case the collection efficiency of both tips, Pt in SG/TC mode and Au in RC mode were taken into account ($N=\eta_{RC}/\eta_{SG/TC}$).[167] This is due to the fact that with this SECM approach, both ORR and H_2O_2 currents are collected *indirectly* at the UMEs, whereas in RRDE for example the ORR current is acquired directly at the disc where the catalyst is deposited, thus only the collection efficiency of the Pt ring needs to be evaluated. Nevertheless, the collection efficiency for both tips, at the same experimental parameters as used in this thesis (*d*, RG, r_T) was N=$\frac{4.3\%}{3.7\%} = 100\%$.

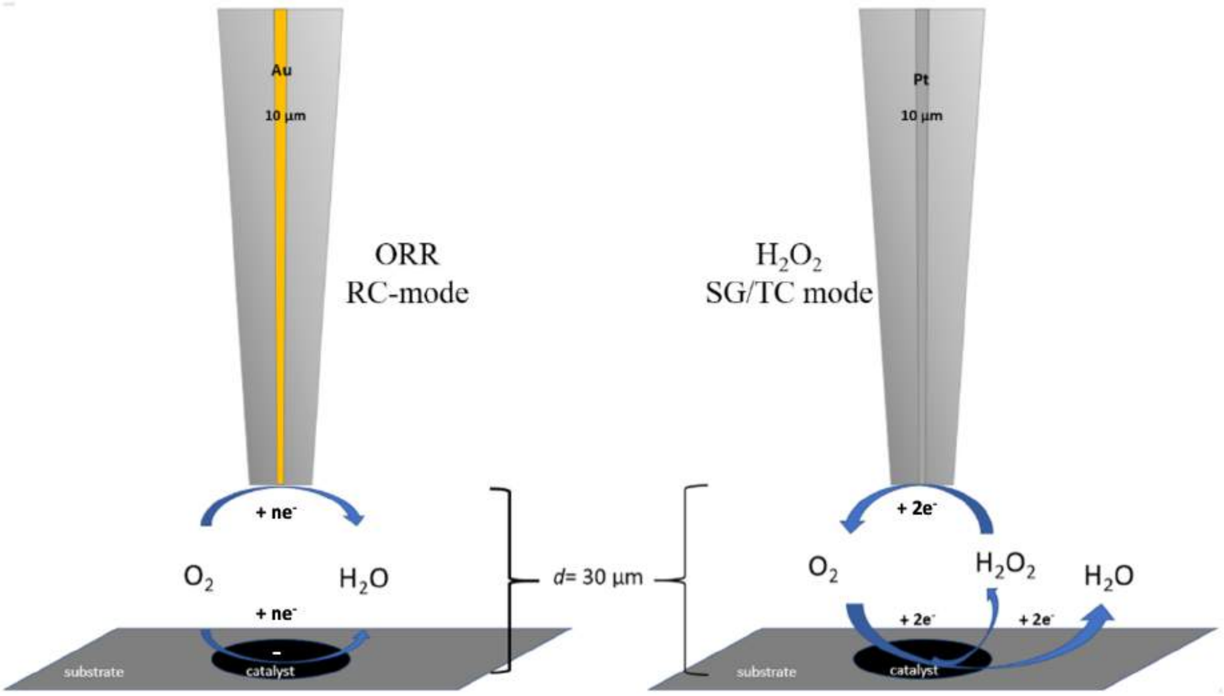

Figure 31 Scheme of the dual electrode SECM approach used.

4.3 ORR performance evaluation and interpretation

4.3.1 ORR activity and selectivity evaluation at different loadings

ORR was evaluated using RC mode where the Au probe is polarized at an oxygen reducing potential, while the sample is simultaneously swept in a wider range of potential (0.7-0 V vs RHE). If we normalize the probe current by its value at the most positive potentials where no ORR occurs, we obtain a depiction of ORR catalytic activity versus applied potential as shown in Figure 32a. During the measurement in RC mode, at more cathodic potentials both the substrate and the Au tip are competing for ORR, which leads to diminished current at the tip as the potential becomes more negative. The more the current depletes, the higher the activity of the catalyst towards ORR. In Figure 32a, it is evident that at higher catalyst loadings, there is more oxygen being consumed by the catalyst and the ORR net current is elevated. It is interesting to observe that the curve corresponding to the highest loading (38.4 µg/cm^2) seems to be the only one where diffusion starts to be a limitation around 0.3 V vs RHE. With a higher amount of material (more active sites), the ORR is occurring rapidly and causing an oxygen depletion in the vicinity of the substrate and the tip, leading to a current pseudo-plateau. Nevertheless, to better quantify the electrochemical performance, the onset potential was determined for all loadings. It is defined as the potential at which the probe current reaches 0.9 (marked in Figure 32a), and the more positive its value (the lower overpotential), the more active the material.[178] In Figure 32b, one can see that the overpotential becomes more positive with loading and follows a trend for the three lowest loadings. The highest loading however (38.4 µg/cm^2) deviates from the line. These kind of deviation was observed as well previously from our group[178] and was related to the agglomerate size, which will be discussed in section 4.3.2.

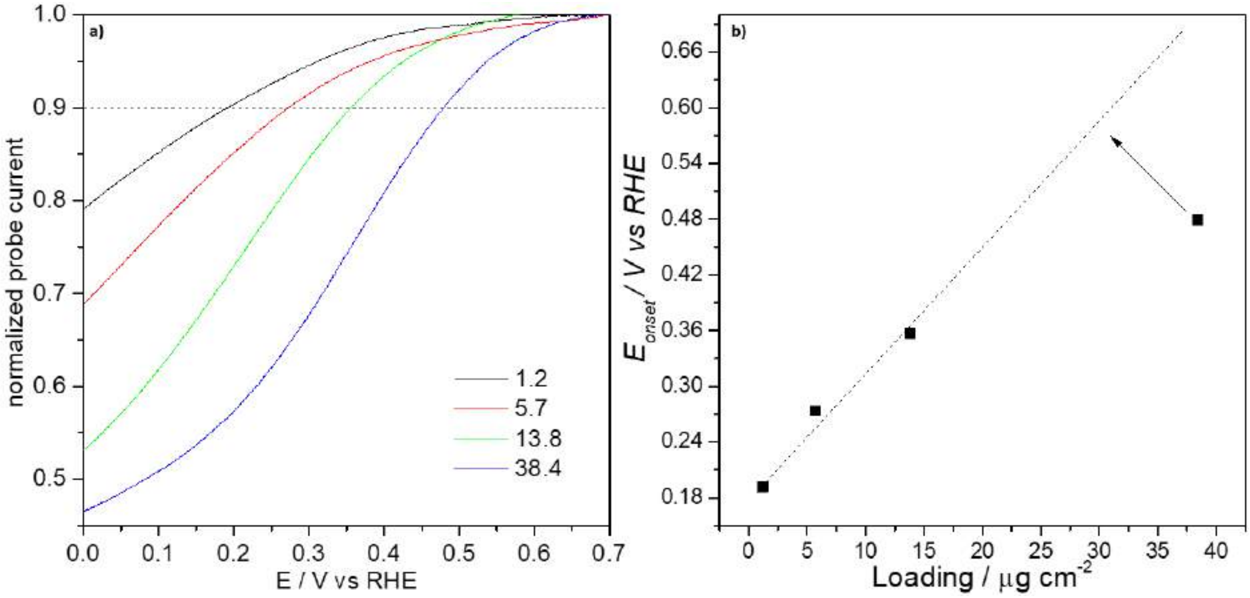

Figure 32 a) normalized probe current versus applied potential at the sample, b) overpotential values at a probe current of 0.9. Results correspond to all studied loadings in µg/cm^2. Electrolyte used was 0.05 M H_2SO_4 saturated with O_2.

In order to acquire the selectivity or number of transferred electrons, the determination of peroxide produced during ORR is necessary. This was done in SG/TC mode while polarizing the probe at 1.4 V vs RHE while the substrate is simultaneously swept in a range of 0-0.7 V vs RHE. During the SG/TC mode the amount of H_2O_2 detected increases at more cathodic potentials due to a higher rate of oxygen reduction at the catalyst, leading to higher current at the Pt tip (Figure 33a). Inhere, the current trend is opposite to the ORR one, with less peroxide detected for highest loadings (0.15 nA) and larger H_2O_2 currents detected for the lowest loading (1.25 nA). Using the ORR and H_2O_2 background-corrected currents, the *n* was acquired for all loadings as shown in Figure 33b. As predicted by the trend of H_2O_2 currents, the number of electrons increased with loading. At 0 V vs RHE the most loaded deposit (38.4 µg/cm^2) exhibits a *n*~3.9, followed by 13.8 µg/cm^2 with *n*=3.8, 5.7 µg/cm^2 deposit with *n*~3.3 and finally, the 1.2 µg/cm^2 deposit exhibits a *n* of only 2.6. All curves seem to exhibit a *n* roughly independent of potential in a wide range (0 to ~0.5 V vs RHE), with the exception of the 5.7 µg/cm^2 deposit which has a less steady behaviour. Further interpretation of results was done by analysing the deposits in agglomerate scale with AFM, as will be shown in the next section.

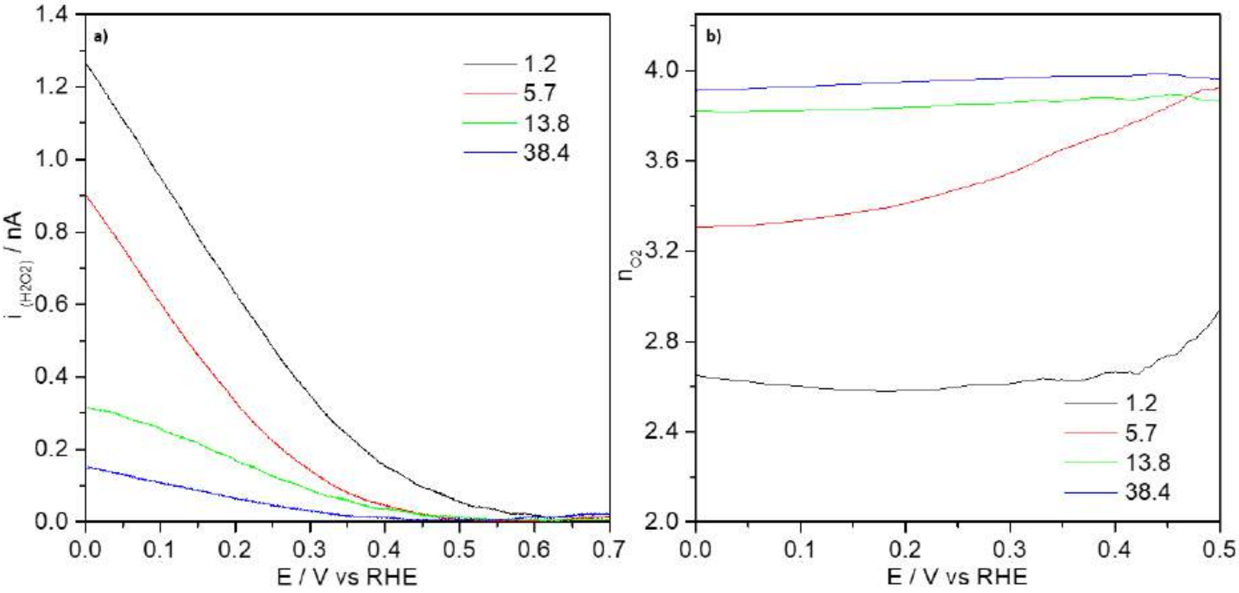

Figure 33 a) net background corrected H_2O_2 currents acquired with a 10 µm Pt UME in SG/TC mode, b) number of transferred electrons calculated from the ORR and H_2O_2 currents while considering *N*=100%. Results correspond to all studied loadings in µg/cm^2. Electrolyte used was 0.05 M H_2SO_4 saturated with O_2.

4.3.2 Linking the ORR activity to the deposit agglomerates

AFM images were taken for each deposit and were processed via Gwyddion software and a Python routine in order to get information on the agglomerate size and their contribution to the total volume of the catalyst. As shown in Figure 34a, there is a great difference on the agglomerate sizes between deposits. The 38.4 $\mu g/cm^2$ deposit contains particles in a range of 20-40 μm^3 corresponding to 7% of the total volume, particles of 70-80 μm^3 corresponding to 5% of the total volume and 90-110 μm^3 to 4%, besides the smaller ones from 0 to 20 μm^3 which seem to have less contribution to the total volume (~3%). It is followed by the 13.8 $\mu g/cm^2$ deposit with particle volumes of 19-30 μm^3 corresponding to 3% of the total volume and 0-11 μm^3 particles. The 5.7 $\mu g/cm^2$ deposit has particles up to 14 μm^3 and the lowest loaded deposit has particles with a volume up to 3 μm^3. There is a clear trend on the increase of agglomerate size with loading which was rather qualitatively evident as well from AFM images in Figure 30. This is possibly a consequence of material accumulation at the substrate as the ink evaporates during the spraying process.

Firstly, the 38.4 $\mu g/cm^2$ deposit is dominated by agglomerates at least double the size of its peers. This could mean that many active sites that are located in the interior part of the bulky agglomerate might not be easily accessible to the reaction.[178] This might be the explanation for the smaller than predicted overpotential for this deposit, observed in Figure 32b. When relating to the peroxide results in Figure 33, one can realize a correlation between agglomerate size and the amount of peroxide detected, thus number of transferred electrons too. There is a chance that at bigger agglomerates, the diffusion pathway of the intermediate is longer and may possibly lead to peroxide decomposition before getting released in the solution. This way, there could be less peroxide detected at the Pt UME leading to an apparent higher number of transferred electrons. At small agglomerates in the lowest loadings, a volume of only ~3 μm^3 might be already small enough for the intermediate that is produced within to get released easily onto the electrolyte, and thus get detected by the electrode. This trend is in accordance with what was observed before in a SECM loading/activity study[114] as well as with the RRDE results presented in Chapter III. A similar reasoning was made when interpreting the RRDE results where the thickness of the layer was discussed instead. A perspective on the ORR activity acquired by RRDE and SECM is presented in Section 4.3.4.

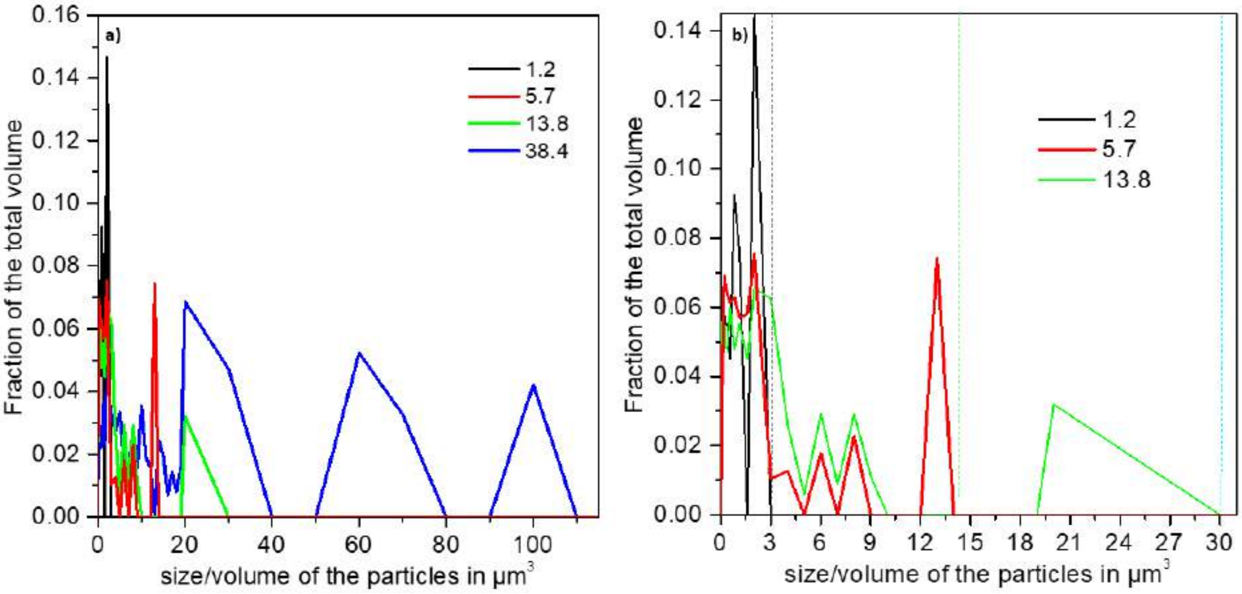

Figure 34 Particle sizes and their distribution determined by AFM for all loadings in µg/cm².

4.3.3 Influence of Nafion on the detected H_2O_2

The catalyst studied herein is modified with Fe, which can undergo demetallation in free water and form ferrous ions Fe^{2+}.[186] The latter can react with the H_2O_2 produced during ORR within the layer via the well-known Fenton reaction and form highly active radicals such as OH* (Equation 13).[39,187] These radicals can attack and degrade Nafion in various functional groups as shown in Figure 35.[188] Moreover, it has been shown that the H_2O_2 alone has the power to degrade Nafion too.[187] Considering that at higher loadings there is more Nafion content on the deposits, one cannot exclude the possibility of the peroxide to be involved in such side reactions to a higher extent, leading to less amount being released from the surface of catalyst.

$$H_2O_2 + Fe^{2+} \rightarrow OH^{\cdot} + OH^{-} + Fe^{3+} \qquad 13$$

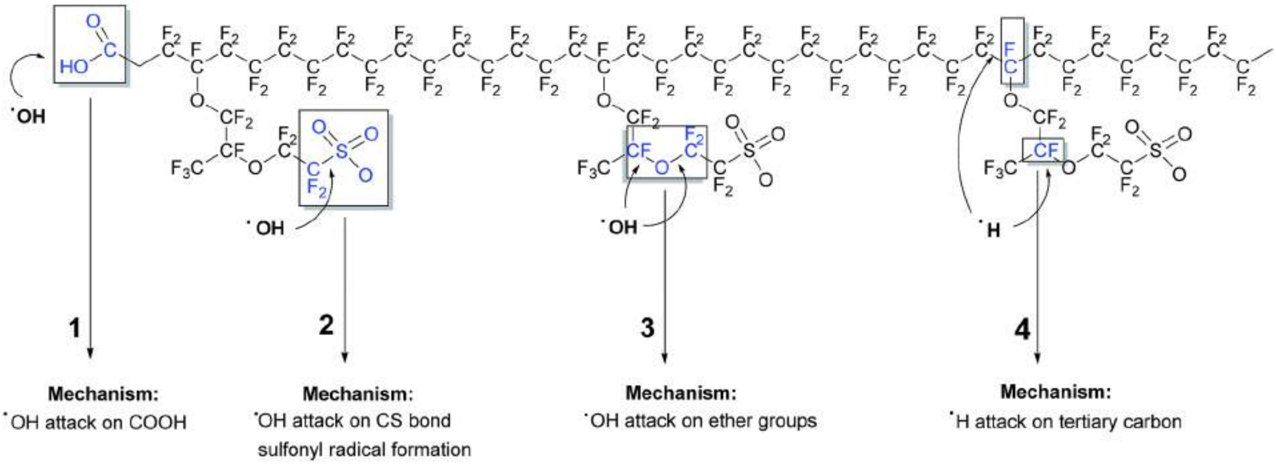

Figure 35 Possible mechanisms of OH* radical attack at different functional groups of Nafion structure.[188]

In order to further look into this, a deposit with similar loading (5.6 µg/cm^2) as presented before (5.7 µg/cm^2) was acquired, only this time with three times more Nafion content (15%). Note that identical loadings were not possible to be acquired due to the limitation in the reproducibility of the Sonotek spraying machine. The micrographs and AFM images of the deposit with 15% Nafion are presented in Figure 36. The ORR and peroxide detected is plotted in Figure 37 along with the previously studied loadings with 5% Nafion, namely the 5.7 µg/cm^2 deposit. While the ORR normalized currents do not differ significantly within the 5% and 15% Nafion deposits, on the other hand it can be observed that the deposit with more Nafion content leads to less peroxide detected at the probe. The current for the 5.6 µg/cm^2 deposit is lower for a value of 0.4 nA compared to its analogue. However, when we observe the agglomerate size in Figure 37c, one can see that the particle volume ranges are 5-8 µm^3, which is not very different from the agglomerates studied previously with 5% Nafion and with particle sizes of 3-14 µm^3. In fact, despite the fact that in the 15% Nafion deposit most agglomerates seem to be small (up to 1 µm^3), the peroxide produced was minimal. Therefore, higher amount of Nafion seems to be playing a role in the peroxide detected, therefore in the *n* too. Indeed, the importance of optimizing the Nafion-to-catalyst mass ratio has been also emphasized in earlier works.[189]

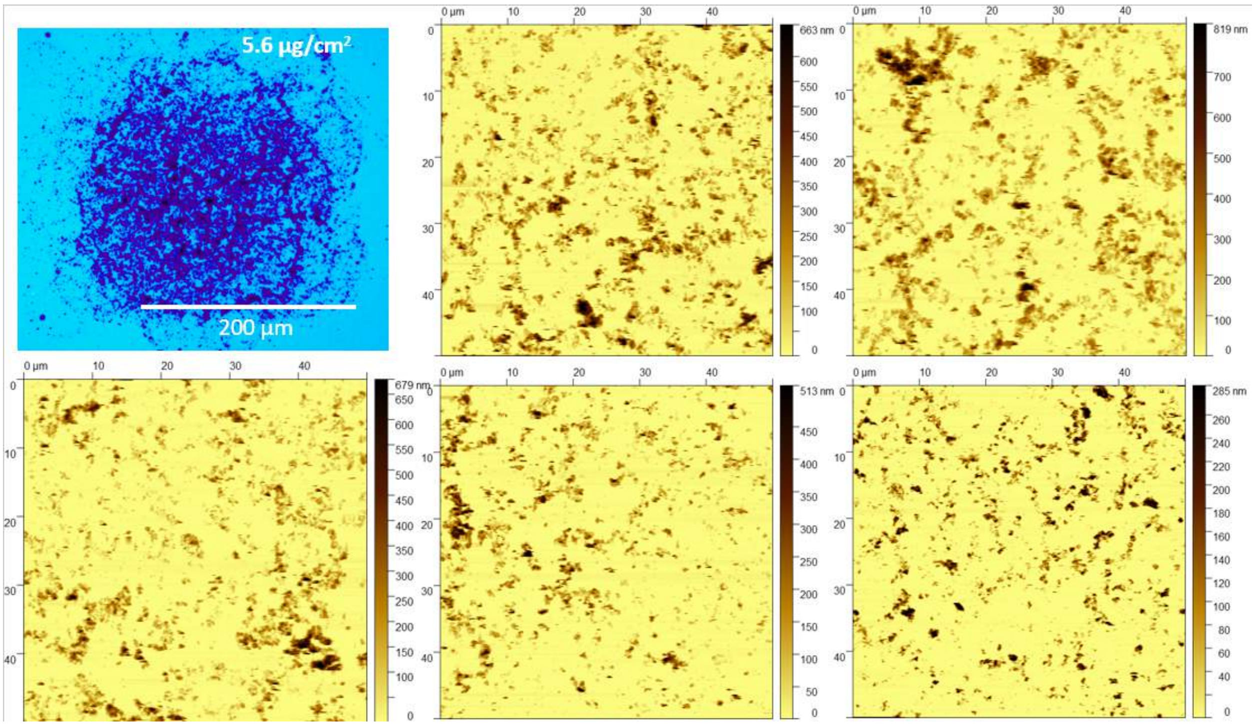

Figure 36 Micrograph and AFM images of 5.6 µg/cm² deposit with 15 % Nafion.

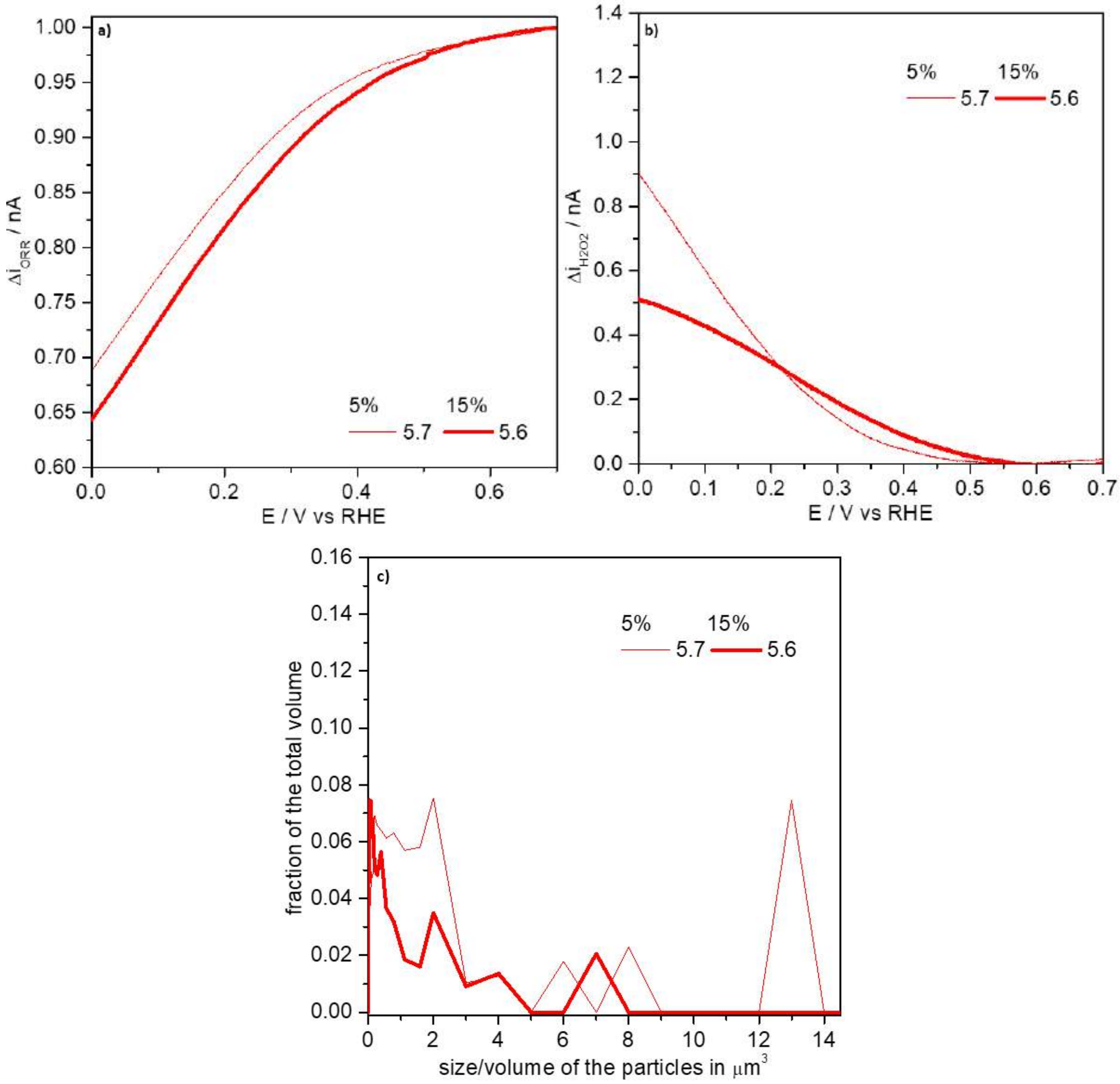

Figure 37a) ORR currents for the deposits with 15% Nafion content and the previously studied deposits with 5% Nafion b) peroxide detected by the Pt UME for the same deposits c) particle sizes and their distribution determined by AFM for the corresponding deposits. Loadings are presented in µg/cm^2.

4.3.4 Comparison of results acquired with SECM vs RRDE

There was comparable information acquired with different methodologies. While the overpotential was decreasing with loading in both SECM and RRDE investigations, the differences in the selectivity of the catalyst towards ORR are interesting to compare. To have a better understanding of the results, a plot of the *n* acquired at different loadings for the RRDE and SECM measurements is presented in Figure 38. One can see that with SECM, the limit of loading able to be studied was expanded. The lowest *n* acquired with SECM is ~2.6 at a loading of only 1.2 μg/cm^2, while in RRDE the lowest loading (23 μg/cm^2) exhibits a *n*~3.2. A common *n* of 3.9 was acquired with both methodologies at their highest studied loadings, namely 38.4 μg/cm^2 with SECM and 300 μg/cm^2 with bm ink in RRDE. At a similar loading where both methods could be used, we can see that the *n* acquired with SECM is higher than the one acquired with RRDE. This can be explained by the difference in the material organisation in the spots investigated by the two methods. For SECM investigation we have sprayed the ink, leading to more individualized agglomerates than for the RRDE study, where the ink was drop casted. Another observation in these plots is the similarity on the trend of their *n* change with loading. As the amount of material increases, the *n* increases no matter the methodology used. Low loadings able to be acquired with SECM were foreseen not to have limitations of peroxide blockage. However, as it was seen also with AFM, even within such low loadings there is considerable differences in agglomerate sizes, despite the prudent deposition methodology used. Nevertheless, limitations that prohibit a *n* independent of loading seem to be manifesting in micro-scale SECM measurements too.

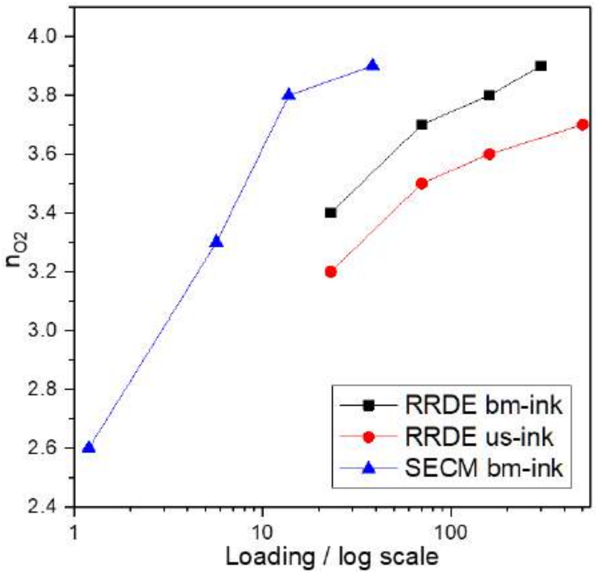

Figure 38 A representation of number of electrons acquired from RRDE measurements (for bm and us ink) and from SECM measurements of bm ink.

4.4 Conclusion

In this chapter, the ORR activity and the agglomerate scale of the Fe-N-MWCNT catalyst was studied with SECM and AFM respectively. The catalyst deposits were acquired by using a spraying technique which lead to defined and homogeneous spots whose area was determined with an optical microscope. The loading of all the deposits was acquired unambiguously by doing AFM scans prior to SECM measurement and extracting the information of size and height of particles, thus granting the total volume of the catalyst.

The electrochemical SECM measurements were carried out by using an Au UME for oxygen detection, as deemed a successful approach in previously reported works. In addition, peroxide produced by the catalyst during ORR was detected by the Pt UME, thus enabling the acquirement of ORR selectivity. While in RRDE measurements, the lowest number of electrons observed was 3.2, in SECCM at a loading of 1.2 µg/cm^2 a *n* of only 2.6 was acquired. Therefore, there is more peroxide produced at the sample that one might have thought solely from the RRDE measurements where this information could have been hidden if one would focus on the highest loadings. In other words, the intrinsic selectivity of this catalyst is closer to 2, rather than 4. This outcome is very significant when considering the integration of the catalyst into a fuel cell, as a high amount of peroxide leads to catalyst degradation. However, even though with SECM at low loadings it was foreseen that there would be no limitation in catalyst thickness, the *n* still kept varying with loading. With AFM we elucidated the sizes of agglomerates in all deposits and observed a correlation between big agglomerate size and smaller H_2O_2 currents (therefore higher *n*). It appears that even agglomerates with a volume of 25 μm^3 could be too big and lead to peroxide entrapment within. On the other hand, more Nafion content in higher loadings could also play a role on the peroxide detected by the UME, due to side reactions that occur between peroxide or its radicals and Nafion. Ultimately, the agglomerate size plays a role on the released peroxide.

Nevertheless, the ability to study ultra-low loadings is valuable in SECM as we can get closer to the intrinsic number of transferred electrons. These results also suggest that in future works, it is critical that the catalyst deposit is more rigorously homogeneous with small agglomerates and optimum Nafion-to-catalyst ratio, so that the entrapment of peroxide within the layer or its reactions with the binder could be avoided and one could get access to the core number of transferred electrons.

Chapter V: SECCM and SEM analysis of individual catalyst agglomerates with nanoscale resolution

In this chapter, nano-scale SECCM is employed to investigate individual Fe-N-MWCNT catalyst agglomerates. At such small scales, the irrelevance of catalyst thickness opens the door for intrinsic activity assessment. Initially, the raw ORR currents for the agglomerates containing Nafion are presented. Thereafter, by normalizing thousands of individual measurements by their unique electrochemical surface area (ECSA), the activity maps in mA/cm^2 are obtained. Similarly, the raw and the ECSA-normalized currents are obtained for the Nafion-free agglomerates. Similar ORR current densities demonstrate the intrinsic ORR activity that is independent of surface area and Nafion content. SEM images of the SECCM scanned area are obtained, revealing the morphology of the studied agglomerates.

5.1 Nano electrochemistry coming to the rescue

From the previous chapters we saw that with RRDE and SECM methodologies, despite acquiring important information about a catalyst's activity, there are irrefutable experimental challenges that make the extraction of intrinsic activity and selectivity quite complicated. The core of the problematic was found to be the thickness of catalyst, which vastly influenced the number of transferred electrons. Even when the loading was further lowered in the SECM measurements, the size of the agglomerates had as well an impact on the selectivity and the overpotential. On the other hand, more Nafion content for the same loading also revealed less peroxide detected at the UME, complicating further the interpretation of results. Although, Nafion's role as a binder is crucial for a good dispersion and adherence on the electrode. Moreover, the resolution in SECM is limited to a few micrometers and the electrochemical information represents the global activity of many agglomerates in a deposit, making it impossible to establish the influence of individual agglomerates on the ORR activity.

Being able to zoom into tiny structures of the material and performing single entity electrochemistry could in principle get rid of such obstacles. The thickness of the layer would not be an impediment as small entities of material can be studied individually. For the same reason, the presence of Nafion and an excellent adherence on the electrode is not mandatory either. One of the SPM techniques which allows high resolution single entity electrochemical measurements is SECCM, with which one can perform electrochemistry in a nano-sized droplet in contact with the sample without any influence of the surrounding (Chapter II). Herein, the usage of nano-sized pipettes and a small hopping distance allows one to perform hundreds to thousands of individual measurements within one sample with ultra-high resolution, at a time-scale of only a few hours. To put it into perspective, what we would see as one pixel in a SECM map, we can discern as thousands of pixels in a SECCM map, which can further be coupled with SEM to correlate the activity with the morphology of the tiny particles (Figure 39). Therefore, this opens the door for unraveling interesting information about the properties of a given catalyst.

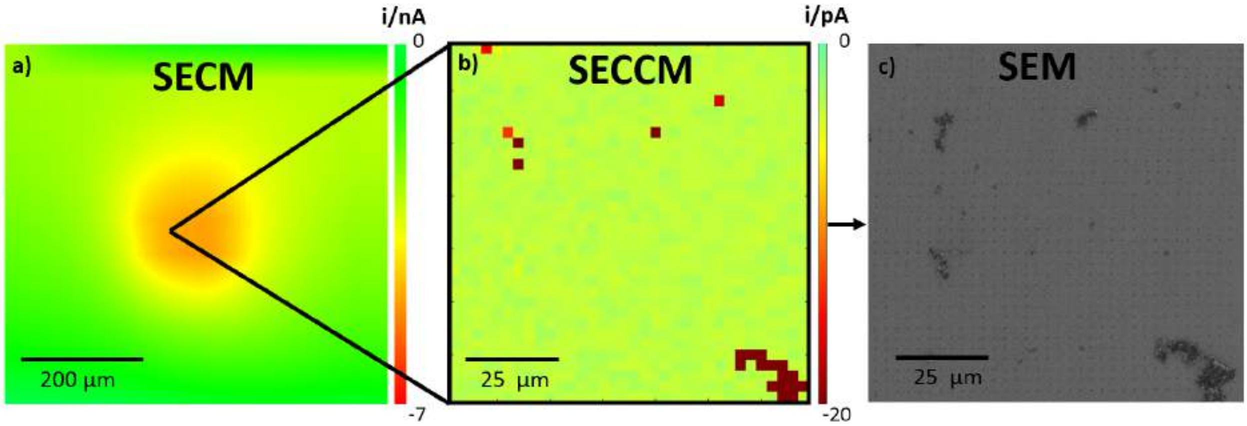

Figure 39 a) A scheme showing an example of a SECM map acquired with RC mode and 10 µm Au UME and b) how one pixel of that map can be discerned as thousands of pixels with an SECCM map, differentiating different catalyst agglomerates, c) SEM image of the same area scanned with SECCM. Note this is only an illustration, as both maps do not correspond to the same deposit.

In the following sections of this chapter, nano-scale SECCM is employed to investigate individual catalyst agglomerates with and without Nafion content, through high resolution surface area-normalized electrochemical data, thus unraveling the intrinsic ORR activity. When coupling with SEM, the morphology of the studied catalyst agglomerates is analyzed.

5.2 Experimental

5.2.1 Fabrication of the nanopipettes

A CO_2 laser puller (P-2000; Sutter Instruments) was utilized to pull single barrel quartz capillaries with filament (ZQF-120-90-10; Science Products) through a one-line program, leading to a single barrel pipette. Subsequently its diameter was determined by SEM (FEI, Quanta 3D ESEM). The pulling parameters utilized for certain capillary sizes are shown below and gave very reproducible results:

(d~150 nm): HEAT 720, FIL 4, VEL 45, DEL 130, PUL 90

(d~250 nm): HEAT 680, FIL 4, VEL 45, DEL 130, PUL 90

5.2.2 Deposit preparation and SECCM experiment

The catalyst ink was prepared with the same procedure as described in section 4.2.2. An additional ink was prepared with the same procedure, only excluding the Nafion in the formulation. The flat BDD substrate was rinsed with isopropanol and dried with argon, before to fixing it in the SECCM holder and contacting it with Cu tape, the conductivity of which was verified with a multimeter. Afterwards, the deposition was done by drop-casting a small drop of the ink on the substrate and letting it dry in air.

A home-built SECCM set-up was utilized for the electrochemical experiments, which was installed in a Faraday cage with thermal isolation panels (Vaku-Isotherm) and set on a vibrating damping table (RS 2000, Newport) with four S-2000 stabilizers (Newport). The pipette was filled with 0.05 M H_2SO_4 (99.999% purity, Sigma Aldrich) with a Ag/AgCl [3 M KCl] reference counter electrode inside and was fixed on a pipette holder. The BDD substrate was fixed on top of an x, y, z-piezo cube (P-611.3S nanocube; Physik Instrumente) where an analog amplifier (E-664, Physik Instrumente) aids for fine positioning. An optical camera (DMK 21AU04; The Imaging Source) and a cold light source (KL1500 LCD Schott) was used for visualization by eye while the substrate was initially positioned close to a region of interest, through a three-stepper motor driven micrometer screws (Owis) with an L Step PCIe (Lang) controller. Once the pipette was ~40 µm above the sample region of interest (working electrode, WE), the approach was done with a surface current (i_{surf}) threshold of 2.5 pA, in order for the contact of meniscus-WE to be detected and further translation to be terminated. The hopping mode protocol was employed for collecting electrochemical data at multiple points, within the restricted area established by the meniscus between the pipette and the substrate. The number of landing points was predefined prior to the experiment. Once the meniscus is in contact with the WE, a linear sweep voltammogram (LSV) in a range of 0.3 to -0.6 V vs Ag/AgCl was performed, followed by three cyclic voltammograms (CV) in a range of 0.65-0.7 V vs Ag/AgCl at scan rates of 2, 5 and 10 V/s, at each landing spot. The potentials were converted to reversible hydrogen electrode (RHE) via Equation 14, where the standard electrode potential for Ag/AgCl ($E^{o}_{(Ag/AgCl)}$) =0.210 V and pH=1.

$$E_{RHE} = E_{Ag/AgCl} + 0.059\,pH + E^{o}_{Ag/AgCl} \qquad 14$$

While the LSVs were translated to spatially-resolved voltametric image containing information about the activity of the sample, the CVs at a non-faradaic region were used to calculate the double layer capacitance. The z-position of approaches at all landing spots was translated to a topography map of the sample. The i_{surf} flowing through the RCE was determined through a variable gain transimpedance amplifier (DLPCA-200, FEMTO Messtechnik). A FPGA card (PCIe-7852R) served for data acquisition and instrumental control. This was managed through a modified version of a software developed in University of Warwick (WEC-SPM) written in LabVIEW (National Instruments). Matlab R2022a (Mathworks) software package was utilized to process all the raw electrochemical data and topography maps, with scripts written by Emmanuel Batsa Tetteh and Moonjoo Kim at Ruhr University in Bochum.

5.2.3 SEM measurements

The SEM images were acquired with a Quanta 3D ESEM (FEI) in high-vacuum mode, using an acceleration voltage of 30 kV. Prior to its investigation, the BDD substrate was put onto the aluminum SEM sample holder and contacted with a copper tape to the sample holder which prevents electrostatic charging.

5.3 Investigation of Nafion containing agglomerates

5.3.1 Raw ORR activity

Initially, the Fe-N-MWCNT catalyst ink with 5% Nafion was drop-casted on the flat BDD substrate and was subsequently analyzed with SECCM using a ~150 nm pipette. The SECCM measurement spanned an area of 40x40 μm^2, with a hopping distance of 0.8 μm leading to 51x51 landing points thus 2601 individual LSV measurements. Throughout the scan, the z-position of the capillary was monitored, generating a topography map as shown in Figure 40a, where the highest landing point corresponds to 730 nm for spot 1, followed by 666 nm and 380 nm for spot 2 and 3 respectively.

The LSVs recorded for all landing spots were translated into activity maps and the map at 0.56 V vs RHE is presented in Figure 40b, showing a homogeneous map with almost no current at such overpotentials.

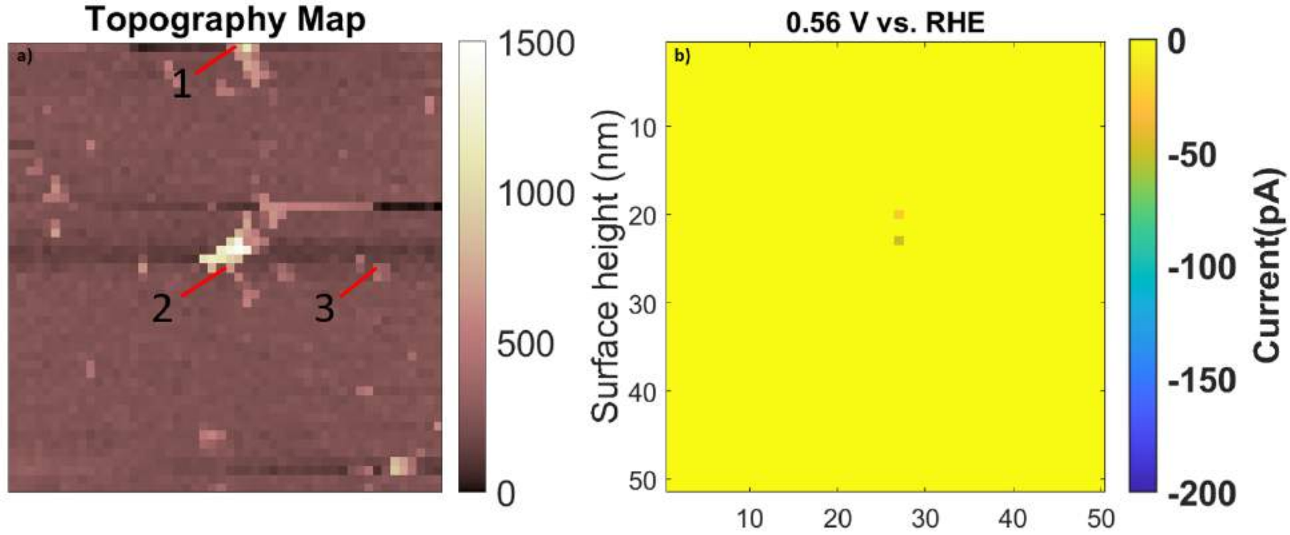

Figure 40 a) Topography map, b) SECCM activity map at 0.56 V vs RHE, scan size 40x40µm with a 0.8 µm hopping distance, acquired with a ~150 nm pipette.

On the other hand, the activity map at 0 V vs RHE in Figure 41a shows an inert BDD substrate covered with active catalyst spots which are easily distinguished with higher currents. The diameter of the individual catalyst nanotubes studied here (~11 nm, Annex I) is significantly smaller than the size of the pipette (~150 nm), therefore the high current areas could correspond to small agglomerates of many nanotubes. When analyzing the LSVs corresponding to designated pixels in the activity map (Figure 41b), spot 2 shows significantly higher current (200 pA) compared to spot 1 and 3 with <20 pA. Nevertheless, something that has to be taken into account when making comparisons within different spots is that their electrochemical surface area (ECSA) could be different, meaning that a simple high current - high activity conclusion could be misleading.

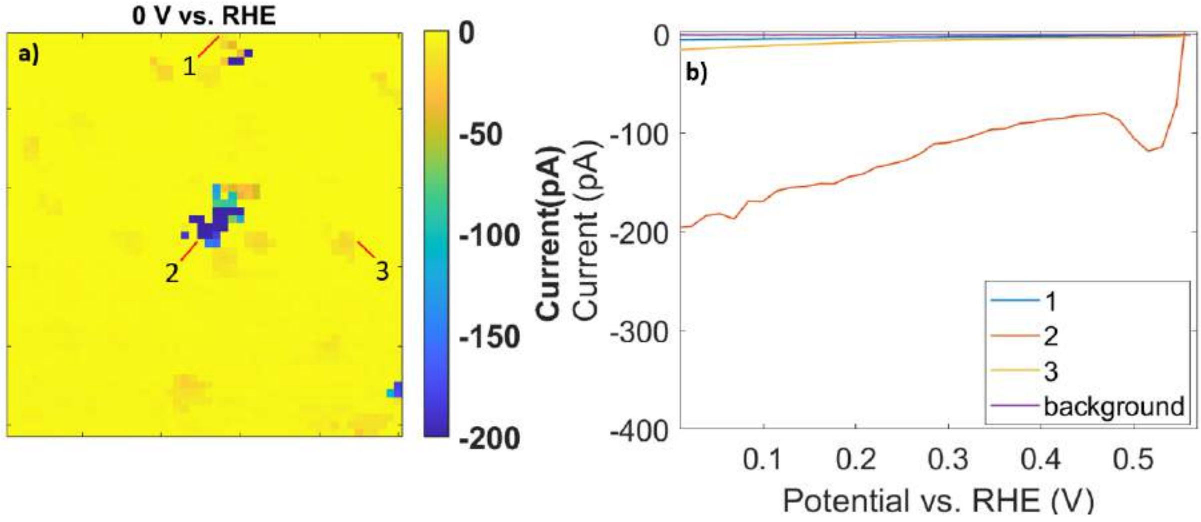

Figure 41 a) Activity map showing the current in pA at 0 V vs RHE, b) corresponding LSVs for the designated pixels in the activity map, showing current (pA) vs *E* vs RHE. Data corresponds to the scan with 40x40 µm, 0.8 µm hopping distance and ~150 nm pipette.

5.3.2 ECSA normalized ORR activity

The raw currents presented in the previous section were further normalized by the ECSA, which can be derived from the double layer capacitance (C_{dl}) and specific capacitance (C_s) according to the expression ECSA=C_{dl}/C_s. Cyclic voltammograms (CVs) were performed at different scan rates in a non-faradaic potential region (0.906 V – 0.956 V vs RHE) (Figure 42) and from the slope of current vs scan rate, the C_{dl} was extracted. The coefficient of determination (R^2) for the fits of each pixel (landing point) is used to verify the quality of the fit (presented in Figure 43a) and the chosen spots for this study exhibited an $R^2 \geq 0.97$ (values in Table 3). The C_{dl} map and its values for all designated spots are shown in Figure 43b and Table 3 respectively. The C_{dl} was divided with a value of C_s (0.0415 F/cm^2) reported for carbon nanotubes (CNT),[190] hence acquiring the ECSA in cm^2 and using it to normalize the current.

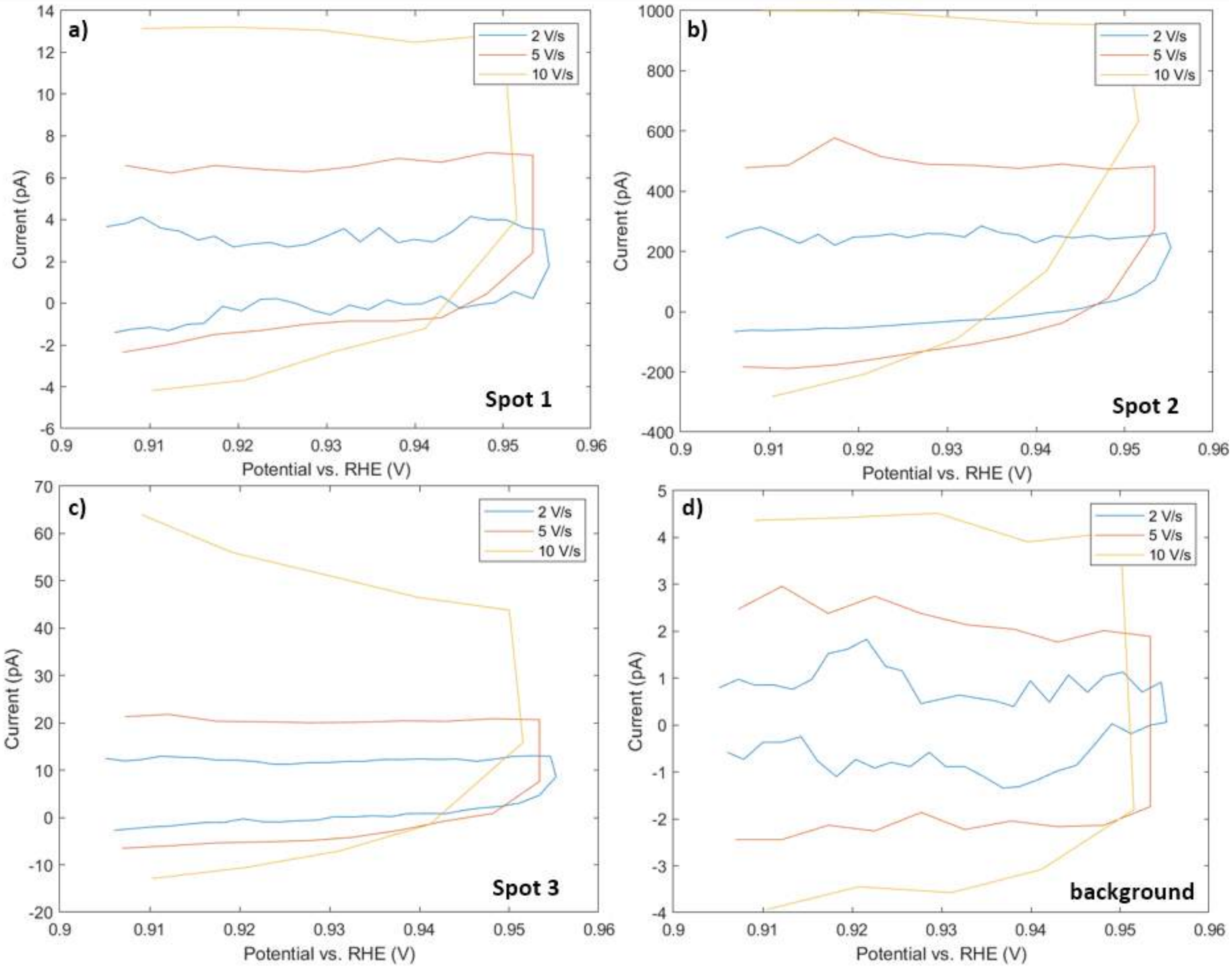

Figure 42 CVs at a potential range of 0.906V to 0.956 V at scan rates of 2,5 and 10 V/s for a) spot 1, b) spot 2, c) spot 3 and d) the background. Data corresponds to the 40x40µm scan with a 0.8 µm hopping distance, acquired with a ~150 nm pipette.

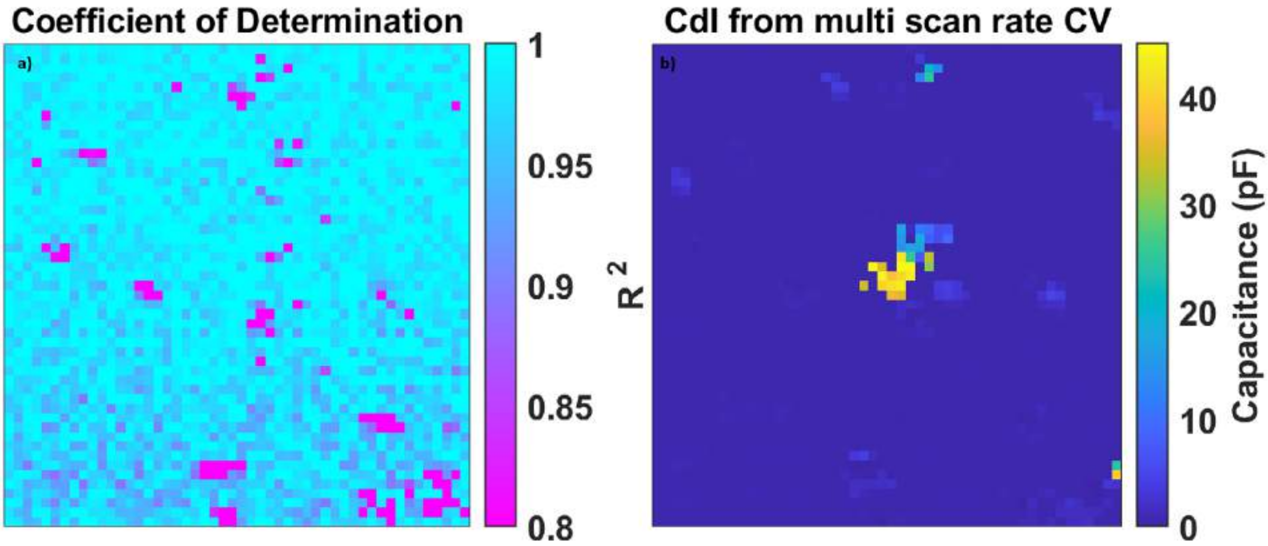

Figure 43a) Coefficient of determination R^2 acquired from the fitting of current vs scan rate, b) double layer capacitance C_{dl} acquired from the slope of current vs scan rate. Data corresponds to the 40x40 µm scan, 0.8 µm hopping distance and ~150 nm pipette.

Table 3 Coefficient of determination of current vs scan rate slopes and double layer capacitance values for all designated spots.

	Spot 1	Spot 2	Spot 3	Background
R^2	0.99	0.99	0.97	0.99
C_{dl} (pF)	0.68	42.24	2.8	0.36

The ECSA normalized LSVs in Figure 44b show more similar current density between -200 and -325 mA/cm^2 rather than the disparate currents in Figure 41b. When analyzing the shape of LSVs, one can see that they do not exhibit diffusion limited current (j_L) due to the high O_2 mass transport in the small droplet, in which case the j_L is shifted to more cathodic potentials.[122,123] For the same reason, the observed current values are orders of magnitude higher than one would foresee.[191]

Moreover, while the LSVs correspond to specific designated spots, the activity map gives us an overall idea of the activity during the whole scan. After normalizing the current with ECSA, the activity map exhibits higher currents throughout the lower half of the substrate (Figure 44a) which is vastly different from the non-normalized map in Figure 41a. The upper part of the scan also shows higher current densities, apparent on the LSV of the background (-60 mA/cm^2).

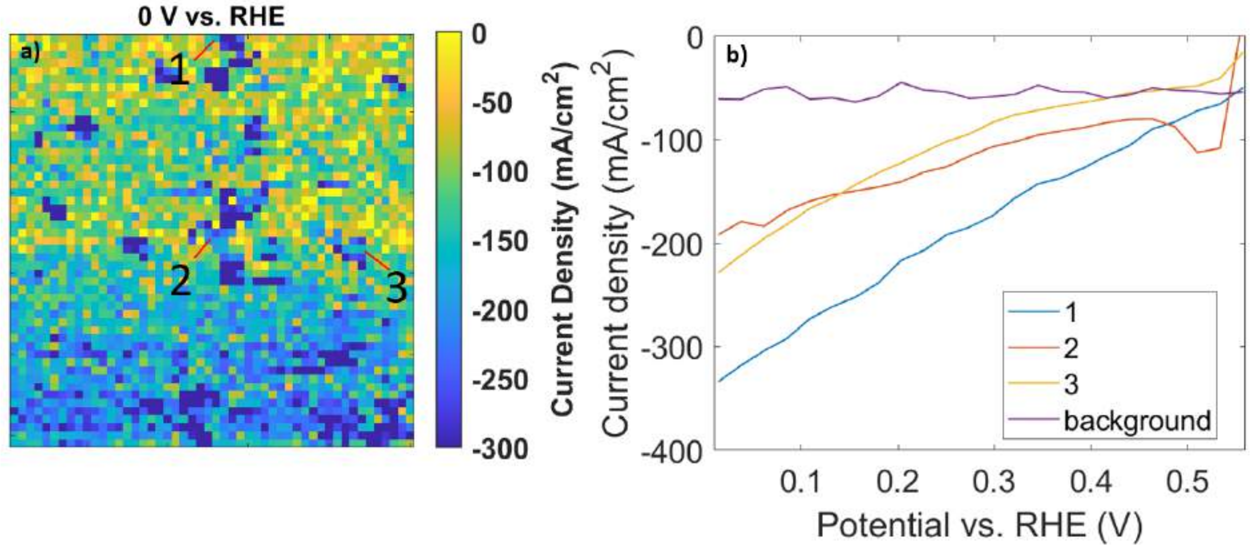

Figure 44 a) activity map normalized by ECSA showing the current density in mA/cm2 at 0 V vs RHE, b) corresponding LSVs for the designated pixels in the normalized activity map, showing current density (mA/cm^2) vs *E* vs RHE. Data corresponds to the scan with 40x40, 0.8 µm hopping distance and a ~150 nm pipette.

5.3.3 SEM investigation of the scanned area

To get further insight on the appearance of normalized activity map in Figure 44a, subsequently we analyzed the SECCM scanned area of the sample with SEM (Figure 45). The lower half of the scan was actually flooded with no individual landing spots, explaining the higher current gradient on the same region in Figure 44a. It should be noted that all data were normalized by using a C_s corresponding to CNT (0.0415 F/cm^2), while the C_s value for the BDD substrate is typically only about 3 µF/cm^2.[192] This might have led to an ECSA lower than predicted, hence leading to a higher current density in the background (BDD). To confirm this, the ECSA normalized activity map considering the BDD C_s is shown in Figure 46 with almost no current, where of course, herein the activity of the catalyst spots does not appear in the map. This explains the high background current in Figure 44b. It is evident that only by ECSA normalization and usage of the appropriate C_s, one can have an idea about the quality of the experiment with the intrinsic activity of the catalyst and the inertness of the BDD substrate in the applied potential region.

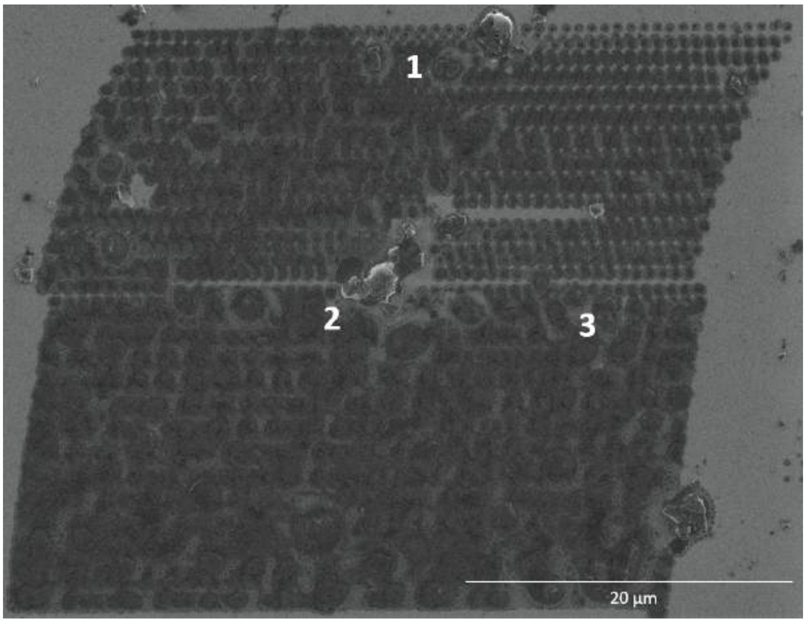

Figure 45 SEM image showing the traces of the SECCM scan with a size of 40x40 µm, 0.8 µm hopping distance and ~150 nm pipette.

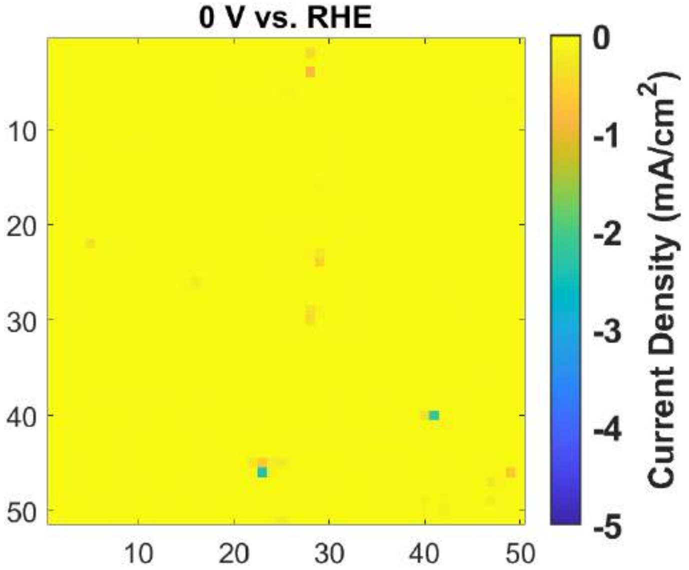

Figure 46 ECSA normalized activity map considering the specific capacitance of BDD (3µF/cm^2) rather than the catalyst one. Data from the 40x40 µm2 scan with a 0.8 µm hopping distance, acquired with a ~150 nm pipette.

Furthermore, we zoomed onto the individual catalyst spots with SEM (Figure 47) in order to have an insight on the morphology of the catalyst. The structure of the material was undetermined in most of the spots, with the exception of spot 2 where one can recognize the carbon nanotubes more clearly. Considering that the SEM images reveal smooth and liquid-like features of the catalyst, it was assumed this could be due to Nafion present in the catalyst ink which may have overshadowed the nanotubes underneath, making the images inconclusive.

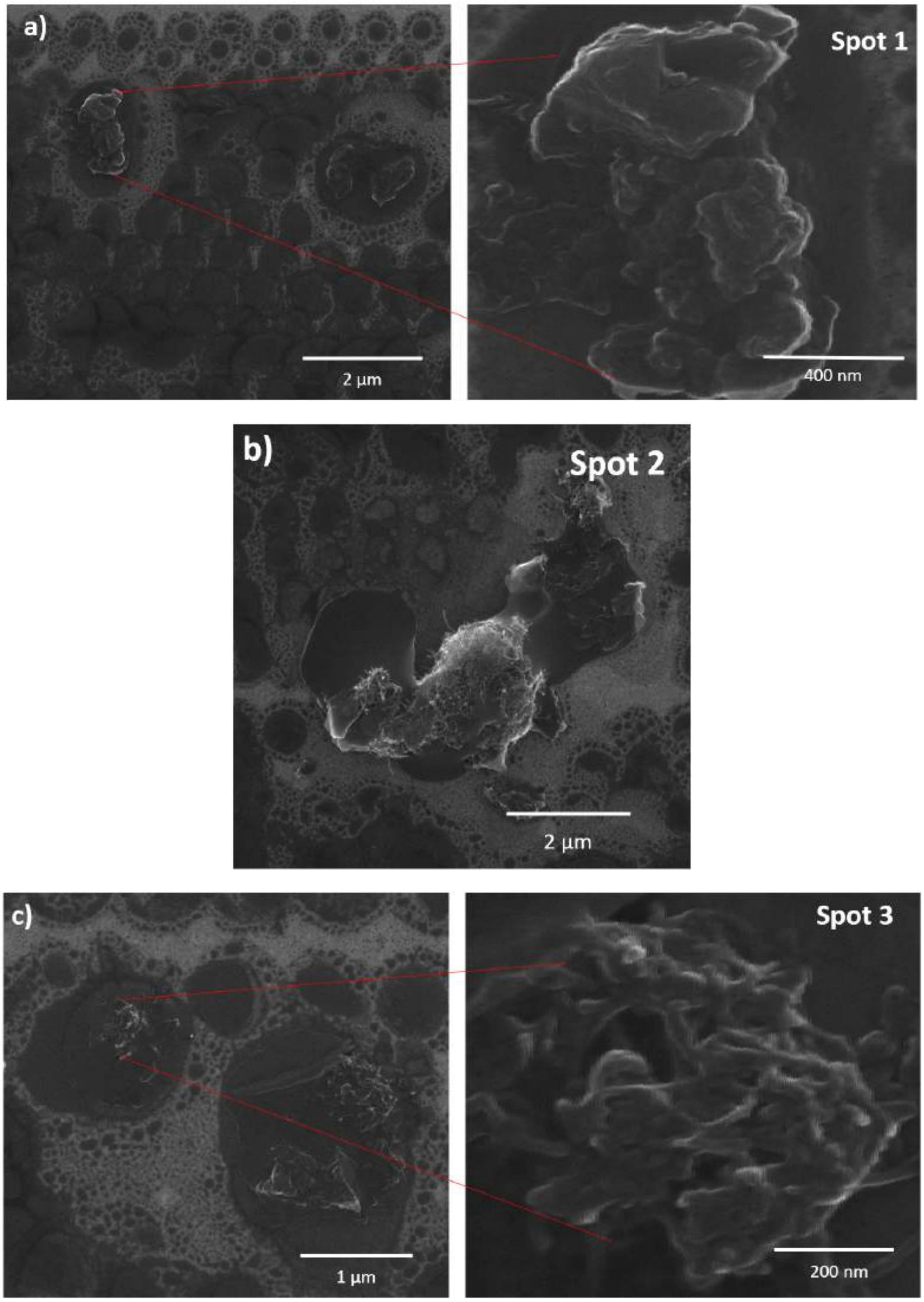

Figure 47 SEM images of all designated spots (1,2,3) corresponding to the traces of the SECCM scan with 40x40 µm size, 0.8 µm hopping distance, ~150 nm pipette.

5.4 SECCM investigation of Nafion-free agglomerates

5.4.1 Raw ORR activity

In order to better visualize the structure of the catalyst in SEM and to acquire the real activity without Nafion influence, another measurement was done by drop-casting a catalyst ink without Nafion in its formulation. As such, the dispersion of the catalyst was not as good, leaving fewer spots deposited on the substrate. To increase the chances of landing on the catalyst spots during the SECCM experiment and to avoid overlapping of landing spots, the scan area was increased to 100x100 μm^2 with a hopping distance of 3 µm, therefore 986 (29x34) individual landing spots and the capillary size was ~250 nm. The topography map shows the flat substrate where the landing points at the studied pixels correspond to different heights, starting from 654 nm, to 721 nm and 1040 nm for spot 1, 2 and 3 respectively, as depicted in Figure 48a along with the activity map at 0.56 V vs RHE in Figure 48b. The map at 0 V vs RHE is shown in Figure 49a where most agglomerates were caught only by one landing point, making the majority of catalyst spots appear as single pixels in the activity map. These pixels could be counted in the SECCM map and could more precisely be found in SEM by counting the droplet traces, making it more convenient for analysis. The non-normalized activity map and the corresponding LSVs in Figure 49a,b) show a trend of increasing current from spot 1 to spot 3 (from -25 to -325 pA).

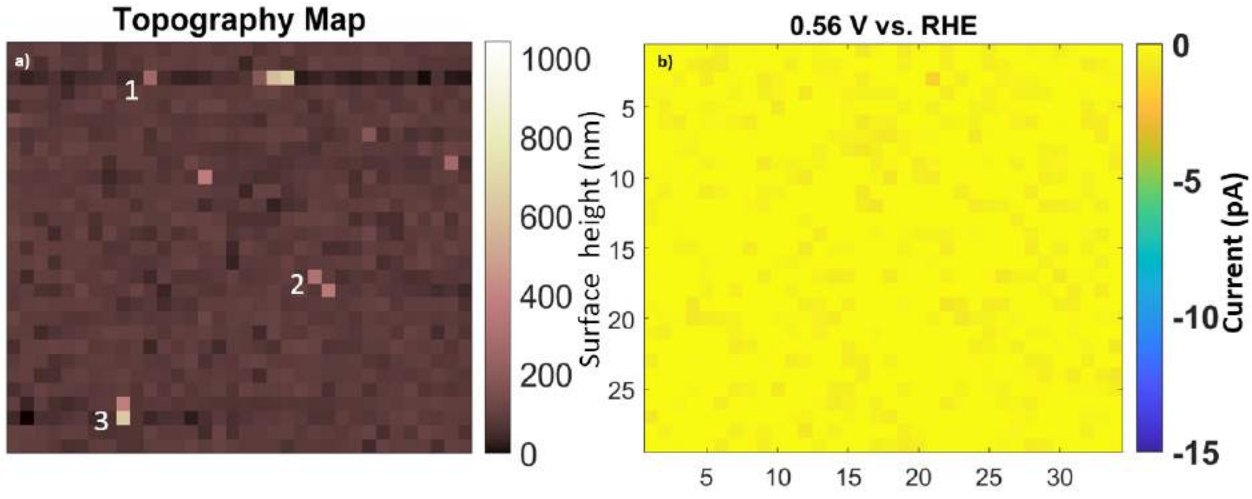

Figure 48 a) topography map, b) SECCM activity map at 0.56 V vs RHE. Scan size 100x100µm with 3 µm hopping distance and a ~250 nm pipette.

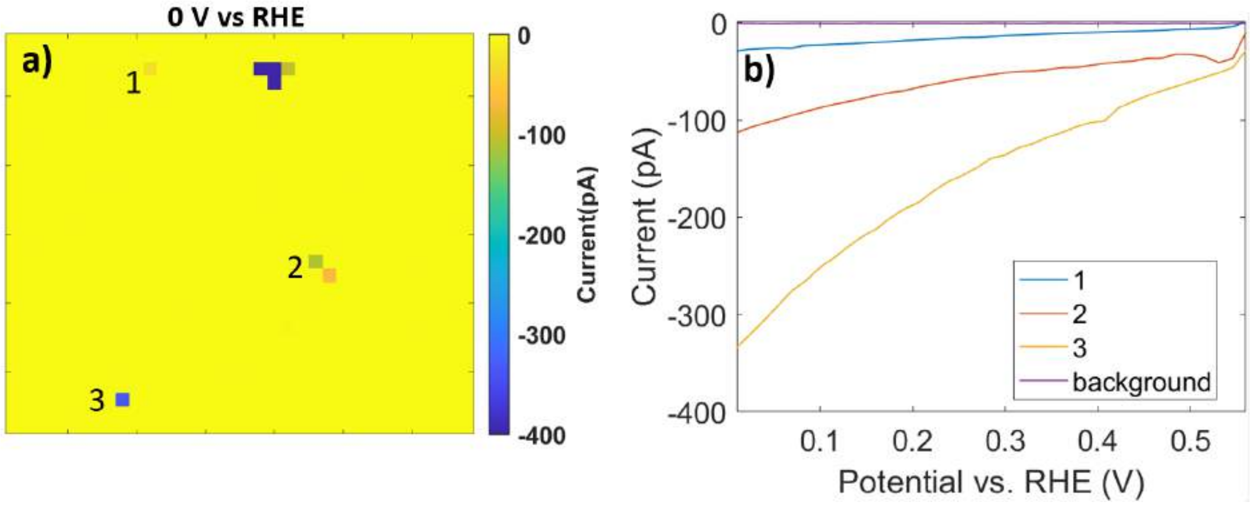

Figure 49 a) Activity map showing the current in pA at 0 V vs RHE, b) corresponding LSVs for the designated pixels in the activity map showing current (pA) vs *E* vs RHE. Data corresponds to the 100x100 µm scan with 3 µm hopping distance and ~250 nm pipette.

5.4.2 ECSA normalized ORR activity

As in the previous section, CVs at different scan rates were performed in order to acquire C_{dl} and ECSA so that the current can be normalized by the surface area. The CVs are presented on Figure 50 while the corresponding R^2 map, the C_{dl} map and their values for all spots are shown in Figure 51 and Table 4. The spots investigated inhere exhibit a $R^2 \geq 0.99$ and the ones with very low R^2 were considered as artefacts and not further investigated, for example the pink spots in Figure

51a. When the current is normalized by the ECSA as shown in Figure 52a,b, all designated spots level to a similar current density values between -225 and 325 mA/cm^2 instead of the distinct ones observed in Figure 49. These values are interestingly similar to the ones in Figure 44 too, where the catalyst contained Nafion in its formulation. It has been reported in macroelectrode (RRDE) investigations that the higher content of Nafion lead to an inhibition of ORR due to the blockage of active sites from the Nafion self-assembly.[193] In the nano scale study however, such events and the non-electroconductive nature of Nafion did not play a role on the ORR results. Doubtlessly, this is a demonstration of the intrinsic activity of the catalyst where the current is similar independently of Nafion content. The high background current after normalization is explained due to the different C_s of BDD, similarly as before. The activity map normalized considering a C_s of 3 µF/cm^2 is presented in Figure 53.

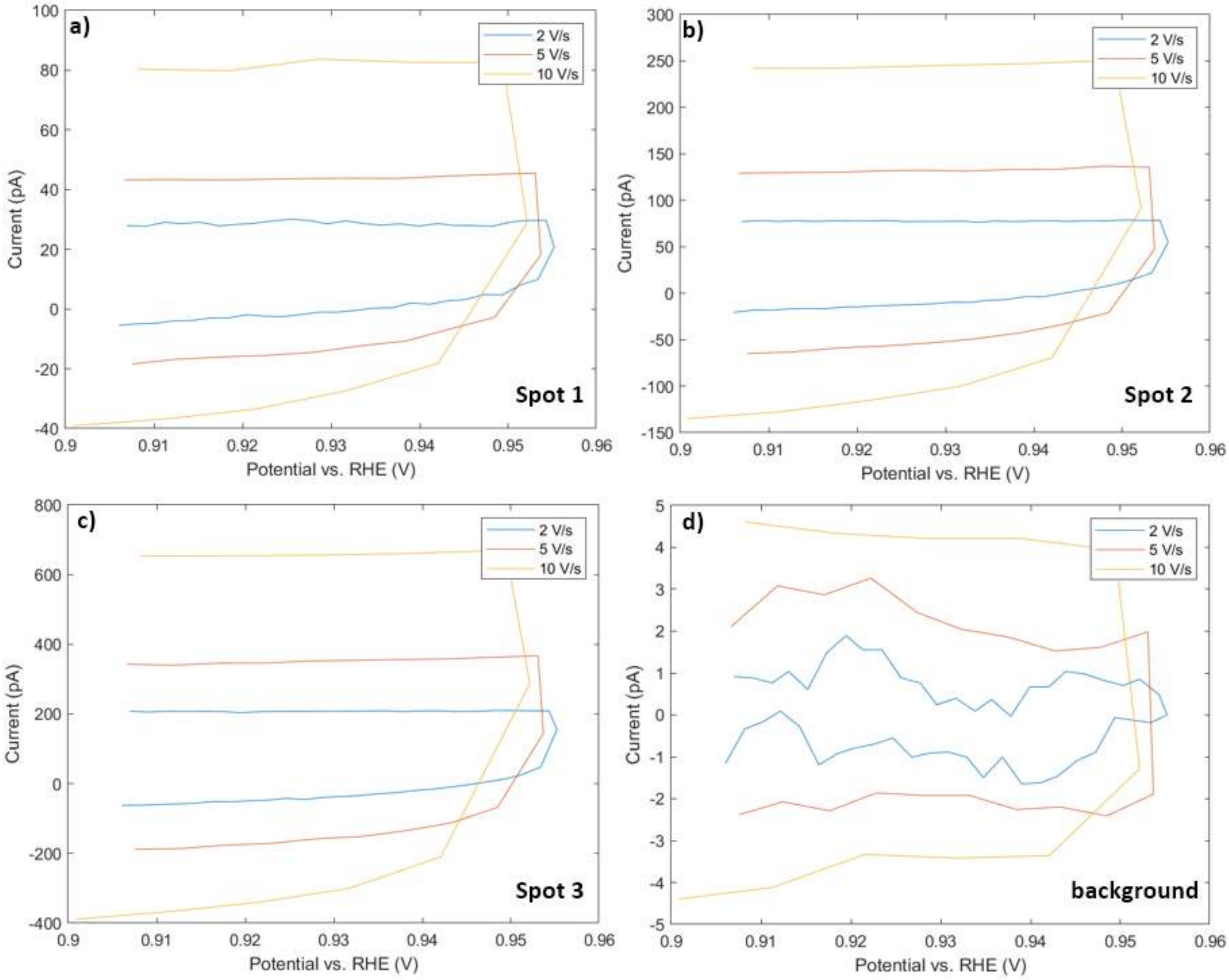

Figure 50 CVs at a potential range of 0.906 V to 0.956 V at scan rates of 2,5 and 10 V/s for a) spot 1, b) spot 2, c) spot 3 and d) the background. Data from the 100x100 µm scan with a 3 µm hopping distance, acquired with a ~250 nm pipette.

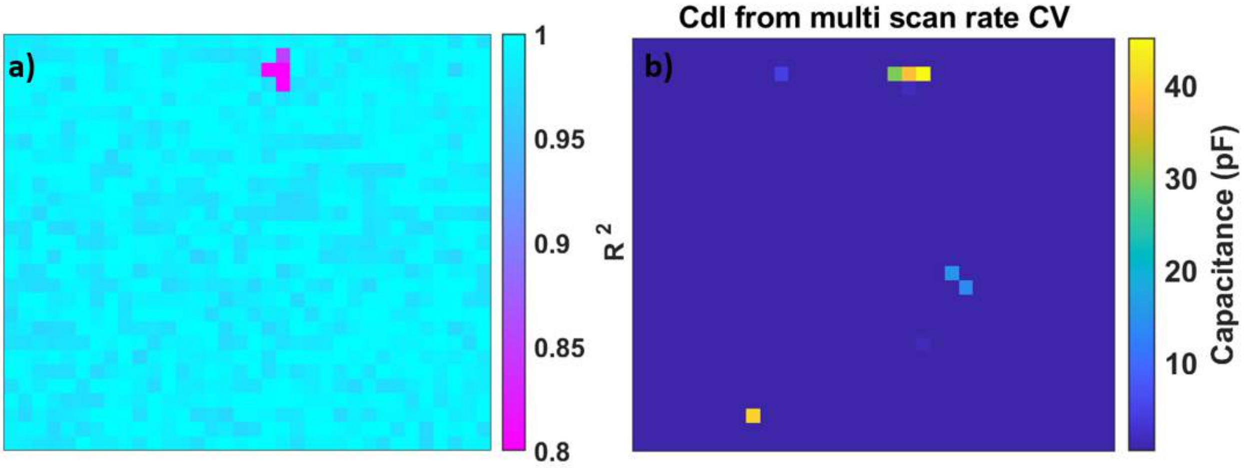

Figure 51 a) Coefficient of determination (R^2) acquired from the fitting of current vs scan rate, b) double layer capacitance C_{dl} acquired from the slope of current vs scan rate. Data from the 100x100 µm scan with 3 µm hopping distance, ~250 nm pipette.

Table 4 Coefficient of determination of current vs scan rate slopes and double layer capacitance values for all designated spots.

	Spot 1	Spot 2	Spot 3	Background
R^2	0.99	1.0	0.99	0.97
C_{dl} (pF)	4.7	14.9	40.5	0.45

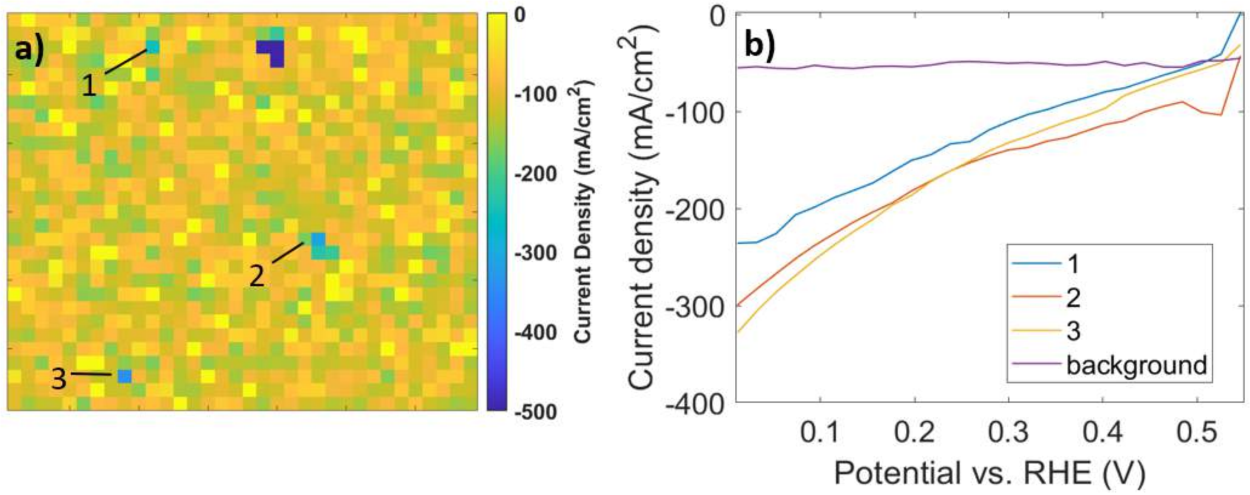

Figure 52 a) Activity map normalized by ECSA showing the current density in mA/cm² at 0 V vs RHE, b) corresponding LSVs for the designated pixels in the normalized activity map, showing current density (mA/cm²) vs *E* vs RHE. Data corresponds to the scan with 100x100, 3 µm hopping distance and ~250 nm pipette.

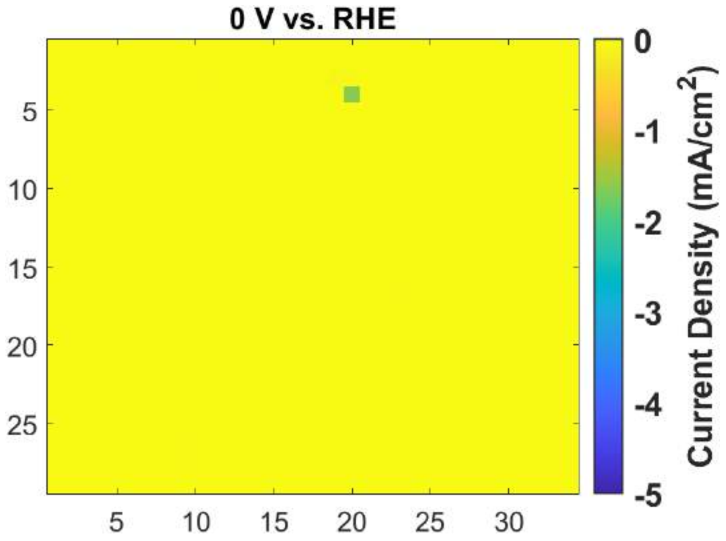

Figure 53 ECSA normalized activity map considering the specific capacitance of BDD (3 µF/cm²) rather than the catalyst one. Data from the 100x100 µm2 scan with a 3 µm hopping distance, acquired with a ~250 nm pipette.

5.4.3 SEM investigation of the scanned area

The scanned area was analyzed subsequently with SEM and the image of the full scan is shown in Figure 54, where at these experimental parameters the traces of the meniscus are well separated and there was no flooding occurring. Thereafter we zoomed into the individual studied spots shown in Figure 55 for a clearer insight on the morphology. Herein one can recognize clearly the presence of nanotubes due to the absence of Nafion in the catalyst. All agglomerates exhibit a mixture of nanotubes and block like structures, although their ratio seems to be different in the distinct agglomerates. To start with, spot 1 has a morphology dominated by nanotubes, while in spot 2 one can recognize only block-like structures rather than anything else. Moreover, spot 3 exhibits a more clear-cut mixture of the two components, with some nanotubes along with block-like structures. Nevertheless, nanotube or not, the ECSA normalized current densities suggest similar ORR activity in all agglomerates, demonstrating once more the steady ORR activity.

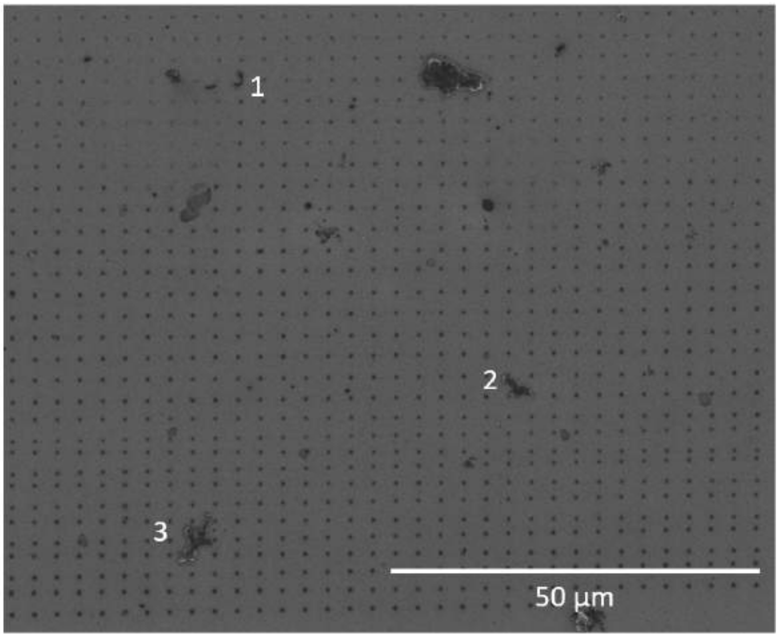

Figure 54 SEM image showing the traces of the SECCM scan with a size of 100x100 µm and 3 µm hopping distance and ~250 nm pipette.

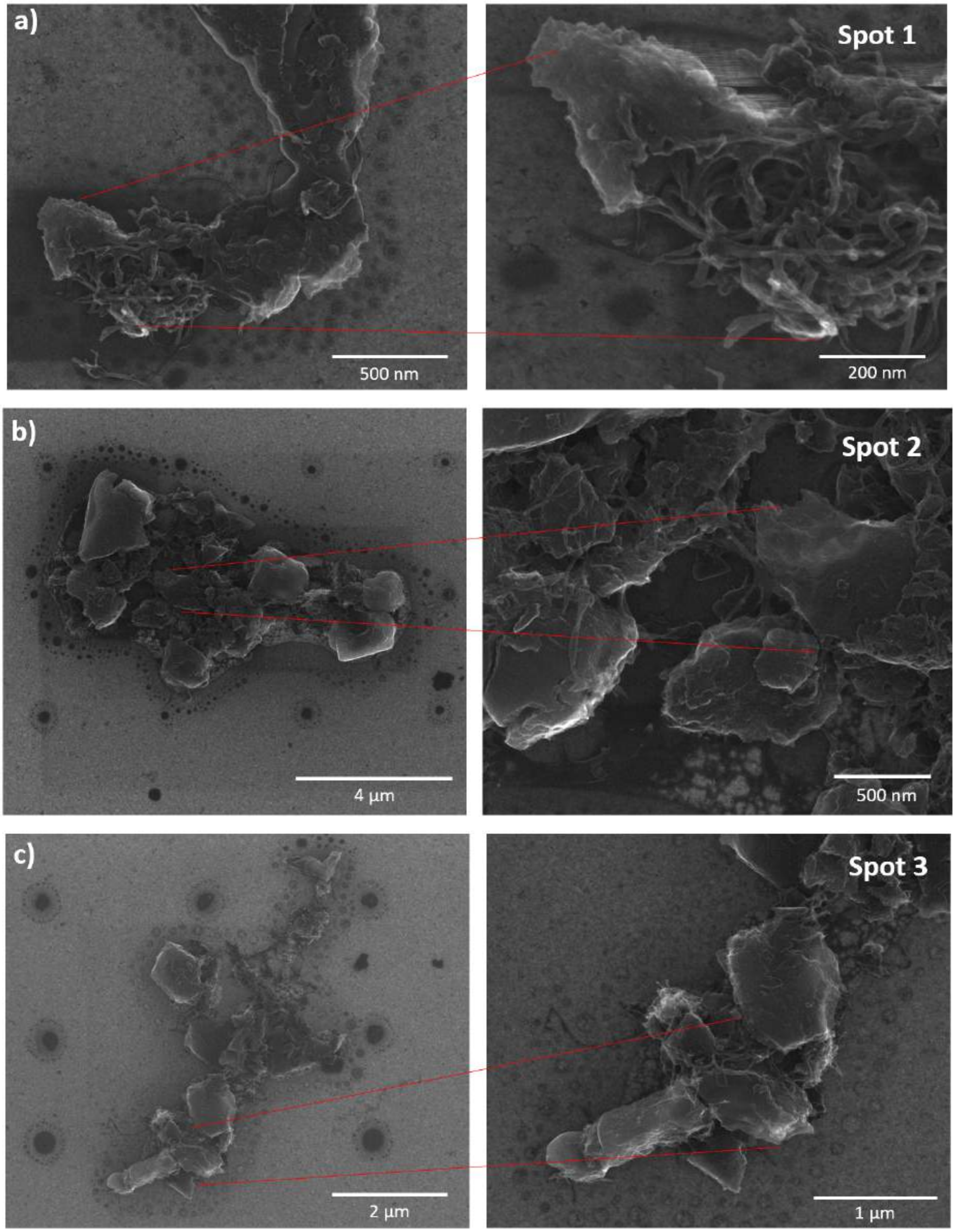

Figure 55 SEM image of all designated spots (1,2,3) corresponding to the traces of SECCM scan with 100x100 µm size, 3 µm hopping distance and ~250 nm pipette.

5.5 Conclusion

In this chapter, the Fe-N-MWCNT catalyst was investigated at nano-scale resolutions via SECCM. Initially a catalyst deposit with Nafion content was analyzed, where the raw currents varied significantly within different agglomerates. When the currents were normalized by the ECSA, the current density of all spots leveled to a similar value of (~250 mA/cm^2 in average). The values of current densities acquired were quite high due to rapid mass transfers in the confined nm-scale meniscus. The SEM images of the studied spots did not reveal clearly the nanotubes due to the presence of Nafion in the catalyst ink. Thereafter, another deposit without Nafion content was investigated. When the current was normalized by the ECSA, the ORR activity was similar to the agglomerates with Nafion content. Moreover, alike current densities are obtained for different spots containing variable proportions of nanotubes and block-like structures-as investigated with SEM. Overall, the nanomaterial morphology does not seem to be a key parameter influencing the intrinsic ORR activity and this can have crucial implications regarding future synthesis strategies. Nevertheless, further studies of a wider variety of morphologies would be imperative for a more unambiguous conclusion.

However, an important parameter which was not able to be acquired herein is the selectivity (*n*), due to the fact that there is only the substrate as the unique WE with no other means to detect the intermediate. Perhaps if one would fabricate a double-barrel pipette with a platinum nanoelectrode in one of the barrels, detecting peroxide would be possible, albeit tricky. Nevertheless, the shape of the LSVs in SECCM studies was often correlated also to the ORR pathway, where two waves in the voltammogram were attributed to a 2+2e$^-$ reduction pathway.[124,194] Consequently, the LSVs acquired herein might suggest a close to 4e$^-$ transfer pathway due to the absence of two separate waves. However, this would be an inordinate overstatement especially when considering the considerable amounts of peroxide detected in SECM and RRDE measurements. Consequently, the intrinsic number of transferred electrons remains an ongoing problematic ought to be solved by the community for a fair prediction of catalyst aptness for FC applications.

Conclusion and perspectives

The unambiguous evaluation of ORR activity in the laboratory scale is crucial for an accurate catalyst performance prediction on fuel cells. This is especially important when it comes to ORR selectivity assessment (number of electrons), considering that an unforeseen H_2O_2 production in a FC would be extremely undesirable. This thesis explicated several electrochemical characterization techniques with which a Fe-N-MWCNT catalyst was investigated.

Starting from RRDE method in Chapter III which was utilized to investigate the material for its activity and selectivity, the results highlighted the influence of electrode loading on the shape of ORR voltammograms and on the number of transferred electrons. Considering the former, the less sigmoidal voltammograms at lower loadings were justified with a hypothesis that a resistance inside the agglomerate screens the applied potential, and this resistance diminishes when more agglomerates (higher loading) are added due to a distribution of local current. This was further confirmed with another set of experiments with a ball milling-treated ink, in which case the agglomerates are smaller and with less screening effect, therefore with improved voltammogram slopes. This significant outcome implies that a non-sigmoidal shaped voltammogram suggests poor organization of material due to certain processing conditions. On the other hand, the selectivity study revealed that the peroxide produced by the catalyst changed significantly with the loading, therefore remaining unclear as to what is the intrinsic *n* of the material. On Chapter IV, advantage of SECM was taken as a micro-scale technique which allowed the study of lower loadings than RRDE. It was predicted that if the catalyst thickness was low enough, there would be less complications coming from the CL. A new SECM dual-electrode investigation approach was used successfully in this work, namely an Au UME for ORR detection and Pt UME for H_2O_2 detection. Whilst SECM unraveled interesting information about the catalyst's ability for peroxide production, the varying *n* with loading was still apparent. However, it was interesting to observe that the intrinsic selectivity of the material is actually closer to 2, an information which is not apparent with higher loadings in RRDE measurements. However, generally both RRDE and SECM are dependent on experimental parameters which are difficult to be rigorously controlled. Extremely fine homogeneous layers are required with small and equally distributed agglomerates, whose Nafion content should be tailored for the specific material studied.

Finally, the situation in which no thickness factor or Nafion content was relevant to the outcome was achieved by nano-scale measurements with SECCM. Zooming into small agglomerates of the catalyst and evaluating their catalytic activity individually was the unique approach that gave access to the intrinsic ORR activity of the catalyst. The same ORR activity was obtained in mA/cm^2 for different agglomerates with and without Nafion content. The SEM images also reveal that all agglomerates with non-identical morphology exhibited similar current densities. However, the n which was one of the main tackled problematics in this thesis, was not possible to be assessed with SECCM due to the presence of only one working electrode.

Overall, this work dealt with a step that is usually overlooked in the community, namely the way we evaluate intrinsic ORR activity with electrochemical methods. The results acquired in this thesis stress the judicious implementation of RRDE and SECM, while the power to accurately evaluate the intrinsic ORR activity with SECCM was unleashed. One would have to agree with Francisco Zaera that: '*Only by making catalytic performance and not catalysis synthesis the center of attention will real progress in catalyst development be made*'.[195]

Annex I: Catalyst synthesis and characterization

Iron acetate (Alfa Aesar), Zinc nitrate (Alfa Aesar) and 2-methylimidazole (Alfa Aesar) (forming a MOF) and carbon nanotubes (NC 7100 from Nanocyl) were mixed 30 minutes in ethanol. Then, the solvent was removed by evaporation. The powder has undergone a first pyrolysis at 900 °C for 1 h under argon, followed by a second pyrolysis at 900 °C for 30 min in an NH_3 atmosphere without any acid treatment. Zinc is removed when the temperature is increased, leaving behind a porous carbon material.

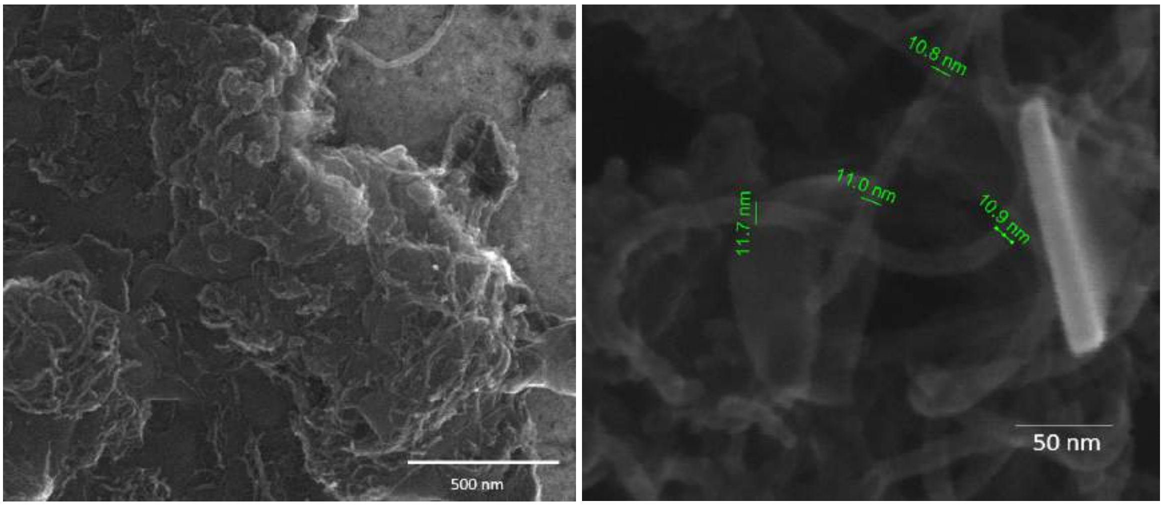

Figure 56 SEM images of the Fe-N-MWCNT catalyst, revealing its morphology and diameter of nanotubes.

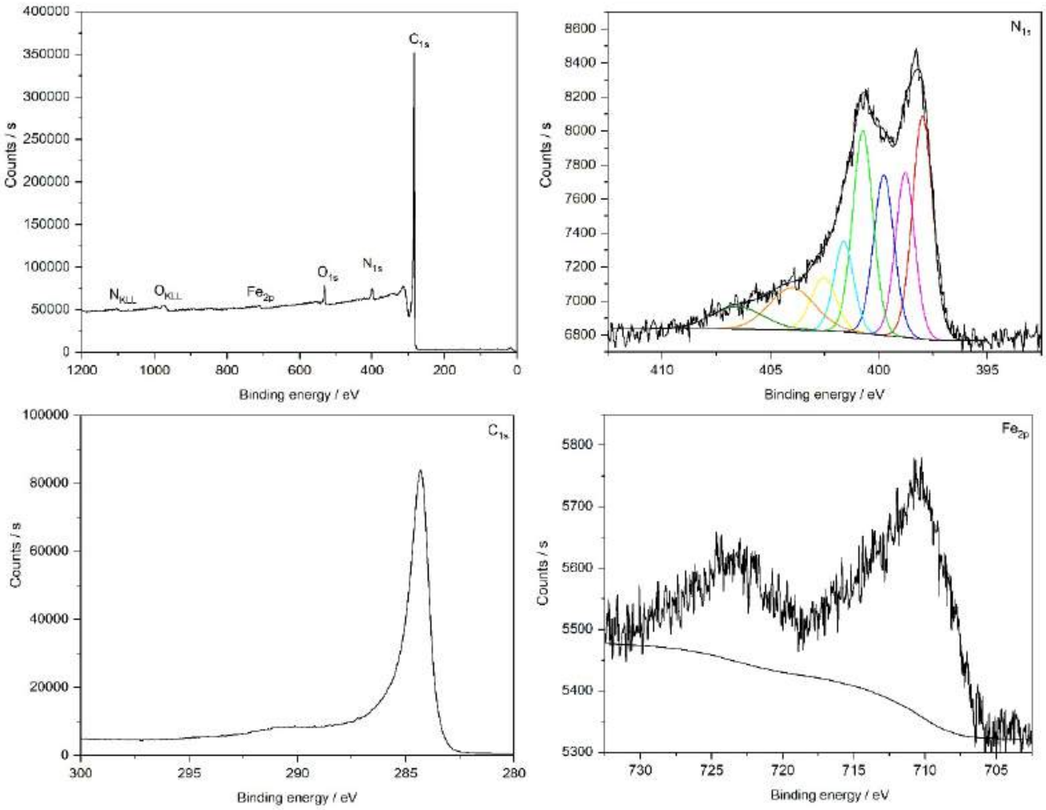

Figure 57 XPS spectra of the catalyst. XPS analyses were performed to show that this material was composed on surface of Carbon, Oxygen, Nitrogen and Iron with percentages of 94.2, 2.9, 2.7 and 0.2 respectively.

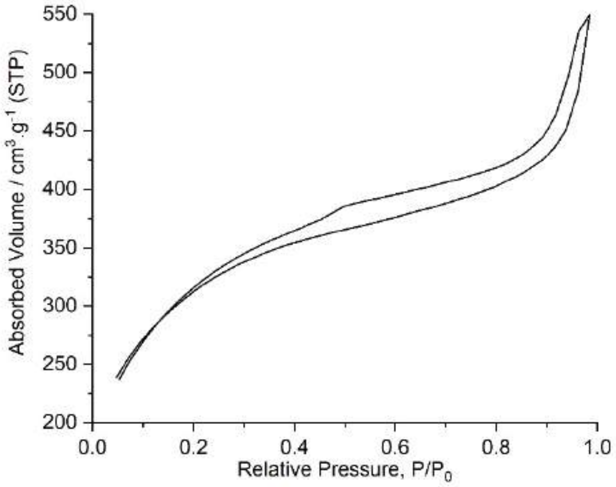

Figure 58 Nitrogen adsorption–desorption BET isotherm. The surface area is 1132 m^{2}g^{-1}.

Annex II: Articles

1. Limani, N.; Boudet, A.; Blanchard, N.; Jousselme, B.; Cornut, R. Local Probe Investigation of Electrocatalytic Activity. Chem. Sci. 2021, 12 (1), 71–98. https://doi.org/10.1039/D0SC04319B.

2. Boudet, A.; Henrotte, O.; Limani, N.; El Orf, F.; Oswald, F.; Jousselme, B.; Cornut, R. Unraveling the Link between Catalytic Activity and Agglomeration State with Scanning Electrochemical Microscopy and Atomic Force Microscopy. Anal. Chem. 2022, 94 (3), 1697–1704. https://doi.org/10.1021/acs.analchem.1c04256

3. Henrotte, O.; Boudet, A.; Limani, N.; Bergonzo, P.; Zribi, B.; Scorsone, E.; Jousselme, B.; Cornut, R. Steady-State Electrocatalytic Activity Evaluation with the Redox Competition Mode of Scanning Electrochemical Microscopy: A Gold Probe and a Boron-Doped Diamond Substrate. ChemElectroChem 2020, 7 (22), 4633–4640. https://doi.org/10.1002/celc.202001088.

4. Limani, N.; Tetteh, EB.; Kim, M.; Quast, T.; Scorsone, E.; Jousselme, B.; Schuhmann, W.; Cornut, R. Scrutinizing intrinsic oxygen reduction reaction activity of a Fe-N-MWCNT catalyst via scanning electrochemical cell microscopy. (submitted)

5. Two articles concerning the RRDE work of Chapter III and the SECM work of Chapter IV are being prepared.

References

(1) Fan, J.; Chen, M.; Zhao, Z.; Zhang, Z.; Ye, S.; Xu, S.; Wang, H.; Li, H. Bridging the Gap between Highly Active Oxygen Reduction Reaction Catalysts and Effective Catalyst Layers for Proton Exchange Membrane Fuel Cells. *Nat Energy* **2021**, *6* (5), 475–486. https://doi.org/10.1038/s41560-021-00824-7.

(2) Abe, J. O.; Popoola, A. P. I.; Ajenifuja, E.; Popoola, O. M. Hydrogen Energy, Economy and Storage: Review and Recommendation. *International Journal of Hydrogen Energy* **2019**, *44* (29), 15072–15086. https://doi.org/10.1016/j.ijhydene.2019.04.068.

(3) Tucker, M. Carbon Dioxide Emissions and Global GDP. *Ecological Economics* **1995**, *15* (3), 215–223. https://doi.org/10.1016/0921-8009(95)00045-3.

(4) Jacobson, T. A.; Kler, J. S.; Hernke, M. T.; Braun, R. K.; Meyer, K. C.; Funk, W. E. Direct Human Health Risks of Increased Atmospheric Carbon Dioxide. *Nat Sustain* **2019**, *2* (8), 691–701. https://doi.org/10.1038/s41893-019-0323-1.

(5) Münzel, T.; Gori, T.; Al-Kindi, S.; Deanfield, J.; Lelieveld, J.; Daiber, A.; Rajagopalan, S. Effects of Gaseous and Solid Constituents of Air Pollution on Endothelial Function. *European Heart Journal* **2018**, *39* (38), 3543–3550. https://doi.org/10.1093/eurheartj/ehy481.

(6) Sun, Y.; Shen, C.; Lai, Q.; Liu, W.; Wang, D.-W.; Aguey-Zinsou, K.-F. Tailoring Magnesium Based Materials for Hydrogen Storage through Synthesis: Current State of the Art. *Energy Storage Materials* **2018**, *10*, 168–198. https://doi.org/10.1016/j.ensm.2017.01.010.

(7) Gray, H. B. Powering the Planet with Solar Fuel. *Nature Chemistry* **2009**, *1* (1), 7–7. https://doi.org/10.1038/nchem.141.

(8) Oreskes, N. The Scientific Consensus on Climate Change. *Science* **2004**, *306* (5702), 1686–1686. https://doi.org/10.1126/science.1103618.

(9) Gür, T. M. Review of Electrical Energy Storage Technologies, Materials and Systems: Challenges and Prospects for Large-Scale Grid Storage. *Energy Environ. Sci.* **2018**, *11* (10), 2696–2767. https://doi.org/10.1039/C8EE01419A.

(10) IEA« Tracking Transport 2020 », Paris, 2020. Https://Www.Iea.Org/Reports/Tracking-Transport-2020. https://www.iea.org/reports/tracking-transport-2020.

(11) Sun, Y.-F.; Zhang, Y.-J.; Su, B. How Does Global Transport Sector Improve the Emissions Reduction Performance? A Demand-Side Analysis. *Applied Energy* **2022**, *311*, 118648. https://doi.org/10.1016/j.apenergy.2022.118648.

(12) Zeng, X.; Li, M.; Abd El-Hady, D.; Alshitari, W.; Al-Bogami, A. S.; Lu, J.; Amine, K. Commercialization of Lithium Battery Technologies for Electric Vehicles. *Adv. Energy Mater.* **2019**, *9* (27), 1900161. https://doi.org/10.1002/aenm.201900161.

(13) Simon, B.; Ziemann, S.; Weil, M. Potential Metal Requirement of Active Materials in Lithium-Ion Battery Cells of Electric Vehicles and Its Impact on Reserves: Focus on Europe. *Resources, Conservation and Recycling* **2015**, *104*, 300–310. https://doi.org/10.1016/j.resconrec.2015.07.011.

(14) Shafique, M.; Rafiq, M.; Azam, A.; Luo, X. Material Flow Analysis for End-of-Life Lithium-Ion Batteries from Battery Electric Vehicles in the USA and China. *Resources, Conservation and Recycling* **2022**, *178*, 106061. https://doi.org/10.1016/j.resconrec.2021.106061.

(15) Narins, T. P. The Battery Business: Lithium Availability and the Growth of the Global Electric Car Industry. *The Extractive Industries and Society* **2017**, *4* (2), 321–328. https://doi.org/10.1016/j.exis.2017.01.013.

(16) Carrette, L.; Friedrich, K. A.; Stimming, U. Fuel Cells - Fundamentals and Applications. *Fuel Cells* **2001**, *1* (1), 5–39. https://doi.org/10.1002/1615-6854(200105)1:1<5::AID-FUCE5>3.0.CO;2-G.

(17) Sharma, S.; Ghoshal, S. K. Hydrogen the Future Transportation Fuel: From Production to Applications. *Renewable and Sustainable Energy Reviews* **2015**, *43*, 1151–1158. https://doi.org/10.1016/j.rser.2014.11.093.

(18) Pollet, B. G.; Kocha, S. S.; Staffell, I. Current Status of Automotive Fuel Cells for Sustainable Transport. *Current Opinion in Electrochemistry* **2019**, *16*, 90–95. https://doi.org/10.1016/j.coelec.2019.04.021.

(19) Jiao, K.; Xuan, J.; Du, Q.; Bao, Z.; Xie, B.; Wang, B.; Zhao, Y.; Fan, L.; Wang, H.; Hou, Z.; Huo, S.; Brandon, N. P.; Yin, Y.; Guiver, M. D. Designing the next Generation of Proton-Exchange Membrane Fuel Cells. *Nature* **2021**, *595* (7867), 361–369. https://doi.org/10.1038/s41586-021-03482-7.

(20) Balat, M. Potential Importance of Hydrogen as a Future Solution to Environmental and Transportation Problems. *International Journal of Hydrogen Energy* **2008**, *33* (15), 4013–4029. https://doi.org/10.1016/j.ijhydene.2008.05.047.

(21) Bockris, J. O. M. The Hydrogen Economy: Its History. *International Journal of Hydrogen Energy* **2013**, *38* (6), 2579–2588. https://doi.org/10.1016/j.ijhydene.2012.12.026.

(22) Wang, Y.-J.; Long, W.; Wang, L.; Yuan, R.; Ignaszak, A.; Fang, B.; Wilkinson, D. P. Unlocking the Door to Highly Active ORR Catalysts for PEMFC Applications: Polyhedron-Engineered Pt-Based Nanocrystals. *Energy & Environmental Science* **2018**, *11* (2), 258–275. https://doi.org/10.1039/C7EE02444D.

(23) Mekhilef, S.; Saidur, R.; Safari, A. Comparative Study of Different Fuel Cell Technologies. *Renewable and Sustainable Energy Reviews* **2012**, *16* (1), 981–989. https://doi.org/10.1016/j.rser.2011.09.020.

(24) Suter, T. A. M.; Smith, K.; Hack, J.; Rasha, L.; Rana, Z.; Angel, G. M. A.; Shearing, P. R.; Miller, T. S.; Brett, D. J. L. Engineering Catalyst Layers for Next-Generation Polymer Electrolyte Fuel Cells: A Review of Design, Materials, and Methods. *Adv. Energy Mater.* **2021**, *11* (37), 2101025. https://doi.org/10.1002/aenm.202101025.

(25) Xie, M.; Chu, T.; Wang, T.; Wan, K.; Yang, D.; Li, B.; Ming, P.; Zhang, C. Preparation, Performance and Challenges of Catalyst Layer for Proton Exchange Membrane Fuel Cell. *Membranes* **2021**, *11* (11), 879. https://doi.org/10.3390/membranes11110879.

(26) Velayutham, G.; Kaushik, J.; Rajalakshmi, N.; Dhathathreyan, K. S. Effect of PTFE Content in Gas Diffusion Media and Microlayer on the Performance of PEMFC Tested under Ambient Pressure. *Fuel Cells* **2007**, *7* (4), 314–318. https://doi.org/10.1002/fuce.200600032.

(27) Ma, R.; Lin, G.; Zhou, Y.; Liu, Q.; Zhang, T.; Shan, G.; Yang, M.; Wang, J. A Review of Oxygen Reduction Mechanisms for Metal-Free Carbon-Based Electrocatalysts. *npj Computational Materials* **2019**, *5* (1). https://doi.org/10.1038/s41524-019-0210-3.

(28) *PEM Fuel Cell Electrocatalysts and Catalyst Layers*; Zhang, J., Ed.; Springer London: London, 2008. https://doi.org/10.1007/978-1-84800-936-3.

(29) Shi, J.; Zhang, P.; Han, Y.; Wang, H.; Wang, X.; Yu, Y.; Sun, J. Investigation on Electrochemical Behavior and Surface Conductivity of Titanium Carbide Modified Ti Bipolar Plate of PEMFC. *International Journal of Hydrogen Energy* **2020**, *45* (16), 10050–10058. https://doi.org/10.1016/j.ijhydene.2020.01.203.

(30) Sasiwimonrit, K.; Chang, W.-C. To Improve the High Temperature Polymer Electrolyte Membrane Fuel Cells Performance by Altering the Properties of Catalyst Layer. *International Journal of Hydrogen Energy* **2020**, *45* (28), 14491–14499. https://doi.org/10.1016/j.ijhydene.2020.03.179.

(31) Bouleau, L.; Pérez-Rodríguez, S.; Quílez-Bermejo, J.; Izquierdo, M. T.; Xu, F.; Fierro, V.; Celzard, A. Best Practices for ORR Performance Evaluation of Metal-Free Porous Carbon Electrocatalysts. *Carbon* **2022**, *189*, 349–361. https://doi.org/10.1016/j.carbon.2021.12.078.

(32) Debe, M. K. Electrocatalyst Approaches and Challenges for Automotive Fuel Cells. *Nature* **2012**, *486* (7401), 43–51. https://doi.org/10.1038/nature11115.

(33) Rauf, M.; Zhao, Y.-D.; Wang, Y.-C.; Zheng, Y.-P.; Chen, C.; Yang, X.-D.; Zhou, Z.-Y.; Sun, S.-G. Insight into the Different ORR Catalytic Activity of Fe/N/C between Acidic and Alkaline Media: Protonation of Pyridinic Nitrogen. *Electrochemistry Communications* **2016**, *73*, 71–74. https://doi.org/10.1016/j.elecom.2016.10.016.

(34) Khotseng, L. Oxygen Reduction Reaction. In *Electrocatalysts for Fuel Cells and Hydrogen Evolution - Theory to Design*; Ray, A., Mukhopadhyay, I., K. Pati, R., Eds.; IntechOpen, 2018. https://doi.org/10.5772/intechopen.79098.

(35) Yeager, E. Electrocatalysts for O2 Reduction. *Electrochimica Acta* **1984**, *29* (11), 1527–1537. https://doi.org/10.1016/0013-4686(84)85006-9.

(36) Dong, J.-C.; Zhang, X.-G.; Briega-Martos, V.; Jin, X.; Yang, J.; Chen, S.; Yang, Z.-L.; Wu, D.-Y.; Feliu, J. M.; Williams, C. T.; Tian, Z.-Q.; Li, J.-F. In Situ Raman Spectroscopic Evidence for Oxygen Reduction Reaction Intermediates at Platinum Single-Crystal Surfaces. *Nat Energy* **2018**, *4* (1), 60–67. https://doi.org/10.1038/s41560-018-0292-z.

(37) Noël, J.-M.; Latus, A.; Lagrost, C.; Volanschi, E.; Hapiot, P. Evidence for OH Radical Production during Electrocatalysis of Oxygen Reduction on Pt Surfaces: Consequences and Application. *J. Am. Chem. Soc.* **2012**, *134* (5), 2835–2841. https://doi.org/10.1021/ja211663t.

(38) Goellner, V.; Armel, V.; Zitolo, A.; Fonda, E.; Jaouen, F. Degradation by Hydrogen Peroxide of Metal-Nitrogen-Carbon Catalysts for Oxygen Reduction. *J. Electrochem. Soc.* **2015**, *162* (6), H403–H414. https://doi.org/10.1149/2.1091506jes.

(39) Xie, X.; He, C.; Li, B.; He, Y.; Cullen, D. A.; Wegener, E. C.; Kropf, A. J.; Martinez, U.; Cheng, Y.; Engelhard, M. H.; Bowden, M. E.; Song, M.; Lemmon, T.; Li, X. S.; Nie, Z.; Liu, J.; Myers, D. J.; Zelenay, P.; Wang, G.; Wu, G.; Ramani, V.; Shao, Y. Performance Enhancement and Degradation Mechanism Identification of a Single-Atom Co–N–C Catalyst for Proton Exchange Membrane Fuel Cells. *Nat Catal* **2020**, *3* (12), 1044–1054. https://doi.org/10.1038/s41929-020-00546-1.

(40) Hamal, K.; May, J.; Koirala, D.; Zhu, H.; Kabir, H.; Echeverria, E.; McIlroy, D. N.; Nicholas, N.; Cheng, I. F. Highly Stable, Low-Cost Metal-Free Oxygen Reduction Reaction Electrocatalyst Based on Nitrogen-Doped Pseudo-Graphite. *Energy Fuels* **2021**, *35* (12), 10146–10155. https://doi.org/10.1021/acs.energyfuels.1c00658.

(41) Chen, W.; Huang, J.; Wei, J.; Zhou, D.; Cai, J.; He, Z.-D.; Chen, Y.-X. Origins of High Onset Overpotential of Oxygen Reduction Reaction at Pt-Based Electrocatalysts: A Mini Review. *Electrochemistry Communications* **2018**, *96*, 71–76. https://doi.org/10.1016/j.elecom.2018.09.011.

(42) Shao, M.; Liu, P.; Zhang, J.; Adzic, R. Origin of Enhanced Activity in Palladium Alloy Electrocatalysts for Oxygen Reduction Reaction †. *The Journal of Physical Chemistry B* **2007**, *111* (24), 6772–6775. https://doi.org/10.1021/jp0689971.

(43) Asset, T.; Chattot, R.; Fontana, M.; Mercier-Guyon, B.; Job, N.; Dubau, L.; Maillard, F. A Review on Recent Developments and Prospects for the Oxygen Reduction Reaction on Hollow Pt-Alloy Nanoparticles. *ChemPhysChem* **2018**, *19* (13), 1552–1567. https://doi.org/10.1002/cphc.201800153.

(44) Li, Y.; Li, Q.; Wang, H.; Zhang, L.; Wilkinson, D. P.; Zhang, J. Recent Progresses in Oxygen Reduction Reaction Electrocatalysts for Electrochemical Energy Applications. *Electrochem. Energ. Rev.* **2019**, *2* (4), 518–538. https://doi.org/10.1007/s41918-019-00052-4.

(45) Anantharaj, S.; Karthik, P. E.; Noda, S. The Significance of Properly Reporting Turnover Frequency in Electrocatalysis Research. *Angew Chem Int Ed* **2021**, *60* (43), 23051–23067. https://doi.org/10.1002/anie.202110352.

(46) Li, J.; Yin, H.-M.; Li, X.-B.; Okunishi, E.; Shen, Y.-L.; He, J.; Tang, Z.-K.; Wang, W.-X.; Yücelen, E.; Li, C.; Gong, Y.; Gu, L.; Miao, S.; Liu, L.-M.; Luo, J.; Ding, Y. Surface Evolution of a Pt–Pd–Au Electrocatalyst for Stable Oxygen Reduction. *Nat Energy* **2017**, *2* (8), 17111. https://doi.org/10.1038/nenergy.2017.111.

(47) Ma, R.; Lin, G.; Zhou, Y.; Liu, Q.; Zhang, T.; Shan, G.; Yang, M.; Wang, J. A Review of Oxygen Reduction Mechanisms for Metal-Free Carbon-Based Electrocatalysts. *npj Comput Mater* **2019**, *5* (1), 78. https://doi.org/10.1038/s41524-019-0210-3.

(48) Taylor, S.; Fabbri, E.; Levecque, P.; Schmidt, T. J.; Conrad, O. The Effect of Platinum Loading and Surface Morphology on Oxygen Reduction Activity. *Electrocatalysis* **2016**, *7* (4), 287–296. https://doi.org/10.1007/s12678-016-0304-3.

(49) Kongkanand, A.; Mathias, M. F. The Priority and Challenge of High-Power Performance of Low-Platinum Proton-Exchange Membrane Fuel Cells. *J. Phys. Chem. Lett.* **2016**, *7* (7), 1127–1137. https://doi.org/10.1021/acs.jpclett.6b00216.

(50) Nørskov, J. K.; Rossmeisl, J.; Logadottir, A.; Lindqvist, L.; Kitchin, J. R.; Bligaard, T.; Jónsson, H. Origin of the Overpotential for Oxygen Reduction at a Fuel-Cell Cathode. *J. Phys. Chem. B* **2004**, *108* (46), 17886–17892. https://doi.org/10.1021/jp047349j.

(51) Cheng, F.; Chen, J. Metal–Air Batteries: From Oxygen Reduction Electrochemistry to Cathode Catalysts. *Chem. Soc. Rev.* **2012**, *41* (6), 2172. https://doi.org/10.1039/c1cs15228a.

(52) Xu, J.; Gao, P.; Zhao, T. S. Non-Precious Co3O4 Nano-Rod Electrocatalyst for Oxygenreduction Reaction in Anion-Exchange Membranefuelcells. *Energy Environ. Sci.* **2012**, *5* (1), 5333–5339. https://doi.org/10.1039/C1EE01431E.

(53) Li, Y.; Li, Q.; Wang, H.; Zhang, L.; Wilkinson, D. P.; Zhang, J. Recent Progresses in Oxygen Reduction Reaction Electrocatalysts for Electrochemical Energy Applications. *Electrochem. Energ. Rev.* **2019**, *2* (4), 518–538. https://doi.org/10.1007/s41918-019-00052-4.

(54) Zeng, Z.; Zhang, W.; Liu, Y.; Lu, P.; Wei, J. Uniformly Electrodeposited α-MnO2 Film on Super-Aligned Electrospun Carbon Nanofibers for a Bifunctional Catalyst Design in Oxygen Reduction Reaction. *Electrochimica Acta* **2017**, *256*, 232–240. https://doi.org/10.1016/j.electacta.2017.10.057.

(55) Shahid, M. M.; Rameshkumar, P.; Basirun, W. J.; Juan, J. C.; Huang, N. M. Cobalt Oxide Nanocubes Interleaved Reduced Graphene Oxide as an Efficient Electrocatalyst for Oxygen Reduction Reaction in Alkaline Medium. *Electrochimica Acta* **2017**, *237*, 61–68. https://doi.org/10.1016/j.electacta.2017.03.088.

(56) Ryabova, A. S.; Bonnefont, A.; Simonov, P. A.; Dintzer, T.; Ulhaq-Bouillet, C.; Bogdanova, Y. G.; Tsirlina, G. A.; Savinova, E. R. Further Insights into the Role of Carbon in Manganese Oxide/Carbon Composites in the Oxygen Reduction Reaction in Alkaline Media. *Electrochimica Acta* **2017**, *246*, 643–653. https://doi.org/10.1016/j.electacta.2017.06.017.

(57) Zhu, Y.; Lin, Q.; Zhong, Y.; Tahini, H. A.; Shao, Z.; Wang, H. Metal Oxide-Based Materials as an Emerging Family of Hydrogen Evolution Electrocatalysts. *Energy Environ. Sci.* **2020**, *13* (10), 3361–3392. https://doi.org/10.1039/D0EE02485F.

(58) Li, Y.; Li, Q.; Wang, H.; Zhang, L.; Wilkinson, D. P.; Zhang, J. Recent Progresses in Oxygen Reduction Reaction Electrocatalysts for Electrochemical Energy Applications. *Electrochem. Energ. Rev.* **2019**, *2* (4), 518–538. https://doi.org/10.1007/s41918-019-00052-4.

(59) Huang, Z.-F.; Wang, J.; Peng, Y.; Jung, C.-Y.; Fisher, A.; Wang, X. Design of Efficient Bifunctional Oxygen Reduction/Evolution Electrocatalyst: Recent Advances and Perspectives. *Adv. Energy Mater.* **2017**, *7* (23), 1700544. https://doi.org/10.1002/aenm.201700544.

(60) Woo, J.; Lim, J. S.; Kim, J. H.; Joo, S. H. Heteroatom-Doped Carbon-Based Oxygen Reduction Electrocatalysts with Tailored Four-Electron and Two-Electron Selectivity. *Chem. Commun.* **2021**, *57* (60), 7350–7361. https://doi.org/10.1039/D1CC02667D.

(61) Ni, S.; Li, Z.; Yang, J. Oxygen Molecule Dissociation on Carbon Nanostructures with Different Types of Nitrogen Doping. *Nanoscale* **2012**, *4* (4), 1184–1189. https://doi.org/10.1039/C1NR11086A.

(62) Shi, Z.; Zhang, J.; Liu, Z.-S.; Wang, H.; Wilkinson, D. P. Current Status of Ab Initio Quantum Chemistry Study for Oxygen Electroreduction on Fuel Cell Catalysts. *Electrochimica Acta* **2006**, *51* (10), 1905–1916. https://doi.org/10.1016/j.electacta.2005.07.006.

(63) Zhang, L.; Xiao, J.; Wang, H.; Shao, M. Carbon-Based Electrocatalysts for Hydrogen and Oxygen Evolution Reactions. *ACS Catal.* **2017**, *7* (11), 7855–7865. https://doi.org/10.1021/acscatal.7b02718.

(64) Zheng, Y.; Jiao, Y.; Jaroniec, M.; Jin, Y.; Qiao, S. Z. Nanostructured Metal-Free Electrochemical Catalysts for Highly Efficient Oxygen Reduction. *Small* **2012**, *8* (23), 3550–3566. https://doi.org/10.1002/smll.201200861.

(65) Limani, N.; Marques, I. S.; Jarrais, B.; Fernandes, A. J. S.; Freire, C.; Fernandes, D. M. Cobalt Phosphotungstate-Based Composites as Bifunctional Electrocatalysts for Oxygen Reactions. *Catalysts* **2022**, *12* (4), 357. https://doi.org/10.3390/catal12040357.

(66) Luo, Z.; Lim, S.; Tian, Z.; Shang, J.; Lai, L.; MacDonald, B.; Fu, C.; Shen, Z.; Yu, T.; Lin, J. Pyridinic N Doped Graphene: Synthesis, Electronic Structure, and Electrocatalytic Property. *Journal of Materials Chemistry* **2011**, *21* (22), 8038. https://doi.org/10.1039/c1jm10845j.

(67) Ge, X.; Sumboja, A.; Wuu, D.; An, T.; Li, B.; Goh, F. W. T.; Hor, T. S. A.; Zong, Y.; Liu, Z. Oxygen Reduction in Alkaline Media: From Mechanisms to Recent Advances of Catalysts. *ACS Catal.* **2015**, *5* (8), 4643–4667. https://doi.org/10.1021/acscatal.5b00524.

(68) Liu, S.; Li, C.; Zachman, M. J.; Zeng, Y.; Yu, H.; Li, B.; Wang, M.; Braaten, J.; Liu, J.; Meyer, H. M.; Lucero, M.; Kropf, A. J.; Alp, E. E.; Gong, Q.; Shi, Q.; Feng, Z.; Xu, H.; Wang, G.; Myers, D. J.; Xie, J.; Cullen, D. A.; Litster, S.; Wu, G. Atomically Dispersed Iron Sites with a Nitrogen–Carbon Coating as Highly Active and Durable Oxygen Reduction Catalysts for Fuel Cells. *Nat Energy* **2022**, *7* (7), 652–663. https://doi.org/10.1038/s41560-022-01062-1.

(69) Chung, H. T.; Won, J. H.; Zelenay, P. Active and Stable Carbon Nanotube/Nanoparticle Composite Electrocatalyst for Oxygen Reduction. *Nat Commun* **2013**, *4* (1), 1922. https://doi.org/10.1038/ncomms2944.

(70) Deng, D.; Yu, L.; Chen, X.; Wang, G.; Jin, L.; Pan, X.; Deng, J.; Sun, G.; Bao, X. Iron Encapsulated within Pod-like Carbon Nanotubes for Oxygen Reduction Reaction. *Angew. Chem. Int. Ed.* **2013**, *52* (1), 371–375. https://doi.org/10.1002/anie.201204958.

(71) Liu, J.; Li, E.; Ruan, M.; Song, P.; Xu, W. Recent Progress on Fe/N/C Electrocatalysts for the Oxygen Reduction Reaction in Fuel Cells. *Catalysts* **2015**, *5* (3), 1167–1192. https://doi.org/10.3390/catal5031167.

(72) Kramm, U. I.; Lefèvre, M.; Larouche, N.; Schmeisser, D.; Dodelet, J.-P. Correlations between Mass Activity and Physicochemical Properties of Fe/N/C Catalysts for the ORR in PEM Fuel Cell via ^{57}Fe Mössbauer Spectroscopy and Other Techniques. *J. Am. Chem. Soc.* **2014**, *136* (3), 978–985. https://doi.org/10.1021/ja410076f.

(73) Charreteur, F.; Jaouen, F.; Ruggeri, S.; Dodelet, J.-P. Fe/N/C Non-Precious Catalysts for PEM Fuel Cells: Influence of the Structural Parameters of Pristine Commercial Carbon Blacks on Their Activity for Oxygen Reduction. *Electrochimica Acta* **2008**, *53* (6), 2925–2938. https://doi.org/10.1016/j.electacta.2007.11.002.

(74) Shen, H.; Thomas, T.; Rasaki, S. A.; Saad, A.; Hu, C.; Wang, J.; Yang, M. Oxygen Reduction Reactions of Fe-N-C Catalysts: Current Status and the Way Forward. *Electrochem. Energ. Rev.* **2019**, *2* (2), 252–276. https://doi.org/10.1007/s41918-019-00030-w.

(75) Marshall-Roth, T.; Libretto, N. J.; Wrobel, A. T.; Anderton, K. J.; Pegis, M. L.; Ricke, N. D.; Voorhis, T. V.; Miller, J. T.; Surendranath, Y. A Pyridinic Fe-N4 Macrocycle Models the Active Sites in Fe/N-Doped Carbon Electrocatalysts. *Nat Commun* **2020**, *11* (1), 5283. https://doi.org/10.1038/s41467-020-18969-6.

(76) Xia, D.; Yang, X.; Xie, L.; Wei, Y.; Jiang, W.; Dou, M.; Li, X.; Li, J.; Gan, L.; Kang, F. Direct Growth of Carbon Nanotubes Doped with Single Atomic Fe–N $_4$ Active Sites and Neighboring Graphitic Nitrogen for Efficient and Stable Oxygen Reduction Electrocatalysis. *Adv. Funct. Mater.* **2019**, *29* (49), 1906174. https://doi.org/10.1002/adfm.201906174.

(77) Luo, F.; Choi, C. H.; Primbs, M. J. M.; Ju, W.; Li, S.; Leonard, N. D.; Thomas, A.; Jaouen, F.; Strasser, P. Accurate Evaluation of Active-Site Density (SD) and Turnover Frequency (TOF) of PGM-Free Metal–Nitrogen-Doped Carbon (MNC) Electrocatalysts Using CO Cryo Adsorption. *ACS Catal.* **2019**, *9* (6), 4841–4852. https://doi.org/10.1021/acscatal.9b00588.

(78) Li, J.; Jaouen, F. Structure and Activity of Metal-Centered Coordination Sites in Pyrolyzed Metal–Nitrogen–Carbon Catalysts for the Electrochemical Reduction of O2. *Current Opinion in Electrochemistry* **2018**, *9*, 198–206. https://doi.org/10.1016/j.coelec.2018.03.039.

(79) Kumar, K.; Dubau, L.; Mermoux, M.; Li, J.; Zitolo, A.; Nelayah, J.; Jaouen, F.; Maillard, F. On the Influence of Oxygen on the Degradation of Fe-N-C Catalysts. *Angew. Chem.* **2020**, *132* (8), 3261–3269. https://doi.org/10.1002/ange.201912451.

(80) Du, C.; Tan, Q.; Yin, G.; Zhang, J. Rotating Disk Electrode Method. In *Rotating Electrode Methods and Oxygen Reduction Electrocatalysts*; Elsevier, 2014; pp 171–198. https://doi.org/10.1016/B978-0-444-63278-4.00005-7.

(81) Sun, K.; Xu, W.; Lin, X.; Tian, S.; Lin, W.; Zhou, D.; Sun, X. Electrochemical Oxygen Reduction to Hydrogen Peroxide via a Two-Electron Transfer Pathway on Carbon-Based Single-Atom Catalysts. *Adv. Mater. Interfaces* **2021**, *8* (8), 2001360. https://doi.org/10.1002/admi.202001360.

(82) Dickinson, E. J. F.; Wain, A. J. The Butler-Volmer Equation in Electrochemical Theory: Origins, Value, and Practical Application. *Journal of Electroanalytical Chemistry* **2020**, *872*, 114145. https://doi.org/10.1016/j.jelechem.2020.114145.

(83) Ikeshoji, T.; Otani, M. Toward Full Simulation of the Electrochemical Oxygen Reduction Reaction on Pt Using First-Principles and Kinetic Calculations. *Phys. Chem. Chem. Phys.* **2017**, *19* (6), 4447–4453. https://doi.org/10.1039/C6CP08466D.

(84) Dong, Q.; Santhanagopalan, S.; White, R. E. Simulation of the Oxygen Reduction Reaction at an RDE in 0.5 M H[Sub 2]SO[Sub 4] Including an Adsorption Mechanism. *J. Electrochem. Soc.* **2007**, *154* (9), A888. https://doi.org/10.1149/1.2756994.

(85) Orellana, W.; Loyola, C. Z.; Marco, J. F.; Tasca, F. Evidence of Carbon-Supported Porphyrins Pyrolyzed for the Oxygen Reduction Reaction Keeping Integrity. *Sci Rep* **2022**, *12* (1), 8072. https://doi.org/10.1038/s41598-022-11820-6.

(86) Wang, T.; Zhang, Y.; Huang, B.; Cai, B.; Rao, R. R.; Giordano, L.; Sun, S.-G.; Shao-Horn, Y. Enhancing Oxygen Reduction Electrocatalysis by Tuning Interfacial Hydrogen Bonds. *Nat Catal* **2021**, *4* (9), 753–762. https://doi.org/10.1038/s41929-021-00668-0.

(87) Zhou, R.; Zheng, Y.; Jaroniec, M.; Qiao, S.-Z. Determination of the Electron Transfer Number for the Oxygen Reduction Reaction: From Theory to Experiment. *ACS Catalysis* **2016**, *6* (7), 4720–4728. https://doi.org/10.1021/acscatal.6b01581.

(88) Jia, Z.; Yin, G.; Zhang, J. Rotating Ring-Disk Electrode Method. In *Rotating Electrode Methods and Oxygen Reduction Electrocatalysts*; Elsevier, 2014; pp 199–229. https://doi.org/10.1016/B978-0-444-63278-4.00006-9.

(89) *Rotating Electrode Methods and Oxygen Reduction Electrocatalysts*; Xing, W., Yin, G., Zhang, J., Eds.; Elsevier: Amsterdam, 2014.

(90) Zoski, C. G. Review—Advances in Scanning Electrochemical Microscopy (SECM). *Journal of The Electrochemical Society* **2016**, *163* (4), H3088–H3100. https://doi.org/10.1149/2.0141604jes.

(91) Cornut, R.; Lefrou, C. A Unified New Analytical Approximation for Negative Feedback Currents with a Microdisk SECM Tip. *Journal of Electroanalytical Chemistry* **2007**, *608* (1), 59–66. https://doi.org/10.1016/j.jelechem.2007.05.007.

(92) Lai, S. C. S.; Macpherson, J. V.; Unwin, P. R. *In Situ* Scanning Electrochemical Probe Microscopy for Energy Applications. *MRS Bulletin* **2012**, *37* (7), 668–674. https://doi.org/10.1557/mrs.2012.146.

(93) *Scanning Electrochemical Microscopy*, 2. ed.; Bard, A. J., Mirkin, M. V., Eds.; CRC Press: Boca Raton, Fla, 2012.

(94) Cornut, R.; Mayoral, M.; Fabre, D.; Mauzeroll, J. Scanning Electrochemical Microscopy Approach Curves for Ring Microelectrodes in Pure Negative and Positive Feedback Mode. *Journal of The Electrochemical Society* **2010**, *157* (7), F77. https://doi.org/10.1149/1.3374340.

(95) Cornut, R.; Poirier, S.; Mauzeroll, J. Forced Convection during Feedback Approach Curve Measurements in Scanning Electrochemical Microscopy: Maximal Displacement Velocity with a Microdisk. *Analytical Chemistry* **2012**, *84* (8), 3531–3537. https://doi.org/10.1021/ac203047d.

(96) Bard, A. J.; Fan, F. R. F.; Kwak, Juhyoun.; Lev, Ovadia. Scanning Electrochemical Microscopy. Introduction and Principles. *Analytical Chemistry* **1989**, *61* (2), 132–138. https://doi.org/10.1021/ac00177a011.

(97) Payne, N. A.; Stephens, L. I.; Mauzeroll, J. The Application of Scanning Electrochemical Microscopy to Corrosion Research. *CORROSION* **2017**, *73* (7), 759–780. https://doi.org/10.5006/2354.

(98) Bergner, S.; Vatsyayan, P.; Matysik, F.-M. Recent Advances in High Resolution Scanning Electrochemical Microscopy of Living Cells – A Review. *Analytica Chimica Acta* **2013**, *775*, 1–13. https://doi.org/10.1016/j.aca.2012.12.042.

(99) Kai, T.; Zoski, C. G.; Bard, A. J. Scanning Electrochemical Microscopy at the Nanometer Level. *Chem. Commun.* **2018**, *54* (16), 1934–1947. https://doi.org/10.1039/C7CC09777H.

(100) Amemiya, S.; Bard, A. J.; Fan, F.-R. F.; Mirkin, M. V.; Unwin, P. R. Scanning Electrochemical Microscopy. *Annual Review of Analytical Chemistry* **2008**, *1* (1), 95–131. https://doi.org/10.1146/annurev.anchem.1.031207.112938.

(101) *Recent Developments in Analytical Techniques for Corrosion Research*; Toor, I. ulhaq, Ed.; Springer International Publishing: Cham, 2022. https://doi.org/10.1007/978-3-030-89101-5.

(102) Heinze, J. Ultramicroelectrodes in Electrochemistry. *Angewandte Chemie International Edition in English* **1993**, *32* (9), 1268–1288. https://doi.org/10.1002/anie.199312681.

(103) Senthamarai, R.; Rajendran, L. A COMPARISON OF DIFFUSION-LIMITED CURRENT AT MICROELECTRODES OF VARIOUS GEOMETRIES. *Journal of Theoretical and Computational Chemistry* **2008**, *07* (02), 205–219. https://doi.org/10.1142/S0219633608003721.

(104) Walsh, D. A.; Lovelock, K. R. J.; Licence, P. Ultramicroelectrode Voltammetry and Scanning Electrochemical Microscopy in Room-Temperature Ionic Liquid Electrolytes. *Chem. Soc. Rev.* **2010**, *39* (11), 4185. https://doi.org/10.1039/b822846a.

(105) Hijazi, I.; Bourgeteau, T.; Cornut, R.; Morozan, A.; Filoramo, A.; Leroy, J.; Derycke, V.; Jousselme, B.; Campidelli, S. Carbon Nanotube-Templated Synthesis of Covalent Porphyrin Network for Oxygen Reduction Reaction. *Journal of the American Chemical Society* **2014**, *136* (17), 6348–6354. https://doi.org/10.1021/ja500984k.

(106) Eckhard, K.; Chen, X.; Turcu, F.; Schuhmann, W. Redox Competition Mode of Scanning Electrochemical Microscopy (RC-SECM) for Visualisation of Local Catalytic Activity. *Physical Chemistry Chemical Physics* **2006**, *8* (45), 5359. https://doi.org/10.1039/b609511a.

(107) Sánchez-Sánchez, C. M.; Solla-Gullón, J.; Vidal-Iglesias, F. J.; Aldaz, A.; Montiel, V.; Herrero, E. Imaging Structure Sensitive Catalysis on Different Shape-Controlled Platinum Nanoparticles. *J. Am. Chem. Soc.* **2010**, *132* (16), 5622–5624. https://doi.org/10.1021/ja100922h.

(108) Fernández, J. L.; Walsh, D. A.; Bard, A. J. Thermodynamic Guidelines for the Design of Bimetallic Catalysts for Oxygen Electroreduction and Rapid Screening by Scanning Electrochemical Microscopy. M−Co (M: Pd, Ag, Au). *J. Am. Chem. Soc.* **2005**, *127* (1), 357–365. https://doi.org/10.1021/ja0449729.

(109) Venegas, R.; Muñoz-Becerra, K.; Juillard, S.; Zhang, L.; Oñate, R.; Ponce, I.; Vivier, V.; Recio, F. J.; Sánchez-Sánchez, C. M. Proving Ligand Structure-Reactivity Correlation on Multinuclear Copper Electrocatalysts Supported on Carbon Black for the Oxygen Reduction Reaction. *Electrochimica Acta* **2022**, *434*, 141304. https://doi.org/10.1016/j.electacta.2022.141304.

(110) Perales-Rondón, J. V.; Herrero, E.; Solla-Gullón, J.; Sánchez-Sánchez, C. M.; Vivier, V. Oxygen Crossover Effect on Palladium and Platinum Based Electrocatalysts during Formic Acid Oxidation Studied by Scanning Electrochemical Microscopy. *Journal of Electroanalytical Chemistry* **2017**, *793*, 218–225. https://doi.org/10.1016/j.jelechem.2016.12.049.

(111) Lin, C.-L.; Rodríguez-López, J.; Bard, A. J. Micropipet Delivery−Substrate Collection Mode of Scanning Electrochemical Microscopy for the Imaging of Electrochemical Reactions and the Screening of Methanol Oxidation Electrocatalysts. *Anal. Chem.* **2009**, *81* (21), 8868–8877. https://doi.org/10.1021/ac901434a.

(112) Kucernak, A. R.; Chowdhury, P. B.; Wilde, C. P.; Kelsall, G. H.; Zhu, Y. Y.; Williams, D. E. Scanning Electrochemical Microscopy of a Fuel-Cell Electrocatalyst Deposited onto Highly Oriented Pyrolytic Graphite. *Electrochimica Acta* **2000**, *45* (27), 4483–4491. https://doi.org/10.1016/S0013-4686(00)00504-1.

(113) Shen, Y.; Träuble, M.; Wittstock, G. Detection of Hydrogen Peroxide Produced during Electrochemical Oxygen Reduction Using Scanning Electrochemical Microscopy. *Anal. Chem.* **2008**, *80* (3), 750–759. https://doi.org/10.1021/ac0711889.

(114) Dobrzeniecka, A.; Zeradjanin, A. R.; Masa, J.; Blicharska, M.; Wintrich, D.; Kulesza, P. J.; Schuhmann, W. Evaluation of Kinetic Constants on Porous, Non-Noble Catalyst Layers for Oxygen Reduction—A Comparative Study between SECM and Hydrodynamic Methods. *Catalysis Today* **2016**, *262*, 74–81. https://doi.org/10.1016/j.cattod.2015.07.043.

(115) Dobrzeniecka, A.; Zeradjanin, A.; Masa, J.; Puschhof, A.; Stroka, J.; Kulesza, P. J.; Schuhmann, W. Application of SECM in Tracing of Hydrogen Peroxide at Multicomponent Non-Noble Electrocatalyst Films for the Oxygen Reduction Reaction. *Catalysis Today* **2013**, *202*, 55–62. https://doi.org/10.1016/j.cattod.2012.03.060.

(116) Sánchez-Sánchez, C. M.; Rodríguez-López, J.; Bard, A. J. Scanning Electrochemical Microscopy. 60. Quantitative Calibration of the SECM Substrate Generation/Tip Collection Mode and Its Use for the Study of the Oxygen Reduction Mechanism. *Anal. Chem.* **2008**, *80* (9), 3254–3260. https://doi.org/10.1021/ac702453n.

(117) Sánchez-Sánchez, C. M.; Bard, A. J. Hydrogen Peroxide Production in the Oxygen Reduction Reaction at Different Electrocatalysts as Quantified by Scanning Electrochemical Microscopy. *Anal. Chem.* **2009**, *81* (19), 8094–8100. https://doi.org/10.1021/ac901291v.

(118) Schuhmann, W.; Bron, M. Scanning Electrochemical Microscopy (SECM) in Proton Exchange Membrane Fuel Cell Research and Development. In *Polymer Electrolyte Membrane and Direct Methanol Fuel Cell Technology*; Elsevier, 2012; pp 399–424. https://doi.org/10.1533/9780857095480.3.399.

(119) Ebejer, N.; Güell, A. G.; Lai, S. C. S.; McKelvey, K.; Snowden, M. E.; Unwin, P. R. Scanning Electrochemical Cell Microscopy: A Versatile Technique for Nanoscale Electrochemistry and

Functional Imaging. *Annual Rev. Anal. Chem.* **2013**, *6* (1), 329–351. https://doi.org/10.1146/annurev-anchem-062012-092650.

(120) Ebejer, N.; Güell, A. G.; Lai, S. C. S.; McKelvey, K.; Snowden, M. E.; Unwin, P. R. Scanning Electrochemical Cell Microscopy: A Versatile Technique for Nanoscale Electrochemistry and Functional Imaging. *Annual Review of Analytical Chemistry* **2013**, *6* (1), 329–351. https://doi.org/10.1146/annurev-anchem-062012-092650.

(121) Chen, C.-C.; Zhou, Y.; Baker, L. A. Scanning Ion Conductance Microscopy. *Annual Rev. Anal. Chem.* **2012**, *5* (1), 207–228. https://doi.org/10.1146/annurev-anchem-062011-143203.

(122) Chen, C.-H.; Meadows, K. E.; Cuharuc, A.; Lai, S. C. S.; Unwin, P. R. High Resolution Mapping of Oxygen Reduction Reaction Kinetics at Polycrystalline Platinum Electrodes. *Phys. Chem. Chem. Phys.* **2014**, *16* (34), 18545. https://doi.org/10.1039/C4CP01511H.

(123) Tetteh, E. B.; Banko, L.; Krysiak, O. A.; Löffler, T.; Xiao, B.; Varhade, S.; Schumacher, S.; Savan, A.; Andronescu, C.; Ludwig, A.; Schuhmann, W. Zooming-in – Visualization of Active Site Heterogeneity in High Entropy Alloy Electrocatalysts Using Scanning Electrochemical Cell Microscopy. *Electrochemical Science Adv* **2022**, *2* (3). https://doi.org/10.1002/elsa.202100105.

(124) Byers, J. C.; Güell, A. G.; Unwin, P. R. Nanoscale Electrocatalysis: Visualizing Oxygen Reduction at Pristine, Kinked, and Oxidized Sites on Individual Carbon Nanotubes. *J. Am. Chem. Soc.* **2014**, *136* (32), 11252–11255. https://doi.org/10.1021/ja505708y.

(125) Katemann, B. B.; Schuhmann, W. Fabrication and Characterization of Needle-Type. *Electroanalysis* **2002**, *14* (1), 22–28. https://doi.org/10.1002/1521-4109(200201)14:1<22::AID-ELAN22>3.0.CO;2-F.

(126) Momotenko, D.; Byers, J. C.; McKelvey, K.; Kang, M.; Unwin, P. R. High-Speed Electrochemical Imaging. *ACS Nano* **2015**, *9* (9), 8942–8952. https://doi.org/10.1021/acsnano.5b02792.

(127) Toca-Herrera, J. L. Atomic Force Microscopy Meets Biophysics, Bioengineering, Chemistry and Materials Science. *ChemSusChem* **2018**, cssc.201802383. https://doi.org/10.1002/cssc.201802383.

(128) Haugstad, G. *Atomic Force Microscopy: Understanding Basic Modes and Advanced Applications*; Wiley, 2012.

(129) Jagoba Iturri; José Toca-Herrera. Characterization of Cell Scaffolds by Atomic Force Microscopy. *Polymers* **2017**, *9* (12), 383. https://doi.org/10.3390/polym9080383.

(130) Upputuri, P. K.; Pramanik, M. Microsphere-Aided Optical Microscopy and Its Applications for Super-Resolution Imaging. *Optics Communications* **2017**, *404*, 32–41. https://doi.org/10.1016/j.optcom.2017.05.049.

(131) Xu, F.; Zhang, H.; Ho, D.; Ilavsky, J.; Justics, M.; Petrache, H.; Stanciu, L.; Xie, J. Investigation of the Interaction of Nafion Ionomer and Carbon Black Using Small Angle X-Ray and Small Angle Neutron Scattering. *ECS Trans.* **2011**, *41* (1), 637–645. https://doi.org/10.1149/1.3635597.

(132) Zamel, N. The Catalyst Layer and Its Dimensionality – A Look into Its Ingredients and How to Characterize Their Effects. *Journal of Power Sources* **2016**, *309*, 141–159. https://doi.org/10.1016/j.jpowsour.2016.01.091.

(133) Klein, T.; Buhr, E.; Georg Frase, C. TSEM. In *Advances in Imaging and Electron Physics*; Elsevier, 2012; Vol. 171, pp 297–356. https://doi.org/10.1016/B978-0-12-394297-5.00006-4.

(134) Li, Y.; Zhou, W.; Wang, H.; Xie, L.; Liang, Y.; Wei, F.; Idrobo, J.-C.; Pennycook, S. J.; Dai, H. An Oxygen Reduction Electrocatalyst Based on Carbon Nanotube–Graphene Complexes. *Nature Nanotech* **2012**, *7* (6), 394–400. https://doi.org/10.1038/nnano.2012.72.

(135) Masa, J.; Batchelor-McAuley, C.; Schuhmann, W.; Compton, R. G. Koutecky-Levich Analysis Applied to Nanoparticle Modified Rotating Disk Electrodes: Electrocatalysis or Misinterpretation. *Nano Res.* **2014**, *7* (1), 71–78. https://doi.org/10.1007/s12274-013-0372-0.

(136) Garsany, Y.; Baturina, O. A.; Swider-Lyons, K. E.; Kocha, S. S. Experimental Methods for Quantifying the Activity of Platinum Electrocatalysts for the Oxygen Reduction Reaction. *Anal. Chem.* **2010**, *82* (15), 6321–6328. https://doi.org/10.1021/ac100306c.

(137) Liu, J.; Cunning, B. V.; Daio, T.; Mufundirwa, A.; Sasaki, K.; Lyth, S. M. Nitrogen-Doped Carbon Foam as a Highly Durable Metal-Free Electrocatalyst for the Oxygen Reduction Reaction in Alkaline Solution. *Electrochimica Acta* **2016**, *220*, 554–561. https://doi.org/10.1016/j.electacta.2016.10.090.

(138) Bonakdarpour, A.; Lefevre, M.; Yang, R.; Jaouen, F.; Dahn, T.; Dodelet, J.-P.; Dahn, J. R. Impact of Loading in RRDE Experiments on Fe–N–C Catalysts: Two- or Four-Electron Oxygen Reduction? *Electrochem. Solid-State Lett.* **2008**, *11* (6), B105. https://doi.org/10.1149/1.2904768.

(139) Garsany, Y.; Ge, J.; St-Pierre, J.; Rocheleau, R.; Swider-Lyons, K. E. Analytical Procedure for Accurate Comparison of Rotating Disk Electrode Results for the Oxygen Reduction Activity of Pt/C. *J. Electrochem. Soc.* **2014**, *161* (5), F628–F640. https://doi.org/10.1149/2.036405jes.

(140) Al-Hamadani, Y. A. J.; Chu, K. H.; Son, A.; Heo, J.; Her, N.; Jang, M.; Park, C. M.; Yoon, Y. Stabilization and Dispersion of Carbon Nanomaterials in Aqueous Solutions: A Review. *Separation and Purification Technology* **2015**, *156*, 861–874. https://doi.org/10.1016/j.seppur.2015.11.002.

(141) Yu, H.; Hermann, S.; Schulz, S. E.; Gessner, T.; Dong, Z.; Li, W. J. Optimizing Sonication Parameters for Dispersion of Single-Walled Carbon Nanotubes. *Chemical Physics* **2012**, *408*, 11–16. https://doi.org/10.1016/j.chemphys.2012.08.020.

(142) Ma, P.-C.; Siddiqui, N. A.; Marom, G.; Kim, J.-K. Dispersion and Functionalization of Carbon Nanotubes for Polymer-Based Nanocomposites: A Review. *Composites Part A: Applied Science and Manufacturing* **2010**, *41* (10), 1345–1367. https://doi.org/10.1016/j.compositesa.2010.07.003.

(143) Chen, S. J.; Zou, B.; Collins, F.; Zhao, X. L.; Majumber, M.; Duan, W. H. Predicting the Influence of Ultrasonication Energy on the Reinforcing Efficiency of Carbon Nanotubes. *Carbon* **2014**, *77*, 1–10. https://doi.org/10.1016/j.carbon.2014.04.023.

(144) Guangyin, Z.; Youcai, Z. Harvest of Bioenergy From Sewage Sludge by Anaerobic Digestion. In *Pollution Control and Resource Recovery*; Elsevier, 2017; pp 181–273. https://doi.org/10.1016/B978-0-12-811639-5.00005-X.

(145) Pollet, B. G. Let's Not Ignore the Ultrasonic Effects on the Preparation of Fuel Cell Materials. *Electrocatalysis* **2014**, *5* (4), 330–343. https://doi.org/10.1007/s12678-014-0211-4.

(146) Guo, Y.; Pan, F.; Chen, W.; Ding, Z.; Yang, D.; Li, B.; Ming, P.; Zhang, C. The Controllable Design of Catalyst Inks to Enhance PEMFC Performance: A Review. *Electrochem. Energ. Rev.* **2021**, *4* (1), 67–100. https://doi.org/10.1007/s41918-020-00083-2.

(147) Du, S.; Li, W.; Wu, H.; Abel Chuang, P.-Y.; Pan, M.; Sui, P.-C. Effects of Ionomer and Dispersion Methods on Rheological Behavior of Proton Exchange Membrane Fuel Cell Catalyst Layer Ink. *International Journal of Hydrogen Energy* **2020**, *45* (53), 29430–29441. https://doi.org/10.1016/j.ijhydene.2020.07.241.

(148) Ratso, S.; Zitolo, A.; Käärik, M.; Merisalu, M.; Kikas, A.; Kisand, V.; Rähn, M.; Paiste, P.; Leis, J.; Sammelselg, V.; Holdcroft, S.; Jaouen, F.; Tammeveski, K. Non-Precious Metal Cathodes for Anion Exchange Membrane Fuel Cells from Ball-Milled Iron and Nitrogen Doped Carbide-Derived Carbons. *Renewable Energy* **2021**, *167*, 800–810. https://doi.org/10.1016/j.renene.2020.11.154.

(149) Kuroki, H.; Onishi, K.; Asami, K.; Yamaguchi, T. Catalyst Slurry Preparation Using a Hydrodynamic Cavitation Dispersion Method for Polymer Electrolyte Fuel Cells. *Ind. Eng. Chem. Res.* **2019**, *58* (42), 19545–19550. https://doi.org/10.1021/acs.iecr.9b02111.

(150) Lyu, H.; Gao, B.; He, F.; Ding, C.; Tang, J.; Crittenden, J. C. Ball-Milled Carbon Nanomaterials for Energy and Environmental Applications. *ACS Sustainable Chem. Eng.* **2017**, *5* (11), 9568–9585. https://doi.org/10.1021/acssuschemeng.7b02170.

(151) Wang, M.; Park, J. H.; Kabir, S.; Neyerlin, K. C.; Kariuki, N. N.; Lv, H.; Stamenkovic, V. R.; Myers, D. J.; Ulsh, M.; Mauger, S. A. Impact of Catalyst Ink Dispersing Methodology on Fuel Cell Performance Using In-Situ X-Ray Scattering. *ACS Appl. Energy Mater.* **2019**, *2* (9), 6417–6427. https://doi.org/10.1021/acsaem.9b01037.

(152) Isse, A. A.; Gennaro, A. Absolute Potential of the Standard Hydrogen Electrode and the Problem of Interconversion of Potentials in Different Solvents. *J. Phys. Chem. B* **2010**, *114* (23), 7894–7899. https://doi.org/10.1021/jp100402x.

(153) Bonakdarpour, A.; Dahn, T. R.; Atanasoski, R. T.; Debe, M. K.; Dahn, J. R. H[Sub 2]O[Sub 2] Release during Oxygen Reduction Reaction on Pt Nanoparticles. *Electrochem. Solid-State Lett.* **2008**, *11* (11), B208. https://doi.org/10.1149/1.2978090.

(154) Bron, M.; Fiechter, S.; Bogdanoff, P.; Tributsch, H. Thermogravimetry/Mass Spectrometry Investigations on the Formation of Oxygen Reduction Catalysts for PEM Fuel Cells on the Basis of Heat-Treated Iron Phenanthroline Complexes. *Fuel Cells* **2002**, *2* (34), 137–142. https://doi.org/10.1002/fuce.200290012.

(155) Biddinger, E. J.; Deak, D. von; Singh, D.; Marsh, H.; Tan, B.; Knapke, D. S.; Ozkan, U. S. Examination of Catalyst Loading Effects on the Selectivity of CNx and Pt/VC ORR Catalysts Using RRDE. *J. Electrochem. Soc.* **2011**, *158* (4), B402. https://doi.org/10.1149/1.3552944.

(156) Zhang, G.; Wei, Q.; Yang, X.; Tavares, A. C.; Sun, S. RRDE Experiments on Noble-Metal and Noble-Metal-Free Catalysts: Impact of Loading on the Activity and Selectivity of Oxygen Reduction Reaction in Alkaline Solution. *Applied Catalysis B: Environmental* **2017**, *206*, 115–126. https://doi.org/10.1016/j.apcatb.2017.01.001.

(157) Cardoso, E. S. F.; Fortunato, G. V.; Maia, G. Use of Rotating Ring-Disk Electrodes to Investigate Graphene Nanoribbon Loadings for the Oxygen Reduction Reaction in Alkaline Medium. *ChemElectroChem* **2018**, *5* (13), 1691–1701. https://doi.org/10.1002/celc.201800331.

(158) Gabe, A.; Ruiz-Rosas, R.; González-Gaitán, C.; Morallón, E.; Cazorla-Amorós, D. Modeling of Oxygen Reduction Reaction in Porous Carbon Materials in Alkaline Medium. Effect of Microporosity. *Journal of Power Sources* **2019**, *412*, 451–464. https://doi.org/10.1016/j.jpowsour.2018.11.075.

(159) Inaba, M.; Yamada, H.; Tokunaga, J.; Tasaka, A. Effect of Agglomeration of Pt/C Catalyst on Hydrogen Peroxide Formation. *Electrochem. Solid-State Lett.* **2004**, *7* (12), A474. https://doi.org/10.1149/1.1814595.

(160) Zhong, G.; Xu, S.; Liu, L.; Zheng, C. Z.; Dou, J.; Wang, F.; Fu, X.; Liao, W.; Wang, H. Effect of Experimental Operations on the Limiting Current Density of Oxygen Reduction Reaction Evaluated by Rotating-Disk Electrode. *ChemElectroChem* **2020**, *7* (5), 1107–1114. https://doi.org/10.1002/celc.201902085.

(161) Poux, T.; Bonnefont, A.; Ryabova, A.; Kéranguéven, G.; Tsirlina, G. A.; Savinova, E. R. Electrocatalysis of Hydrogen Peroxide Reactions on Perovskite Oxides: Experiment *versus* Kinetic Modeling. *Phys. Chem. Chem. Phys.* **2014**, *16* (27), 13595–13600. https://doi.org/10.1039/C4CP00341A.

(162) Jiang, K.; Back, S.; Akey, A. J.; Xia, C.; Hu, Y.; Liang, W.; Schaak, D.; Stavitski, E.; Nørskov, J. K.; Siahrostami, S.; Wang, H. Highly Selective Oxygen Reduction to Hydrogen Peroxide on Transition Metal Single Atom Coordination. *Nat Commun* **2019**, *10* (1), 3997. https://doi.org/10.1038/s41467-019-11992-2.

(163) Lu, Z.; Chen, G.; Siahrostami, S.; Chen, Z.; Liu, K.; Xie, J.; Liao, L.; Wu, T.; Lin, D.; Liu, Y.; Jaramillo, T. F.; Nørskov, J. K.; Cui, Y. High-Efficiency Oxygen Reduction to Hydrogen Peroxide Catalysed by Oxidized Carbon Materials. *Nat Catal* **2018**, *1* (2), 156–162. https://doi.org/10.1038/s41929-017-0017-x.

(164) Chen, S.; Luo, T.; Chen, K.; Lin, Y.; Fu, J.; Liu, K.; Cai, C.; Wang, Q.; Li, H.; Li, X.; Hu, J.; Li, H.; Zhu, M.; Liu, M. Chemical Identification of Catalytically Active Sites on Oxygen-doped Carbon Nanosheet to Decipher the High Activity for Electro-synthesis Hydrogen Peroxide. *Angew. Chem.* **2021**, *133* (30), 16743–16750. https://doi.org/10.1002/ange.202104480.

(165) Bonakdarpour, A.; Delacote, C.; Yang, R.; Wieckowski, A.; Dahn, J. R. Loading of Se/Ru/C Electrocatalyst on a Rotating Ring-Disk Electrode and the Loading Impact on a H2O2 Release during Oxygen Reduction Reaction. *Electrochemistry Communications* **2008**, *10* (4), 611–615. https://doi.org/10.1016/j.elecom.2008.02.004.

(166) Safari, M.; Delacourt, C. Mathematical Modeling of Lithium Iron Phosphate Electrode: Galvanostatic Charge/Discharge and Path Dependence. *J. Electrochem. Soc.* **2011**, *158* (2), A63. https://doi.org/10.1149/1.3515902.

(167) Boudet, A. Investigation of Platinum-Free ORR Catalysts at Agglomerate Scale: From Local Probe Characterizations to Modeling Studies, 2021. https://www.theses.fr/2021UPASF037.

(168) Orfanidi, A.; Rheinländer, P. J.; Schulte, N.; Gasteiger, H. A. Ink Solvent Dependence of the Ionomer Distribution in the Catalyst Layer of a PEMFC. *Journal of The Electrochemical Society* **2018**, *165* (14), F1254–F1263. https://doi.org/10.1149/2.1251814jes.

(169) Bernt, M.; Siebel, A.; Gasteiger, H. A. Analysis of Voltage Losses in PEM Water Electrolyzers with Low Platinum Group Metal Loadings. *Journal of The Electrochemical Society* **2018**, *165* (5), F305–F314. https://doi.org/10.1149/2.0641805jes.

(170) Harzer, G. S.; Schwämmlein, J. N.; Damjanović, A. M.; Ghosh, S.; Gasteiger, H. A. Cathode Loading Impact on Voltage Cycling Induced PEMFC Degradation: A Voltage Loss Analysis. *Journal of The Electrochemical Society* **2018**, *165* (6), F3118–F3131. https://doi.org/10.1149/2.0161806jes.

(171) Singh, V.; Tiwari, A.; Nagaiah, T. C. Facet-Controlled Morphology of Cobalt Disulfide towards Enhanced Oxygen Reduction Reaction. *Journal of Materials Chemistry A* **2018**, *6* (45), 22545–22554. https://doi.org/10.1039/C8TA06710D.

(172) Tiwari, A.; Singh, V.; Mandal, D.; Nagaiah, T. C. Nitrogen Containing Carbon Spheres as an Efficient Electrocatalyst for Oxygen Reduction: Microelectrochemical Investigation and Visualization. *Journal of Materials Chemistry A* **2017**, *5* (37), 20014–20023. https://doi.org/10.1039/C7TA05503J.

(173) Tiwari, A.; Singh, V.; Nagaiah, T. C. Tuning the $MnWO_4$ Morphology and Its Electrocatalytic Activity towards Oxygen Reduction Reaction. *Journal of Materials Chemistry A* **2018**, *6* (6), 2681–2692. https://doi.org/10.1039/C7TA10380H.

(174) Sidhureddy, B.; Prins, S.; Wen, J.; Thiruppathi, A. R.; Govindhan, M.; Chen, A. Synthesis and Electrochemical Study of Mesoporous Nickel-Cobalt Oxides for Efficient Oxygen Reduction. *ACS Applied Materials & Interfaces* **2019**, *11* (20), 18295–18304. https://doi.org/10.1021/acsami.8b22351.

(175) Seiffarth, G.; Steimecke, M.; Walther, T.; Kühhirt, M.; Rümmler, S.; Bron, M. Mixed Transition Metal Oxide Supported on Nitrogen Doped Carbon Nanotubes - a Simple Bifunctional Electrocatalyst Studied with Scanning Electrochemical Microscopy. *Electroanalysis* **2016**, *28* (10), 2335–2345. https://doi.org/10.1002/elan.201600254.

(176) Chen, X.; Botz, A. J. R.; Masa, J.; Schuhmann, W. Characterisation of Bifunctional Electrocatalysts for Oxygen Reduction and Evolution by Means of SECM. *Journal of Solid State Electrochemistry* **2016**, *20* (4), 1019–1027. https://doi.org/10.1007/s10008-015-3028-z.

(177) Limani, N.; Boudet, A.; Blanchard, N.; Jousselme, B.; Cornut, R. Local Probe Investigation of Electrocatalytic Activity. *Chemical Science* **2021**. https://doi.org/10.1039/D0SC04319B.

(178) Boudet, A.; Henrotte, O.; Limani, N.; El Orf, F.; Oswald, F.; Jousselme, B.; Cornut, R. Unraveling the Link between Catalytic Activity and Agglomeration State with Scanning Electrochemical

Microscopy and Atomic Force Microscopy. *Anal. Chem.* **2022**, *94* (3), 1697–1704. https://doi.org/10.1021/acs.analchem.1c04256.

(179) Henrotte, O.; Boudet, A.; Limani, N.; Bergonzo, P.; Zribi, B.; Scorsone, E.; Jousselme, B.; Cornut, R. Steady-State Electrocatalytic Activity Evaluation with the Redox Competition Mode of Scanning Electrochemical Microscopy: A Gold Probe and a Boron-Doped Diamond Substrate. *ChemElectroChem* **2020**, *7* (22), 4633–4640. https://doi.org/10.1002/celc.202001088.

(180) Girard, H. A.; Scorsone, E.; Saada, S.; Gesset, C.; Arnault, J. C.; Perruchas, S.; Rousseau, L.; David, S.; Pichot, V.; Spitzer, D.; Bergonzo, P. Electrostatic Grafting of Diamond Nanoparticles towards 3D Diamond Nanostructures. *Diamond and Related Materials* **2012**, *23*, 83–87. https://doi.org/10.1016/j.diamond.2012.01.021.

(181) Klapetek, P.; Ohlídal, I. Theoretical Analysis of the Atomic Force Microscopy Characterization of Columnar Thin Films. *Ultramicroscopy* **2003**, *94* (1), 19–29. https://doi.org/10.1016/S0304-3991(02)00159-6.

(182) Chemical Rubber Company. *CRC Handbook of Chemistry and Physics: A Ready-Reference Book of Chemical and Physical Data*, 85. ed.; Lide, D. R., Ed.; CRC Press: Boca Raton, 2004.

(183) Eckhard, K.; Schuhmann, W. Localised Visualisation of O2 Consumption and H2O2 Formation by Means of SECM for the Characterisation of Fuel Cell Catalyst Activity. *Electrochimica Acta* **2007**, *53* (3), 1164–1169. https://doi.org/10.1016/j.electacta.2007.02.028.

(184) Sánchez-Sánchez, C. M.; Bard, A. J. Hydrogen Peroxide Production in the Oxygen Reduction Reaction at Different Electrocatalysts as Quantified by Scanning Electrochemical Microscopy. *Analytical Chemistry* **2009**, *81* (19), 8094–8100. https://doi.org/10.1021/ac901291v.

(185) Combellas, C.; Fermigier, M.; Fuchs, A.; Kanoufi, F. Scanning Electrochemical Microscopy. Hydrodynamics Generated by the Motion of a Scanning Tip and Its Consequences on the Tip Current. *Anal. Chem.* **2005**, *77* (24), 7966–7975. https://doi.org/10.1021/ac0513358.

(186) Menga, D.; Low, J. L.; Li, Y.-S.; Arčon, I.; Koyutürk, B.; Wagner, F.; Ruiz-Zepeda, F.; Gaberščček, M.; Paulus, B.; Fellinger, T.-P. Resolving the Dilemma of Fe–N–C Catalysts by the Selective Synthesis of Tetrapyrrolic Active Sites via an Imprinting Strategy. *J. Am. Chem. Soc.* **2021**, *143* (43), 18010–18019. https://doi.org/10.1021/jacs.1c04884.

(187) Tsuneda, T.; Singh, R. K.; Iiyama, A.; Miyatake, K. Theoretical Investigation of the H_2O_2-Induced Degradation Mechanism of Hydrated Nafion Membrane via Ether-Linkage Dissociation. *ACS Omega* **2017**, *2* (7), 4053–4064. https://doi.org/10.1021/acsomega.7b00594.

(188) Zatoń, M.; Rozière, J.; Jones, D. J. Current Understanding of Chemical Degradation Mechanisms of Perfluorosulfonic Acid Membranes and Their Mitigation Strategies: A Review. *Sustainable Energy Fuels* **2017**, *1* (3), 409–438. https://doi.org/10.1039/C7SE00038C.

(189) Charreteur, F.; Ruggeri, S.; Jaouen, F.; Dodelet, J. P. Increasing the Activity of Fe/N/C Catalysts in PEM Fuel Cell Cathodes Using Carbon Blacks with a High-Disordered Carbon Content. *Electrochimica Acta* **2008**, *53* (23), 6881–6889. https://doi.org/10.1016/j.electacta.2007.12.051.

(190) Ramli, N. I. T.; Abdul Rashid, S.; Sulaiman, Y.; Mamat, M. S.; Mohd Zobir, S. A.; Krishnan, S. Physicochemical and Electrochemical Properties of Carbon Nanotube/Graphite Nanofiber Hybrid Nanocomposites for Supercapacitor. *Journal of Power Sources* **2016**, *328*, 195–202. https://doi.org/10.1016/j.jpowsour.2016.07.110.

(191) Bentley, C. L. Scanning Electrochemical Cell Microscopy for the Study of (Nano)Particle Electrochemistry: From the Sub-particle to Ensemble Level. *Electrochemical Science Adv* **2022**, *2* (3). https://doi.org/10.1002/elsa.202100081.

(192) Fujishima, A.; Einaga, Y.; Rao, T. N.; Tryk, D. A. *Diamond Electrochemistry*; Elsevier Science: Burlington, 2005.

(193) Chlistunoff, J.; Sansiñena, J.-M. On the Use of Nafion® in Electrochemical Studies of Carbon Supported Oxygen Reduction Catalysts in Aqueous Media. *Journal of Electroanalytical Chemistry* **2016**, *780*, 134–146. https://doi.org/10.1016/j.jelechem.2016.09.014.

(194) Kruusenberg, I.; Alexeyeva, N.; Tammeveski, K. The PH-Dependence of Oxygen Reduction on Multi-Walled Carbon Nanotube Modified Glassy Carbon Electrodes. *Carbon* **2009**, *47* (3), 651–658. https://doi.org/10.1016/j.carbon.2008.10.032.

(195) Zaera, F. Molecular Approaches to Heterogeneous Catalysis. *Coordination Chemistry Reviews* **2021**, *448*, 214179. https://doi.org/10.1016/j.ccr.2021.214179.